Numerical Prediction of the Maneuvering Characteristics of Submarines Operating Near the Free Surface

by

Michael J. Griffin

Submitted to the Department of Ocean Engineering
in partial fulfillment of the requirements for the degree of

Doctor of Philosophy in Ocean Engineering

at the

MASSACHUSETTS INSTITUTE OF TECHNOLOGY

February 2002

Author .....
Department of Ocean Engineering
October 31, 2001

Certified by .....
Jerome H. Milgram
Professor
Thesis Supervisor

Accepted by .....
Professor Henrik Schmidt
Chairman, Departmental Committee on Graduate Studies
Department of Ocean Engineering

Numerical Prediction of the Maneuvering Characteristics of Submarines Operating Near the Free Surface

by

Michael J. Griffin

Submitted to the Department of Ocean Engineering
on October 31, 2001, in partial fulfillment of the
requirements for the degree of
Doctor of Philosophy in Ocean Engineering

Abstract

A method for coupling a Reynolds-averaged Navier-Stokes (RANS) computer code with an inviscid panel code to predict the maneuvering characteristics of submarines operating near the free-surface has been developed. The RANS code calculates the flow field immediately surrounding and in the wake of the body where viscous effects are important. The panel code calculates the fluid flow in the far field including the free-surface where viscous effects are negligible. The computational domains used by each code overlap, and it is this overlap that enables their coupling. The evolution of the free-surface boundary condition is linked to the evolution of the bulk flow through a novel iteration technique that first computes the viscous flow near and in the wake of the body, and then computes the potential flow outside the viscous region including at the free-surface.

Calculated and measured vertical force and pitching moment are in excellent agreement for conditions where free-surface effects are minimal. In addition calculated vertical plane maneuvering coefficients are presented. There is no known experimental force and moment data available for submarine bodies where free-surface effects are significant, and therefore only qualitative statements pertaining to validation of the method can be made under such conditions.

Five submarine geometries operating at five depths, seven Froude numbers and several pitch angles have been simulated to obtain relationships between these parameters and the vertical force and pitching moment on the bodies. Iterative and grid convergence have been demonstrated.

Thesis Supervisor: Jerome H. Milgram
Title: Professor

Acknowledgments

The author wishes to thank Professor Jerome Milgram for supporting me throughout this research and giving me countless important input. Professors Jake Kerwin, Paul Sclavounos and Cliff Whitcomb for helping me to refine my research. Dr. Chao-Ho Sung for giving me invaluable mentoring over the years. Drs. Francis Noblesse and Dane Hendrix have freely given of their time and expertise on more occasions than I can count. None of this research would have been possible without the generous financial support of the Dr. William Morgan at NSWCCD and Mr. Jim Fein at ONR. Virtually unlimited computational resources were provided by the Arctic Region Supercomputing Center in Fairbanks, AK.

Finally, there is no way that and of this would have been possible without the unending patience and support of my beautiful wife Lili and my two beautful daughters Keely and Marlee.

Contents

List of Figures

List of Tables

Chapter 1

Introduction

1.1 Background

Throughout the Cold War, the U.S. Navy focused its research and development efforts on designing its submarine fleet to operate undetected for long periods of time in the open ocean. When the Cold War ended and regional conflicts began to erupt such as the Gulf War, it became apparent that that Navy's open ocean war-fighting capability did not fully meet the needs of littoral operations.

Submarines designed to operate primarily in deep water were suddenly carrying out missions in shallow water. Because the operating envelopes of submarines in shallow water are so much smaller than the operating envelopes of submarines in deep water, they become more vulnerable to counter measures such as mines, e.g. far fewer mines are necessary to block the passage of a submarine in shallow water than in deep water. A tremendous amount of research has been directed at rectifying this newly important vulnerability to mines.

It follows that if submarines are more frequently operating in shallow water then they are also more frequently operating near the free-surface. This is in fact the case. The focus of the present research seeks to address this issue.

A well known but little understood complication of operating near the free-surface is the effect that the free-surface has on the maneuvering characteristics of the submarine. The maneuvering characteristics of a submarine define its ability to maintain

stable, controlled motions while operating. In general, submarines are designed to be only slightly stable so that they can be more easily maneuvered. Thus, off-design operating conditions can make the submarine unstable.

As stated earlier, submarines have been designed with the assumption that most of their operations would take place in deep water. This assumption greatly simplifies the requirements of the submarine in terms of maintaining stability and control. Specifically, in deep water the fluid is assumed to behave symmetrically as the body moves through it, i.e. the fluid behaves above the body as it does below the body assuming the body is symmetric above and below with exceptions due to various appendages like the sail.

However, the free-surface invalidates this assumption. As the submarine moves closer to the surface it necessarily interacts with it. This interaction is, of course, not symmetric above and below the body. In fact, this interaction appears to have some surprisingly complex effects on the stability and control of the submarine. These effects will be discussed in later chapters.

In deep water moving the stern planes to the dive position pitches the stern planes up causing a submarine to dive. Near the free-surface a submarine must pitch its stern planes up slightly to maintain a constant depth. This is due to the lifting effect that the submarine experiences there. Simply put, the fluid pressure between the submarine and the free-surface is lower than the pressure between it and the ocean floor. Thus, the submarine tends to rise while operating near the free-surface. Add heavy seas and an only slightly stable design into this mix and you need a very good operator to keep the submarine at a constant depth.

Much like surface ships, near-surface submarines generate free-surface disturbances or wakes that are detectable via satellite surveillance. Wake patterns can reveal not only the position of a submarine, but also its size, speed and direction of travel. The effectiveness of a submarine is strongly (perhaps most importantly) dependent on its ability to avoid detection. Therefore, wake detection by satellite or even the fear of wake detection by satellite can incapacitate a vital part of the Navy's war-fighting capability.

Recent years have also seen a tremendous increase in the use of remotely operated vehicles (ROV's) and autonomous underwater vehicles (AUV's) for salvage and exploration. In fact there have been many important discoveries aided by these vehicles including ship wrecks such as the Titanic. A less newsworthy but no less important duty performed by AUV's and ROV's is mapping the ocean floor. Performance of such missions often requires operating at or near the ocean surface. To create accurate maps requires accurate navigation. Accurate navigation near the ocean surface requires robust control systems. As previously stated, robust control near the free-surface is a non-trivial accomplishment.

Very little research has been directed at predicting the maneuvering characteristics of small vehicles such as ROV's or AUV's near the free-surface. The current research attempts to address this situation.

There are three main thrusts of the current research: 1) accurate and efficient prediction of forces, moments and maneuvering coefficients acting on submerged vehicles, 2) accurate and efficient prediction of free-surface elevations, and 3) automatic generation of thousands of high quality numerical grids. Each of these components are necessary to predict the maneuvering characteristics of near-surface submarines. Each of these efforts will be discussed in detail throughout this and later chapters.

1.2 Prediction of Maneuvering Characteristics

Accurately predicting the maneuvering characteristics of underwater vehicles through numerical simulations has, in recent years, become a realistic goal due to many of the significant advances in numerical techniques and computing power. Maneuvering coefficients are derived from forces and moments. Therefore, predicting maneuvering coefficients accurately requires accurate prediction of forces and moments.

Predicting the forces and moments on a submerged body advancing in a fluid is a challenging task, whether from an analytical, experimental or computational standpoint. The advancing body generates a complex, unsteady, viscous boundary layer and wake, including crossflow separation. When the body is near the free-

surface, the problem becomes even more daunting because the body also generates a complex surface wave system. The energy required to create this system and the interaction of the generated surface waves with the body can have a significant impact on the forces and moments on and thus the maneuvering characteristics of the body.

A great deal of research has been done to predict the forces and moments on two- and three-dimensional submarine-like bodies using empirical and inviscid numerical techniques. These efforts are all limited by the neglect of viscosity. Since so many flow field characteristics around submarines are a direct result of viscosity, it is important to consider viscosity when predicting submarine maneuvering coefficients. There is only a small body of research devoted to predicting the forces and moments on submerged bodies and thus their maneuvering characteristics No previous effort has been made to compute maneuvering coefficients while including viscous effects.

The research presented herein addresses the problem of predicting the flow due to a submerged body operating near the free-surface in a calm sea and in deep water. The forces and moments acting on these bodies as well as the maneuvering coefficients predicted here are essential to the effective and efficient design of propulsion and control systems.

In addition the wakes produced by these vehicles and predicted here can be used in their remote identification and tracking. These steady flow predictions are also considered the first step toward the computation of the unsteady flow due to submerged bodies advancing in waves.

1.3 Free-Surface Simulations

To understand the maneuvering characteristics of vehicles the forces and moments acting on those vehicles must either be measured or accurately simulated.

Due to the relatively recently identified need to understand the interaction of submerged vehicles with the free-surface, numerical simulations of free-surface flows have been primarily used to study the interaction and performance of surface ships.

A large body of literature has dealt with the interactions of surface ships and the

free-surface, atesting to the importance of this challenge. The majority of research in this area has focused on panel methods.

Panel methods assume that the fluid is inviscid, incompressible and of constant density, and that the flow is irrotational. These assumptions greatly simplify the governing equations such that panel methods can be used to compute free-surface flows very efficiently. Including the effects of viscosity as in RANS methods, makes the goal of efficiency much more difficult to obtain. However, a large amount of research has dealt in recent years with computing the viscous free-surface around surface ships.

The usefulness of each approach is often debated. However, there is little doubt that each holds an important place in this field.

Two physical conditions must be satisfied at the free-surface: 1) the kinematic boundary condition and 2) the dynamic boundary condition. For the purposes of the present research the kinematic boundary condition states that fluid does not penetrate the free-surface. The dynamic boundary condition states that the pressure is constant everywhere on the free-surface.

Free-surface flows, in general, are unsteady, i.e. the fluid motion is dependent on time. For the purposes of this research the fluid flow is assumed to be steady everywhere except in the turbulent boundary layer and wake of the vehicle and that the fluid upstream of the submerged body is calm.

The flow characteristics very close to and in the wake of a submerged vehicle are influenced by viscous effects. These characteristics include three-dimensional turbulent boundary layers and flow separation. Flow characteristics in the far field, including free-surface wave patterns, are dominated by inviscid effects.

Many methods have been developed to attempt to model the free-surface. In general these methods fall into three categories: 1) panel methods, 2) viscous methods, and 3) hybrid methods. Each of the three approaches are discussed in the remainder of this section.

1.3.1 Panel Methods

There are a number of approaches to solving the inviscid flow equations. By assuming only small free-surface deviations, the boundary condition can be linearized. Limited analytic results are possible using this approach.

Panel methods transform the problem into a boundary integral formulation. In so doing, the dimensionality of the problem for the initial set of unknowns is reduced from three to two. The computational savings of this approach can be dramatic. In addition, there is a considerable time savings in the discretization of the geometries. In three dimensions volume grids become surface grids.

The free-surface boundary condition may be applied at the exact location of the free-surface or at the plane of the undisturbed free-surface. The latter is accomplished by a Taylor series expansion, which is usuallly linearized by dropping the high-order derivatives of the fluid velocity resulting from the expansion and is known as Kelvin linearization. Kelvin linearization is often combined with imposing the Neumann boundary condition on the ship hull ($\vec{n} \cdot \nabla\phi \equiv \phi_n = n_x$), where ϕ is the velocity potential and $\vec{n}$ is the hull normal vector. The resulting method is called the Kelvin-Neumann method.

In the pioneering work of Hess and Smith[12] a method was developed for predicting the flow about non-lifting, three-dimensional bodies of arbitrary shape in an infinite fluid. Some years later Dawson[6] computed the inviscid free-surface flows due to surface ships by enforcing a linearized boundary condition on the plane.

Several authors have attempted to compute flowfields around bodies operating near the free-surface. Havelock [10] was the first to compute the wave resistance of a spheroid using slender body theory.

Thomas [31] developed a high-order combined panel and spectral method for modelling wave interactions with two-dimensional submerged bodies like the circular cylinder. Scullen [23] used a nonlinear panel method to compute the free-surface flows for submerged spheroids.

1.3.2 RANS Methods

Reynolds-averaged Navier-Stokes or RANS methods include the effects of viscosity. In so doing, RANS methods promise to better model the flow field in numerical simulations. This advantage is not without cost, of course. Although they are getting faster every year, due to increases in computer speed and improved numerical methods, RANS methods are generally much more computationally expensive than panel methods.

RANS methods require the generation of complex three-dimensional numerical grids - a well known bottleneck in computational fluid dynamics (CFD) [5]. This will be discussed in greater detail later in this thesis.

Since it doesn't make much sense to include the effects of viscosity without the effects of turbulence, RANS methods require the development of turbulence models. Turbulence models have improved tremendously in recent years but remain a source of uncertainty and instability in the RANS methods.

RANS methods also suffer from excessive numerical damping of the solution in the far field, which prevents accurate calculation of the far-field, particularly the far wake. This problem has been addressed in the literature but is still largely unsolved.

These disadvantages are especially significant in the current research. To compute maneuvering coefficients for even a single geometry requires many dozens of three-dimensional simulations. Inefficient, unstable and highly dissipative RANS simulations would preclude their use in such applications.

Panel methods are far more computationally efficient than RANS methods and do not have a problem with numerical dissipation, but they ignore the effects of viscosity. It is therefore logical to utilize the strengths of each and to avoid their weaknesses by coupling the two methods.

Several authors have used this coupling approach to simulate the free-surface flow past surface ships. Tahara and Stern [30] coupled a RANS method with a source doublet method by using the RANS solution to create a displacement body which the panel code used to calculate the free-surface flow.

1.3.3 Hybrid Methods

Hybrid methods use both panel methods and RANS methods in the prediction of flow fields around marine vehicles. Hybrid methods are designed to take advantage of the strengths of each and avoid their weaknesses. In other words, the panel code is used in that part of the flow domain where the flow is believed to be dominated by inviscid effects and the RANS code is used only where the viscous effects are important. In practice, this means that the RANS code is used near the body and the panel code is used everywhere else.

Campana et al. [1] used a linearized potential-flow method coupled with a near-field viscous method coupled with a free-surface for flows about surface ships. Their method requires a calculation with the RANS and potential methods employing a double-body solution, and then a second calculation with the free-surface effects taken into account. The solution of the second calculation is then used. In the current method the RANS and panel methods no double-body solution is required. Thus, it is believed that the current method is a more efficient approach.

Chen et al. [3] used a combination of RANS and panel methods to iteratively calculate the free-surface flow with both the RANS method and the panel method for flows about surface ships. Their method also requires a double-body solution, and then the free-surface effects are taken into account. However, it differs from the approach of Campana et al. by taking into account the free-surface effects more than once. The procedure is as follows: 1) the double-body solution is computed, 2) the free-surface effects are computed, 3) steps 1 and 2 are repeated until the desired convergence is achieved. The velocities used as the boundary condition for the double-body calculation are, however, no longer double-body velocities. Thues, there is an inherent inaccuracy to this approach that is not present in the current method. The current method will be discussed in more detail in later chapters.

There are obvious advantages to the hybrid approach. Since the vast majority of most flow domains can be characterized accurately as inviscid, the viscous domain need not be very large. Since viscous codes are generally much slower than panel

codes, this benefit leads to huge computational cost savings.

Additionally, since RANS codes suffer from excessive numerical dissipation, confining the viscous domain to very near the body can mitigate this damping and improve the overall accuracy of the prediction.

Unfortunately, there is no such thing as a free lunch. Both RANS and panel codes tend to be complex and difficult to use. Efficiently converged solutions from either method can be difficult to obtain for complex three-dimensional geometries. Using both in tandem can exacerbate these problems. It is, therefore, essential to use both efficient and robust RANS and panel methods when performing hybrid calculations.

Another important issue that arises when using hybrid methods is that RANS methods operate with velocities while panel methods generally use velocity potentials. Translating between the two naturally introduces another possibile source of error.

1.4 Numerical Grid Generation

No discussion of CFD would be complete without considering the generation of numerical grids. Recent advances in solving the Navier-Stokes equations have far outstripped advances in grid generation. For many years grid generation has been cited as one of the most significant bottlenecks in CFD simulations.

Grid generation is not a botteneck because it is technically difficult. In fact, generating a three-dimensional numerical grid around even complex bodies can be simple in principle. It is a bottleneck, however, because it is usually quite tedious and time consuming.

Traditional grid generation methods using graphical user interface driven computer programs can only do so much to speed the process. These programs make it relatively easy to generate grids around even the most complex geometry. Although much of the process can be automated, without exception it is difficult to generate many grids of similar geometries and or similar domains without human interaction.

Engineers wishing to design a vehicle to operate near a free surface must consider a high-dimensional parameter space of operating conditions. Speed, depth, angle of

attack and geometry are often the most important parameters that must be varied in the design process. The cumulative total number of unique operating conditions that must be tested and accounted for can easily approach the tens of thousands. In other words, if numerical procedures are to be used to predict the maneuvering characteristics of near surface submarines, a range in geometry and operating conditions of many thousands of calculations must be performed.

It is absolutely critical then that every aspect of the numerical procedure (the RANS method, the panel method and the numerical grid generation method) be extremely efficient, i.e. there can be no bottlenecks. For the present research a novel method for efficiently generating thousands of numerical grids around submarines for various speeds, depths, angles of attack and geometry was developed.

The technique developed here takes advantage of the inherent similarity of all grids around submarine-like geometries to remove the need for human intervention when changing speed, depth, angle of attack and geometry. Thus, it was possible to generate many thousands of three-dimensional numerical grids for the current research without the human intervention that slows traditional grid generation. This in turn has enabled the establishment of a database of maneuvering coefficients to be used by engineers to design new submarines.

1.5 Current Method

The method used in the current research is a hybrid method in that it uses both a panel code and a RANS code. In this case the panel code is used in the "outer" domain, which includes the free-surface. The RANS code computes the fluid flow only near the body or in the "inner" domain. The flow is assumed to be steady and the free-surface initially undisturbed.

The novelty of the approach lies in the use of a region of overlap by both the inner and the outer domains. This overlapping region is chosen so as to exclude the boundary layer near the body and the free surface itself.

Thus, the panel code is used in a region outside the boundary layer near the body

up to the free-surface and extended in all other directions to infinity. The RANS code is used only in the region near the body including the boundary layer and in the wake where viscous effects are most important.

The flow within the overlap region is considered to be nearly potential, but because viscous effects are included in this region it need not and can not be entirely potential with the current method.

In brief, the current method uses the RANS code to calculate the viscous flow near the body and to determine the bounday condition for the panel code just outside the viscous boundary layer. The panel code uses this to calculate the outer boundary condition for the RANS code given the current speed and depth. The two domains do not just meet on a surface but overlap each other. This process is repeated in an iterative manner until some measure of convergence is satisfied.

Solutions are obtained after 10 or less iterations of the RANS and panel codes. Numerical grids are generated automatically. Parameters such as speed, depth and angle of attack are varied automatically. Over one thousand three-dimensional solutions were calculated to generate a small database of maneuvering coefficients. This database can be used as is or built upon to provide immediate insight into the maneuvering characteristics of submarines operating near a free-surface.

Several smaller computer codes were developed to assist in the coupling of the grid, panel and RANS codes. A sophisticated UNIX shell script was developed to manage the execution of the computer codes as well as to automatically carry out the parameter studies.

The current combination of efficient computer codes and sophisticated shell scripts combine to make possible for the first time the prediction of maneuvering characteristics for a broad range of near surface submarines.

1.6 Validation and Verification

Published predictions of forces and moments using *any* method for near-surface submerged bodies are a rarity. Predictions of maneuvering characteristics are even more

rare.

This is due at least in part to the scarcity of high quality experimental measurements. It is also, no doubt, due to the difficulty in obtaining accurate, converged comparisons with the experimental data that is available.

There is no unclassified experimental data available with which to compare numerical predictions of submarines operating near the free-surface. All of the near-surface comparisons included in the present research are either indirect or with theory.

Because of the lack of validated predictions for near-surface cases by the current or any other method and because there is scant experimental data with which to directly compare the current computations, it was uncertain at the beginning of this research if including the free-surface in such calculations was even practical. Therefore, to begin it was necessary to perform a large number of calculations to predict the forces and moments on bodies in an infinite fluid. These predictions are included in Chapter 7.

A number of things can be done to validate and verify numerical predictions in the absence of experimental data. Many of these things should be done in the *presence* of experimental data. They include grid convergence and iterative convergence studies and comparisons with theory.

1.7 Content of Thesis

The remainder of this thesis examines, in detail, each of the three principal components of the new coupling method, the preliminary validation that was performed, and the results of the analyses

Chapters 2, 3 and 4 detail the RANS, panel, and grid methods used, respectively. Chapter 5 discusses the new coupling method. Chapter 6 considers the geometries and numerical grids used. Chapter 7 presents the preliminary work that was performed to verify and validate the RANS code. Chapter 8 presents the results of the validation and verification of the new method. Chapter 9 details the maneuvering characteristics of the geometries considered. Chapter 10 presents the free-surface wakes generated by

the geometries under a number of flow conditions. Finally, conclusions are presented in Chapter 11.

Chapter 2

RANS Method

2.1 Introduction to the RANS Method

Three major computer programs were coupled in the current research to 1) generate numerical grids, 2) compute viscous flow near the body and 3) to compute the potential flow away from the body. The viscous flow is computed by the Reynolds-averaged Navier-Stokes, RANS, code IFLOW representing the work of Sung et al.[24], [25], [26], [27], [28], Tsai et al.[32], Huang et al.[13] and Griffin et al.[9].

IFLOW solves the two- and three-dimensional incompressible steady and unsteady RANS equations using a non-linear $k-\omega$ turbulence model developed by Wilcox[34] for closure.

The IFLOW code was chosen for the present research in large measure because of the extensive prior effort made to validate it against a wide variety of experimental measurements including forces and moments on deeply submerged bodies. IFLOW has also been shown to accurately characterize boundary layer flows, and flows with crossflow separation which typically occur around maneuvering vehicles. This prior work was critical to the success of the current research as calculating forces and moments on submerged bodies is a relatively new challenge for RANS codes and only one other RANS code is known to have been used for this reason.

IFLOW has also been shown to be one of the most computationally efficient RANS codes. To calculate maneuvering coefficients over a wide range of operating conditions

required many thousands of complete three-dimensional calculations had to be made. Inefficient use of available computational resources would have made it impossible to present the extensive set of results shown in later chapters.

IFLOW has also been proven to be an extremely robust computer code despite the fact that it is a "research code". In general, if IFLOW converges at one set of conditions for a particular geometry it will converge at all conditions for that geometry. This is another critical characteristic that enabled the completion of the parameter studies included here.

Finally, IFLOW has been shown to yield grid independent solutions for complex geometries at what are considered to be rather modest grid resolutions. Showing grid independence in RANS calculations is, in general, a time consuming effort.

In the following sections the numerical schemes implemented in IFLOW are presented and the turbulence model is described.

2.2 Governing Equations

The governing equations are written as

$$\frac{\partial u_i}{\partial x_i} = 0 \tag{2.1}$$

$$\frac{\partial u_i}{\partial t} + \frac{\partial u_i u_j}{\partial x_j} = -\frac{\partial p^*}{\partial x_i} + \frac{\partial}{\partial x_j}(\nu \frac{\partial u_i}{\partial x_j} - \tau_{ij}) \tag{2.2}$$

$$\frac{\partial K}{\partial t} + \frac{\partial}{\partial x_j}(u_i K) - \frac{\partial}{\partial x_j}[(\nu + \sigma_k \nu_t)\frac{\partial K}{\partial x_j}] = -\tau_{ij}\frac{\partial u_i}{\partial x_j} - \beta^* \omega K \tag{2.3}$$

$$\frac{\partial \omega}{\partial t} + \frac{\partial}{\partial x_j}(u_i \omega) - \frac{\partial}{\partial x_j}[(\nu + \sigma_\omega \nu_t)\frac{\partial \omega}{\partial x_j}] = -\alpha \frac{\omega}{K}\tau_{ij}\frac{\partial u_i}{\partial x_j} - \beta\omega^2, \tag{2.4}$$

where $\beta^* = 0.09$, $\beta = \frac{3}{40}$, $\alpha = \frac{5}{9}$, $\sigma_\kappa = \sigma_\omega = \frac{1}{2}$, u_i is the Cartesian velocity component, p^* is the pressure divided by a constant density ρ, k is the turbulent kinetic energy, ω is the specific dissipation rate, ν is the kinematic viscosity, ν_t is the eddy viscosity

given as k/ω and τ_{ij} is the Reynolds stress tensor.

The variables are non-dimensionalized as follows: u_i by the free stream velocity U_0, x_i by the characteristic length L and p by $\rho {U_0}^2/2$. L here is the length of the submarine. The origin of the coordinate system is fixed at the bow of the submarine. The x-axis is along the longitudinal axis of the vehicle with positive pointing aft. The y-axis is in the lateral direction with positive pointing starboard. The z-axis is positive in the upward direction toward the free-surface to form a right hand coordinate system.

The above equations are solved by the artificial compressibility approach first proposed by Chorin [4] and improved by Turkel [33]. In this approach an artificial time derivative of pressure is added to the continuity equation to permit the solution to be advanced in time. Without this derivative the system of equations is singular. This approach has been successfully used by Chang and Kwak [2]. A finite volume method is used.

The mean flow is discretized by a second-order accurate central difference method with fourth-order dissipation terms. The turbulent mean flow is discretized by one of the upwind schemes suggested by Yee [36]. An upwind scheme is used for the turbulent flow because the matrix is already diagonal. Therefore, there is no additional cost in doing the characteristic formulation.

The time step is based on an explicit one-step multi-stage Runge-Kutta method to reach a steady-state solution. Several convergence acceleration techniques including multigrid, local time step, preconditioning and bulk viscosity damping are implemented by the IFLOW code.

A multi-block grid structure is used for complex geometries. For example, the SUBOFF body with sail is conveniently discretized with a grid block that wraps around the body and a second block that extends from the sail cap to the outer boundary. This grid structure or topology is not only convenient, but it also makes generating grids with non-crossing grid lines much easier. A similar grid structure is used for the two geometries with stern appendages.

Because we are interested only in the steady state solution, local time stepping is

used to accelerate convergence. Each point in the grid is advanced by the maximum possible time step rather than the global maximum or constant time step. This is advantageous when time steps vary dramatically from one area of the grid to another.

Numerical preconditioning is used to make the speeds of the various wave modes more or less the same so that convergence can be accelerated. This is important when using the artificial compressibility approach to solve for the incompressible flow because the sound speed (one of the wave modes) propagates much faster than the fluid speed.

The preconditioned mean flow with viscous terms neglected is written in conservative form, i.e. the coefficients of the derivative terms are constant, as

$$P_o^{-1} q_t + F_x + G_y + H_z = 0 \tag{2.5}$$

where the preconditioned matrix P_o and the three components of fluxes F, G, and H are defined as

$$P_o^{-1} = \begin{bmatrix} (1+\gamma)\beta^{-2} & \lambda\beta^{-2}u & \lambda\beta^{-2}v & \lambda\beta^{-2}w \\ \gamma\beta^{-2}u & 1+\gamma\beta^{-2}u^2 & \gamma\beta^{-2}vu & \gamma\beta^{-2}wu \\ \gamma\beta^{-2}v & \gamma\beta^{-2}uv & 1+\gamma\beta^{-2}v^2 & \gamma\beta^{-2}wv \\ \gamma\beta^{-2}w & \gamma\beta^{-2}uw & \gamma\beta^{-2}vw & 1+\gamma\beta^{-2}w^2 \end{bmatrix}, \tag{2.6}$$

where $\lambda = 1 + \alpha + \gamma$, and

$$q = \begin{bmatrix} p^* \\ u \\ v \\ w \end{bmatrix}, \; F = \begin{bmatrix} u \\ u^2 + p^* - \tau_{xx} \\ uv - \tau_{xy} \\ uw - \tau_{xz} \end{bmatrix}, \tag{2.7}$$

$$G = \begin{bmatrix} v \\ uv - \tau_{yx} \\ v^2 + p^* - \tau_{yy} \\ vw - \tau_{yz} \end{bmatrix}, \; H = \begin{bmatrix} w \\ uw - \tau_{zx} \\ vw - \tau_{zy} \\ w^2 + p^* - \tau_{zz} \end{bmatrix},$$

where α, β^{-2} and γ are preconditioning parameters.

For mathematical analysis, it is easier to write Eq. 2.5 in nonconservative form, i.e. the coefficients of the derivative terms are non-constant,

$$P^{-1}q_t + Aq_x + Bq_y + Cq_z = 0. \tag{2.8}$$

The preconditioning matrix P^{-1} is now changed to

$$P^{-1} = \begin{bmatrix} (1+\gamma)\beta^{-2} & \gamma\beta^{-2}u & \gamma\beta^{-2}v & \gamma\beta^{-2}w \\ \alpha\beta^{-2}u & 1 & 0 & 0 \\ \alpha\beta^{-2}v & 0 & 1 & 0 \\ \alpha\beta^{-2}w & 0 & 0 & 1 \end{bmatrix}. \tag{2.9}$$

For the present research $\alpha = 1$, $\gamma = 0$ and $\beta^{-2} = max(|u|^2, \epsilon)$, where $\epsilon = 0.7$.

The final system of equations to be solved in conservative form is

$$\begin{aligned} P_o^{-1}q_t + F_x + G_y + H_z = (P_o^{-1}|PA|q_{xxx})_x \\ +(P_o^{-1}|PB|q_{yyy})_y + (P_o^{-1}|PC|q_{zzz})_z. \end{aligned} \tag{2.10}$$

2.3 Multigrid Technique

The multigrid method developed by Jameson[14] to accelerate the convergence of a system of hyperbolic equations has been implemented in IFLOW. By the cyclic use of a sequence of fine to coarse grids, the multigrid technique is very effective in damping the solution modes with long wave lengths, which are primarily responsible for slow convergence.

In the present research a 3-level V-cycle multigrid technique was used. Boundary conditions are updated at each Runge-Kutta stage of every grid level in the fine-to-coarse path. They are not updated in the coarse-to-fine path. This practice is mainly to avoid introducing boundary condition interpolation errors.

For ease of coding the grid cell number in each coordinate direction for a coarse mesh is half that used for the next finer grid. The computational grid is generated in the following manner. A very fine grid with a sufficiently large number of grid cells to achieve the desired resolution in rapidly changing flow regions including near the walls is first generated. The next coarser grid is generated by removing every other point in the fine grid in each direction. This procedure is repeated to form the

coarsest of the grids.

The 3 level V-cycle solution procedure is as follows:

1. Solve for the flow in the finest grid.
2. Interpolate that solution onto the next coarser grid.
3. Solve for the flow in that grid.
4. Interpolate that solution onto the coarsest grid.
5. Solve for the flow in the coarsest grid.
6. Interpolate that solution onto the next finer grid.
7. Solve for the flow in that grid.
8. Interpolate that solution onto the finest grid.
9. Solve for the flow in the finest grid.
10. Repeat Steps 1-9 until prescribed convergence criteria are met.

2.4 Boundary Conditions

Boundary conditions used at the solid wall are that the three components of the velocity and the normal pressure gradient are set to zero.

Two far-field boundary conditions are used here. The downstream or outflow boundary uses a zero gradient for the three velocity components and a non-reflecting condition for the pressure using the technique developed by Hedstrom[11] and Rudy and Strikwerda[22].

The non-reflecting boundary condition is particularly important for computations in small domains such as those used here. It has been carefully implemented such that convergence rates do not deteriorate noticeably for even the smallest domains used. This condition is obtained by setting the time derivative of the characteristic variable corresponding to the negative eigenvalue equal to zero as detailed by Sung[29].

The upstream and far-field boundary conditions use the velocities calculated by the panel code, FKX (see Chapter 3), and the same non-reflecting condition for the pressure.

2.5 Turbulence Model

Time averaging or Reynolds averaging the Navier-Stokes equations results in the appearance of the correlation $\overline{-\rho u_i' u_j'}$ on the right hand side of the equations (the Reynolds-averaged Navier-Stokes or RANS equations). This term is referred to as the Reynolds-stress tensor and is usually denoted by τ_{ij}. To compute all mean flow properties of the turbulent flow a means of computing τ_{ij} is needed. Since $\tau_{ij} = \tau_{ji}$ is a symmetric tensor, it has six independent components and therefore six unknown quantities are produced as a result of Reynolds averaging. Thus a means of closing the RANS equations is necessary, which in the present context means that τ_{ij} must be modeled. This is what is meant by turbulence modeling.

There are many different types of turbulence models. The most popular being zero-equation and two-equation models. Each uses the Boussinesq eddy viscosity approximation to compute τ_{ij} as the product of an eddy viscosity and the mean strain-rate tensor. The eddy viscosity is often computed in terms of a mixing length that is analogous to the mean free path in a gas. Prandtl's well known mixing length hypothesis leads to a model for τ_{ij} or τ_{xy} in two-dimensions:

$$\tau_{xy} = \nu_T dU/dy, \tag{2.11}$$

where U is the velocity of the fluid, y is the direction normal to the wall and ν_T is the eddy viscosity given by

$$\nu_T = l_{mix}^2 \mid dU/dy \mid. \tag{2.12}$$

Calculating ν_T is the fundamental problem of algebraic turbulence models. The eddy viscosity and thus the mixing length depend upon the flow under consideration and therefore must be specified in advance. This means that algebraic models of turbulence are *incomplete* models.

Two-equation turbulence models compute the turbulent kinetic energy as well as the turbulence length scale and are therefore *complete* models of turbulence, i.e. they can be used to predict properties of a given flow with no prior knowledge of the flow.

The K-ω turbulence model is a two-equation model that solves the kinetic energy of turbulence equation, K, and the dissipation per unit turbulence kinetic energy, ω. Several other definitions of ω are given in Wilcox[34]. He attributes to Saffman the following: ω is "... a frequency characteristic of the turbulence decay process under its self interaction ...," and "... ω^2 is the mean square of the vorticity of the 'energy containing eddies' and K is the kinetic energy of the motion induced by the vorticity." In the same reference ω is identified as the RMS fluctuating vorticity or enstrophy and as the ratio of ϵ to K, i.e. the rate of dissipation of turbulence kinetic energy.

The standard two-equation K-ω turbulence model as in Wilcox[34] is used for this analysis.

$$\begin{aligned}
\frac{\partial K}{\partial t} + \overline{\mathrm{u}}_i \frac{\partial K}{\partial \mathrm{x_i}} &= \tau_{\mathrm{ij}} \frac{\partial \overline{\mathrm{u}}_{\mathrm{i}}}{\partial \mathrm{x_j}} - \beta^* \mathrm{K}\omega + \frac{\partial}{\partial \mathrm{x_i}}[(\nu + \sigma^* \nu_{\mathrm{T}}) \frac{\partial \mathrm{K}}{\partial \mathrm{x_i}}] \\
\frac{\partial \omega}{\partial t} + \overline{\mathrm{u}}_i \frac{\partial \omega}{\partial \mathrm{x_i}} &= \alpha \frac{\omega}{\mathrm{K}} \tau_{\mathrm{ij}} \frac{\partial \overline{\mathrm{u}}_{\mathrm{i}}}{\partial \mathrm{x_j}} - \beta \omega^2 + \frac{\partial}{\partial \mathrm{x_i}}[(\nu + \sigma \nu_{\mathrm{T}}) \frac{\partial \omega}{\partial \mathrm{x_i}}]
\end{aligned} \tag{2.13}$$

where t is time, x_i is the position vector, u_i is the velocity vector, ν is the kinematic viscosity and τ_{ij} is the sum of the molecular and Reynolds stress tensors. Also $\nu_T = \gamma^* \frac{K}{\omega}, \gamma^* = 1, \sigma = \sigma^* = 0.5, \beta^* = \frac{9}{100}, \beta = \frac{3}{40}$.

Near the wall: $y \approx 0$; $\tau_{12} = -\overline{u_1' u_2'} = \nu_T \frac{\partial u}{\partial y}$; $u = \frac{u_\tau}{\kappa} \ln[\frac{u_\tau y}{\nu}]$; $K = \frac{u_\tau^2}{\sqrt{\beta^*}}$; $\omega = \frac{u_\tau}{(\sqrt{\beta^*} \kappa y)}$; $\frac{\tau}{K} = \sqrt{\beta^*} = \frac{3}{10}$ (data); $\alpha = \frac{\beta}{\beta^*} - \frac{\sigma \kappa^2}{\sqrt{\beta^*}} \approx \frac{5}{9}$.

The terms in the above equations are defined as follows:

$$\frac{\partial K}{\partial t} + \overline{\mathrm{u}}_i \frac{\partial K}{\partial \mathrm{x_i}} \tag{2.14}$$

is the rate of change of K following a fluid particle

$$\tau_{ij} \frac{\partial \overline{\mathrm{u}}_i}{\partial \mathrm{x_j}} \tag{2.15}$$

is the turbulent kinetic energy production term or the rate at which kinetic energy is transferred from the mean flow to turbulence.

$$\beta^* K\omega \tag{2.16}$$

is the K dissipation term or the rate at which turbulent kinetic energy is converted into thermal internal energy.

$$\frac{\partial}{\partial \mathbf{x}_i}[(\nu + \sigma^* \nu_T)\frac{\partial K}{\partial \mathbf{x}_i} \tag{2.17}$$

is the molecular diffusion term or the rate at which turbulent kinetic energy is diffused by the fluid's natural molecular transport process. The above definitions may be applied to the terms in the ω equation by replacing turbulent kinetic energy and K by dissipation of turbulent kinetic energy and ω.

Wilcox[35] conducted a review of the six closure coefficients ($\gamma = \alpha$, γ^*, σ, σ^*, β and β^*) and suggested the values listed above. Also presented were arguments "as physically meaningful as possible" from which these coefficients could be established. These arguments are extensive and therefore won't be included here. In short they consist of a combination of scaling of the equations describing the flow (RANS, et al.) and experimental observations.

2.6 Modifications to IFLOW

The method by which IFLOW is coupled to the other computer programs involved in the current research is described in greater detail in Chapter 5. In brief, great care was taken to modify IFLOW as little as possible to complete this coupling.

This approach was taken to enhance the maintainability of the coupled method. IFLOW is constantly being updated with enhanced turbulence models, numerical schemes and many other features. By making only small modifications to this code and the other computer codes, it should be possible to rapidly update each component. The coupled method thereby maintains a high level of modularity.

Obviously, some maintenance has to be performed, but in this case it is almost entirely confined to much smaller and more manageable computer programs, which translate the output from one code into the input of another code.

Chapter 3

Panel Method

3.1 Introduction

The second major component of the method developed here is a computer program that computes the velocity field in the potential flow region or overlap region, which is outside the boundary layer region of the body. The Fourier-Kochin (FKX) code developed by Noblesse et al. [15]-[19] was selected for this task for a variety of reasons.

As with IFLOW, FKX has a long development history with a strong emphasis on generality, accuracy, efficiency and robustness. All of these qualities are essential to enabling the massive number of computations described in later chapters.

A unique characteristic of FKX makes it even more attractive for coupling with a viscous flow code. FKX computes the velocity field in the potential flow region given a *velocity* distribution at a boundary surface rather than a potential distribution at the boundary surface. This feature greatly simplified the coupling of FKX to IFLOW, which also only deals with velocity distributions and not velocity potentials, which do not exist in the viscous domain. No conversion from velocities to potentials or from potentials to velocities was necessary. Therefore, two possible sources of error were eliminated.

3.2 Governing Equations

FKX is a 3-D potential-flow computer code based on a free-surface boundary condition linearized about the uniform stream opposing the forward speed of the vehicle. The free-surface Green function satisfying this linearized free surface condition is used.

Variables are nondimensionalized as follows: $t^* = t/\sqrt{L/g}$, $\vec{x}^* = \vec{x}/L$, $\vec{v}^* = \vec{v}/\sqrt{gL}$, pressure $p^* = p/\rho gL$, and the potential $\phi^* = \phi/L\sqrt{gL}$, where $\vec{v}$ is the velocity vector (u, v, w), $\vec{x}$ is the position vector (x, y, z), g is the acceleration due to gravity, and ρ is the fluid density. The * indicating that those variables are nondimensionalized will be dropped hereafter.

The velocity vector, $\vec{v}$, is the disturbance velocity. RANS velocities include the free stream velocity. Therefore, to convert from the panel domain to the RANS domain the free-stream velocity must be added. To convert from the RANS domain to the panel domain the free-stream velocity must be subtracted, i.e. $\vec{v}_{panel} = \vec{v}_{RANS} - U_\infty$.

The forward speed of the ship and the frequency of the ambient regular waves are denoted $\mathcal{U}$ and ω_w, respectively. The flow due to the ship depends on two non-dimensional parameters $Fr_L = \mathcal{U}/\sqrt{gL}$ is the Froude number and $f_L = \omega_w\sqrt{L/g}$ is the nondimensional frequency.

The velocity potentials of the steady and the time-harmonic flow components are defined in terms of a growth parameter ϵ as $\mathcal{R}[\phi(\vec{x})e^{\epsilon t - ift}]$. We have $\epsilon > 0$ so that the flow vanishes as $t \to -\infty$. Steady and time-harmonic flows are obtained in the limit $\epsilon \to +0$.

Laplace's equation $\nabla^2\phi = 0$ is solved subject to the far-field boundary condition $\phi = O(1/\sqrt{x^2+y^2+z^2})$ as $\sqrt{x^2+y^2+z^2} \to \infty$ and the linear free-surface boundary condition

$$[\partial_z - (f + i\epsilon - iFr_L\partial_x)^2]\phi = 0. \tag{3.1}$$

3.3 Green Function

The Green Function can be expressed as a sum of two components:

$$G = G^S + G^F \tag{3.2}$$

where G^S is the Rankine component and G^F is the free-surface component.

The Rankine component of the Green function is written as

$$4\pi G^S = -\frac{1}{r} + \frac{1}{r'} \tag{3.3}$$

where

$$r = \sqrt{(x-\xi)^2 + (y-\eta)^2 + (z-\zeta)^2} \tag{3.4}$$

$$r' = \sqrt{(x-\xi)^2 + (y-\eta)^2 + (z+\zeta)^2}. \tag{3.5}$$

The free-surface component of the Green function is given as

$$4\pi^2 G^F = \lim_{\epsilon \to 0^+} \int_{-\infty}^{+\infty} \int_{-\infty}^{+\infty} \frac{e^{Zk - i(X\alpha + Y\beta)}}{Fr_L^2 \alpha^2 - k - i\epsilon sign(\alpha)} d\alpha d\beta, \tag{3.6}$$

where $k = \sqrt{\alpha^2 + \beta^2}$, $(X, Y, Z \leq 0) = (x - \xi, y - \eta, z + \zeta)$, and $(x, y, z \leq 0)$ is the location of the singularity and $(\xi, \eta, \zeta \leq 0)$ is the flow observation point. Finally,

$$\epsilon = e^{k(z-z_o) + i[\alpha(x-x_o) + \beta(y-y_o)]}. \tag{3.7}$$

The dispersion function, D, is given as

$$D = (Fr_L \alpha)^2 - k. \tag{3.8}$$

In the Fourier-Kochin formulation calculations involve distributions of singularities of the form

$$\mathcal{P} = \int_{P_o} G\sigma \tag{3.9}$$

and

$$\mathcal{P} = \int_{P_o} \nabla G \cdot \vec{\delta} \tag{3.10}$$

P_o is the hull panel or waterline segment near the point $\vec{x_o} = (x_o, y_o, z_o)$, which is in the middle of the hull panel or waterline segment, and σ, $\vec{\delta} = (\delta_x, \delta_y, \delta_z)$ are the source and dipole densities, respectively.

The usual panel method approach is to evaluate G and ∇G then integrate. In the Fourier-Kochin approach the space integration is performed first with respect to $\vec{x}$ and then a Fourier integration with respect to α and β is done. Thus the Green function is not evaluated directly. It is instead based on the Fourier representation of the free-surface component, $\mathcal{P}^F$.

$$4\pi^2\mathcal{P}^F = \lim_{\epsilon\to 0^+} \int_{-\infty}^{+\infty}\int_{-\infty}^{+\infty} \frac{Se^{Zk-i(X\alpha+Y\beta)}}{Fr_L^2\alpha^2 - k - i\epsilon sign(\alpha)} d\alpha d\beta \tag{3.11}$$

where $(X, Y, Z \leq 0) = (\xi - x_o, \eta - y_o, \zeta + z_o)$ and S is the spectrum function defined as

$$S = \int_{P_o} \epsilon\sigma \tag{3.12}$$

$$S = \int_{P_o} \epsilon(i\alpha\delta_x + i\beta\delta_y + k\delta_z) \tag{3.13}$$

For the current research sources and dipole densities are evaluated on the boundary surface S^i using the Green identity. These densities are expressed as functions of the velocity components on S^i. The function S becomes

$$S(\alpha, \beta) = \int_{S^i} A^{S^i} e^{k(z-z_0)+i(\alpha(x-x_0)+\beta(y-y_0))} dA \tag{3.14}$$

where dA is the differential area element of the surface S^i and

$$A^{S^i} = \vec{u} \cdot \vec{n} + i(\frac{\beta}{k} t_x - \frac{\alpha}{k} t_y)\vec{u} \cdot \vec{s} - i(\frac{\beta}{k} s_x - \frac{\alpha}{k} s_y)\vec{u} \cdot \vec{t}. \tag{3.15}$$

Notice that each variable in Eq. 3.15 is either a geometric variable or a velocity variable. The velocity potential is not a part of this equation. This is one of the key differentiators of the FKX method: velocities rather than velocity potentials are used. This approach lends itself well to coupling with RANS methods, which use only velocities as well.

The current coupling method will be explained in more detail in Chapter 5. It is helpful, however, to point out some of the features of the method here. The coupling method relies on an overlap of the panel and viscous domains. A surface in the RANS domain which lies between the inner and outer surfaces of the RANS domain is used as the inner surface of the panel domain. The surface S^i serves as this inner surface of the panel domain. Velocities on this surface are used by the FKX code to determine the velocities at the outer boundary of the RANS code.

3.4 Modifications to FKX

As with the IFLOW code, great care was taken to limit the number of modifications to the FKX code to couple it with the other codes. The resulting coupled system of complex computer programs is therefore much easier to maintain.

Several minor modifications were made to the FKX code, but a sophisticated generalized computer program was developed to carry out the majority of the tasks associated with coupling FKX with IFLOW as well as with the GRID code described in the next chapter.

The modifications to the FKX code were confined to the input and output routines such that

Because the FKX code uses velocities rather than velocity potential the coupling of the FKX and IFLOW codes was made easier.

Chapter 4

Numerical Grid Generation Method

4.1 Introduction

The third major computer code involved in the new method presented here is responsible for generating the three-dimensional numerical grids that are used by the two flow solvers. The code used here is called GRID and was developed by the author specifically for the current research.

As mentioned previously, numerical grid generation is one of the biggest if not *the* biggest bottleneck in CFD simulations. Grid generation is tedious and time consuming in part because commercial grid generation software demands that users intervene to make even the smallest modifications to the generated grids.

RANS analyses are becoming faster, cheaper and more robust every month. So much so that RANS codes can now perform parameter studies on grid resolution, geometry and flow conditions such as speed, depth and angle of attack. However, without an easy way to modify an existing grid or to generate a new grid it would be impossible to perform these parameter studies.

The GRID numerical grid generation code was developed to address these issues. GRID attempts to obviate the need for human intervention to the greatest extent. As a result, GRID can be used to generate thousands (or more) of unique two and

three-dimensional numerical grids.

GRID was used to generate each of the several thousand unique, three-dimensional, structured grids used in the current research.

4.2 Traditional Approach to Grid Generation

The common method used to generate numerical grids for RANS calculations begins with a geometry. For example, to generate a grid for a body of revolution one would begin with the offsets, e.g. the radius at a number of longitudinal coordinates (r vs. x). These offsets would be loaded into graphical user interface (GUI) driven numerical grid generation software and a grid would be generated by first fitting the offsets with some sort of spline, distributing points along the body, defining the size of the grid domain and the spacing required in the three coordinate directions.

Grid points would then be distributed along the twelve edges of the computational domain. Two-dimensional grid generation methods such as transfinite interpolation or elliptic methods would be used to create grids on the six faces of the computational domain. Finally, a three-dimensional volume grid generation method would be used to create the volume grid. For a complete discussion of traditional numerical grid generation see Thompson [8].

If, during the course of the investigation, the offsets of the body were to change the grid would need to be regenerated by the user interactively. To change the number of grid points in any direction would also require interaction through the GUI. If the grid were used in a RANS calculation and were found to be inadequate, e.g. there was not enough resolution near the body or the domain size was too small, the grid would be regenerated through the GUI. If a grid sensitivity study were to be performed each grid in the study would be generated through the GUI.

In brief, if the traditional approach to numerical grid generation is employed *every* modification to the grid requires human interaction with the GUI driven software. Human interaction is not only slow, but it is a potential source of error.

Typically, it requires anywhere from several hours to several days to complete the

first numerical grid after the offsets have been defined. It then requires from minutes to hours to make each of the above described modifications.

Most of the steps described above are repeated many times while using CFD techniques to study the performance characteristics of a geometry. Repetition is almost always an opportunity for automation with the help of a computer program. It is this repetitive characteristic of numerical grid generation methods that is exploited in the current research to dramatically improve the efficiency of numerical grid generation. In other words, every possible repetitive task is automated in the GRID computer program.

In the current research several thousand grids were generated. Therefore, it was not practical to use the traditional approach to numerical grid generation. Fortunately, it was possible to automate every one of the above described steps such that generating several hundred grids was no more labor intensive than generating one or two grids. The act of automating each of the above steps resulted in a new grid generation code and that employs a unique grid generation method. This new method is described in the next sections.

It is of interest to note that GUI driven software seldom runs on supercomputer platforms like Crays where RANS codes are usually executed. Therefore, each time a grid is generated or modified it must be transferred from the grid generation platform to the RANS platform. Even with the current high bandwidth communications available, grids of many megabytes can be slow to transfer. Additionally, because binary data is often platform dependent, grids are most often saved and transferred as ASCII formatted files, which are much bigger than binary files. Finally, due to security issues it is often impossible to execute a file transfer without human interaction.

The new grid generation method avoids the problem of transferring large grid files by doing away with the GUI and running on whatever platform the RANS code runs on.

4.3 The Current Approach to Grid Generation

As mentioned above every possible attempt was made to automate the grid generation process. In so doing a new grid generation method was developed. This method is best described as a parametric method because nearly every step in the grid generation process has been described by a parameter. These parameters are included in a simple ASCII input file. Therefore, changing the input file and executing the GRID code creates a new grid.

For example, to change the number of grid cells in one of the coordinate directions requires a simple modification to a number, i.e. parameter, in the input file. The same procedure is used to change many other characteristics of the grid including: the distribution of grid points, geometry, domain size and body angle of attack.

Since the parameters are included in an ASCII file, they can be changed with any number of computer programs. Therefore, changing the grid can be automated.

The most difficult and time consuming aspect of the current grid generation process is to parameterize the geometry. Parameterizing the geometry is accomplished by writing or modifying subroutines in the GRID code. This is explained in more detail later. After a geometry is parameterized it becomes possible to substitute other similar geometries with only a very small amount of additional work. It also becomes possible to switch from one geometry to the next, e.g. SUBOFF to Albacore by changing the geometry parameter in the input file.

The benefits of this method are great. No longer is human interaction required for any but major changes to the numerical grid. Since major changes are seldom made once a grid topology is settled upon, human interaction is almost completely unnecessary in order to perform parametric studies involving the grid.

In fact, when a geometry such as a body of revolution has been parameterized it is suddenly possible to generate grids for bodies of revolution of virtually *any* geometry.

Never before has it been possible to generate so many grids so quickly. In fact, once a grid has been set up in the GRID code one can generate a virtually unlimited number of grids with no human interaction whatsoever.

4.4 Semi-automatic Grid Generation

Some human intervention is required at some point in the process of generating a numerical grid. The method employed here requires that this intervention take place at the very beginning of the grid generation process by writing software, but that little or no intervention is required thereafter. Thus, the term "semi-automatic" rather than "automatic" is used here to describe this method.

The geometries considered in the current research are all submarine-like bodies. Several configurations were analyzed including: bare hull, bare hull plus sail, bare hull plus stern appendages. Two bare hull geometries were considered: SUBOFF and Albacore.

Fundamentally, all structured grids are very similar to each other. Grids can be described parametrically such that they are virtually indistinguishable from each other. Grids are often described in a parameter space like i-j-k space rather than x-y-z space. Here i, j and k correspond to the three boundary fitted computational coordinate directions, while x, y and z correspond to the three cartesian coordinate directions.

Figure 4-1 illustrates the difference between computational and physical space and how one maps to the other. An important observation to make here is that the computational space does not indicate the geometry. In other words, the geometry could have been the SUBOFF bare hull, a prolate spheroid or virtually any other body of revolution.

For example a two-dimensional c-grid[1] around a hydrofoil section would be described in parametric or computational space as being a rectangle. A three-dimensional c-h-grid around a wing would be described in parametric space as a cube. It is easy to see that if the shape of the hydrofoil or wing changes only slightly the parametric

[1]A two-dimensional single block grid is typically described as a c, o or h-grid. The letters correspond roughly to the physical shape of the grid. A two-dimensional grid around a hydrofoil that starts at the outflow boundary, sweeps forward and wraps around the foil and ends at the outflow boundary is a c-grid. Three dimensional grids are typically described as combinations of the these three types of grids. A three-dimensional grid might be a c-grid in the i-k plane and an o-grid in the j-k plane. It would then be called a c-o-grid.

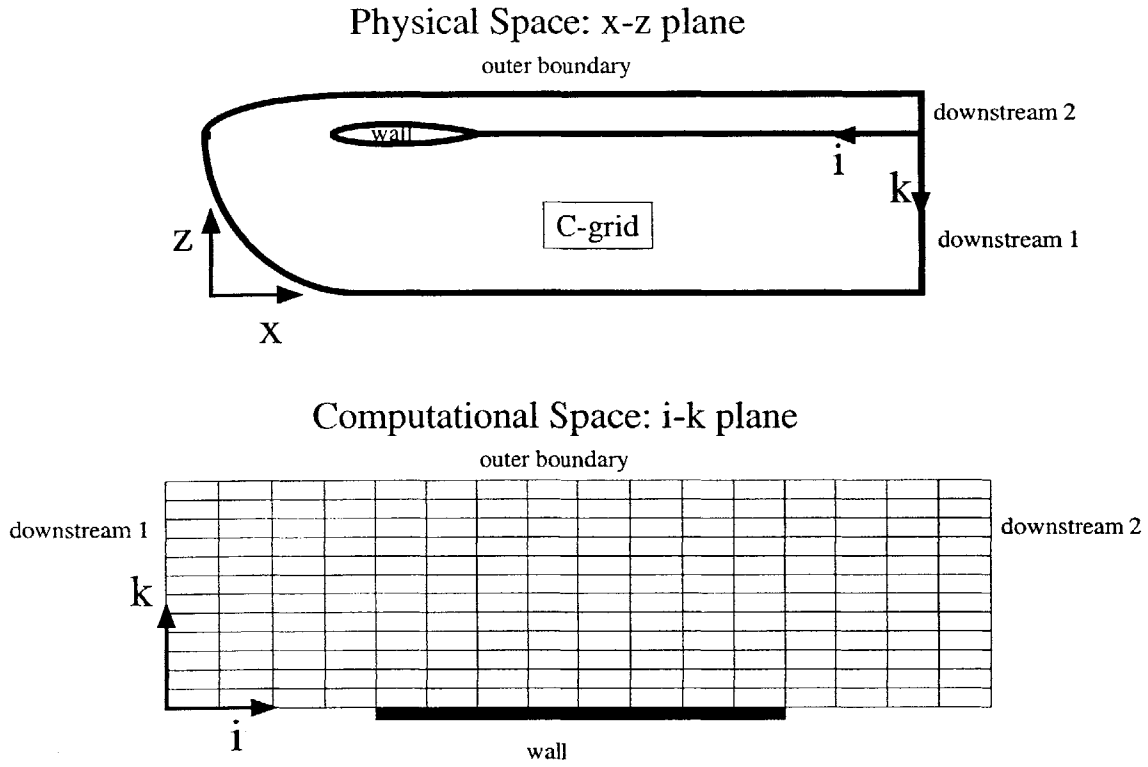

Figure 4-1: Computational space versus physical space for the body of revolution configuration.

description of the grid wouldn't change at all, i.e. a grid for a NACA0012 hydrofoil would be parametrically identical to a grid for a NACA0016 hydrofoil.

It follows that a grid for the SUBOFF bare hull can be made to be parametrically identical to a grid for the Albacore bare hull. That is exactly what GRID does whenever possible. In other words, geometry is a *parameter* in the GRID code. Switching from one geometry to the next is as simple as changing a flag in the GRID input file.

These geometries are supplied either through input files or by writing extensions to GRID's integrated geometry library.

4.5 Grid Configurations

Each grid configuration must be built into GRID by writing extensions to the GRID code. In this research submarine configurations were built one step at a time. For example, the first configuration considered was the bare hull. Then a configuration was built that added the sail. Then another configuration was built that added stern appendages and so forth. Modifications were made to allow for variations in the angle of attack and size of the grid domain.

This is, no doubt, the single biggest drawback of this method. Writing such code can be difficult and tedious. The benefits described here, however, far outweigh the difficulty of writing such code. In other words, generating one grid is still a bottleneck, but once it's generated a virtually unlimited number of variations can be made to it with ease.

Once a configuration is built into GRID, it is reasonably simple to add another geometry through modifications to the geometry library or to make modifications to a geometry through input files. For example, the submarine bare hull configuration allows users to swap in *any* submarine-like geometry. Currently, there are 6 submarine-like geometries built into the library.

It is also easy and straightforward to make modifications to a geometry once it's in the library. For example, through the GRID input file it is possible to modify the length of the parallel middle body of every submarine-like geometry. The position, span, chord length and angle of attack can be modified for configurations with stern appendages.

It should be noted that, commonly, the angle of attack, AOA, of a submarine is not changed in the grid. Coordinate transformation within the RANS code make such changes simple. However, this was not possible here due to the presence of the "fixed" free-surface. In other words the AOA of the submarine was modified with respect to the free-surface.

Modifying the AOA *automatically* required great care due to the challenge of keeping grid lines from crossing. In particular, as the depth diminished the domain size

necessarily became smaller making changes to the AOA troublesome. Nonetheless, variations in the AOA between $\pm 4^{\circ}$ were done for each geometry considered and at all depths considered.

4.6 Summary of Method

Note that no mention has been made of GRID being a *completely general* grid generation code. There is little hope of such a code being developed in the near future. Instead, GRID is focused on being a completely general *submarine* grid generation code. (Previous work on GRID by the author also included surface ships and several other types of grids.)

The grid generation procedure used by here can be summarized as follows:

- Define the commonalities of all grids. For example:
  1. Domain size
  2. Sub-domains or blocks
  3. Number of grid points in each direction in each sub-domain
  4. Spacing of grid points in each direction in each sub-domain
- Abstract the geometry of interest into the fragments that make it up. Examples of fragments:
  1. bow
  2. stern
  3. sail
  4. stern appendages
- Abstract the fragments into the parameters that define them. Examples of parameters:
  1. length

2. height

3. shape

4. position with respect to a reference

- Place all parameters in an easily modifiable ASCII input file.
  - This is critical for performing automated parameter studies.
- Write computer code that generates the fragments which are now independent of the underlying geometry.
- Write modifications or enhancements to the integrated geometry library.
- Put the bits and pieces together to make a complete 3-D numerical grid.

4.7 Parameter Studies

Obviously, if all that is required to change a geometry is a modification to an input file then these changes can be made automatically with little extra effort by using utilities that can modify these input files. In the present research UNIX shell scripts were used along with the sed[2] command to modify the parameters in these input files to accomplish the parameter studies presented herein.

The following parameters were varied for the current research:

- Configuration - bare hull, bare plus sail, bare hull plus stern appendages
- Geometry - SUBOFF, Albacore
- Domain size - as depth decreased the viscous domain size decreased so as not to intersect the free-surface

[2]sed is the UNIX "stream editor" command. It takes as arguments editing commands and a filename. It then executes the editing commands on the named file. A typical command in the present research would cause a parameter in the file to be changed from one value to another.

- Grid resolution - to automate grid convergence studies, the number of grid points in each direction can be changed automatically
- Grid spacing - as domain size changes the grid spacing must change
- Angle of attack - with respect to the free-surface
- Parallel middle body - length

The following parameters can be varied in GRID via input files for the geometries considered here. In other words, no modifications need be made to the geometry library itself to accomplish the following changes:

- Sail shape, span, width, chord length, position
- Stern appendage shape, span, width, chord length, position
- Hull radius
- Bow length
- Stern length

In addition several other configurations are available for each of the geometries under consideration. They are:

- Bare hull with sail and stern appendages
- Articulated stern planes - with flap and with flap and tab, i.e. two and three pieces
- Bare hull with bow planes
- Moving free-surface - for nonlinear, viscous free-surface calculations
- Inside water or air tunnel

4.8 Summary

A robust, semi-automatic method for the generation of numerical grids was developed. This method allows for the generation of grids for several submarine configurations, including bare hull, bare hull plus sail, bare hull plus stern appendages. The method is generic in the sense that different geometries can be easily substituted for each configuration, e.g. SUBOFF and Albacore.

The grid generation method allows many parameters to be changed automatically, i.e. without human intervention. Parameters that can be changed automatically include grid resolution, grid spacing, domain size, geometry, configuration, and angle of attack.

The generic and automated nature of the code allow it to be used for parameter studies like those described in later chapters.

Since typical CFD publications include on the order of three or four numerical grids and the current publication includes approximately 640 unique three-dimensional grids, the current grid generation method is believed to represent an improvement in efficiency of approximately two orders of magnitude over traditional grid generation methods.

In fact, the current method is so robust and efficient that a new numerical grid was generated for *every* condition studied, and over three thousand conditions ere studied. Approximately one in five of these conditions required a unique grid. However, it was simply easier to generate a new grid every time the conditions changed. This resulted in 640 unique grids, but each of those was generated approximately five times.

Chapter 5

Coupling Method

5.1 Introduction

In the present research the GRID, IFLOW and FKX codes have been coupled. As mentioned previously the IFLOW and FKX codes were chosen because they have been extensively validated and because they are both extremely robust and efficient. The GRID code was developed here to those same standards so that there would be no weak links in the coupled method. Since there were no weak links, the resulting coupled method shared those same characteristics.

A great deal of effort was made to validate and verify the new method. In fact, several thousand three-dimensional computations were made for five different geometries subject to many different flow conditions.

5.2 Method

The coupling was accomplished by decomposing the flow field into viscous and inviscid parts. Velocities calculated by the RANS code in the viscous domain are provided to the panel code in the inviscid domain as boundary conditions and vice versa. This process is repeated until the solution is converged. By overlapping the viscous and inviscid domains the two codes can communicate with each other. Thus, the inner viscous domain also includes some portion of the inviscid flow field. The results from

this research indicate that the calculation of forces and moments is not very sensitive to how the two domains overlap as long as the overlap region does not include the boundary layer.

A schematic of the flow domain is shown in Figure 5-1. The two flow codes communicate via velocities calculated at their common boundaries. The RANS code provides velocities to the panel code at the inner panel boundary, and the panel code will provide velocities to the RANS code at the outer boundary of the RANS domain as well as on the free-surface. Conceptually, it may be useful to consider the surface represented by the dashed line in Figure 5-1 as the body in the inviscid domain.

To couple two or more methods or computer programs it is necessary to translate the output of one into the input of the other. One way to do this is to modify each of the computer programs to conform to the requirements of the others. A problem with this approach is that the best codes for this type of research are the technologically most advanced and, therefore, necessarily research code. Research codes are by definition constantly under revision. If the input/output scheme of one of the codes is changed the above mentioned revisions must be made again. Thus, maintenance of coupled research codes can be problematic. There seems to be little that can be done about this problem unless some industry standards are established for input and output of CFD codes.

Great care was taken to modify each of the three major codes as little as possible. In fact, the coupling was accomplished through the input and output of each code rather than by directly linking each code. In other words, the coupled codes remained as independent as if they were uncoupled. The output of one code was used to create the input for the next. There were no direct links in the source code from one code to the next. There are several very important advantages to keeping the codes separate in this fashion.

- Faster development time
- Easier to update individual codes
- Easier to maintain the necessarily huge and evolving code base

- Less memory used during calculations

The one serious drawback to this method is the need to read and write many large data files during a single computation. This drawback was mitigated by the fact that less than 2% of the CPU time needed to accomplish a complete, coupled calculation was spent in the reading and writing of files. This is due in part to the very fast storage devices used by Cray computers and in part by the large amount of CPU time needed to solve the RANS equations.

Several small computer codes were developed to translate the output from one code into the input of the next code. Generality was emphasized while developing each of these smaller codes to make them as parameter independent as possible, i.e. independent of geometry or flow condition.

5.3 Implementation

The implementation of the method is outlined below.

1. Define parameters governing the flow such as depth, speed, geometry, and angle of attack.

2. Define viscous inner (RANS) and inviscid outer (panel) domains.

3. Generate numerical volume grid for the inner RANS domain (shaded region in Figure 5-1).

4. Generate numerical surface grid (panels) defining free-surface for the outer panel domain.

5. Generate a surface grid on the inner boundary for the panel code.

6. Compute the flow in RANS domain.

7. Use RANS velocities at common boundary shown by *dashed* line in Figure 5-1 as boundary condition for panel domain.

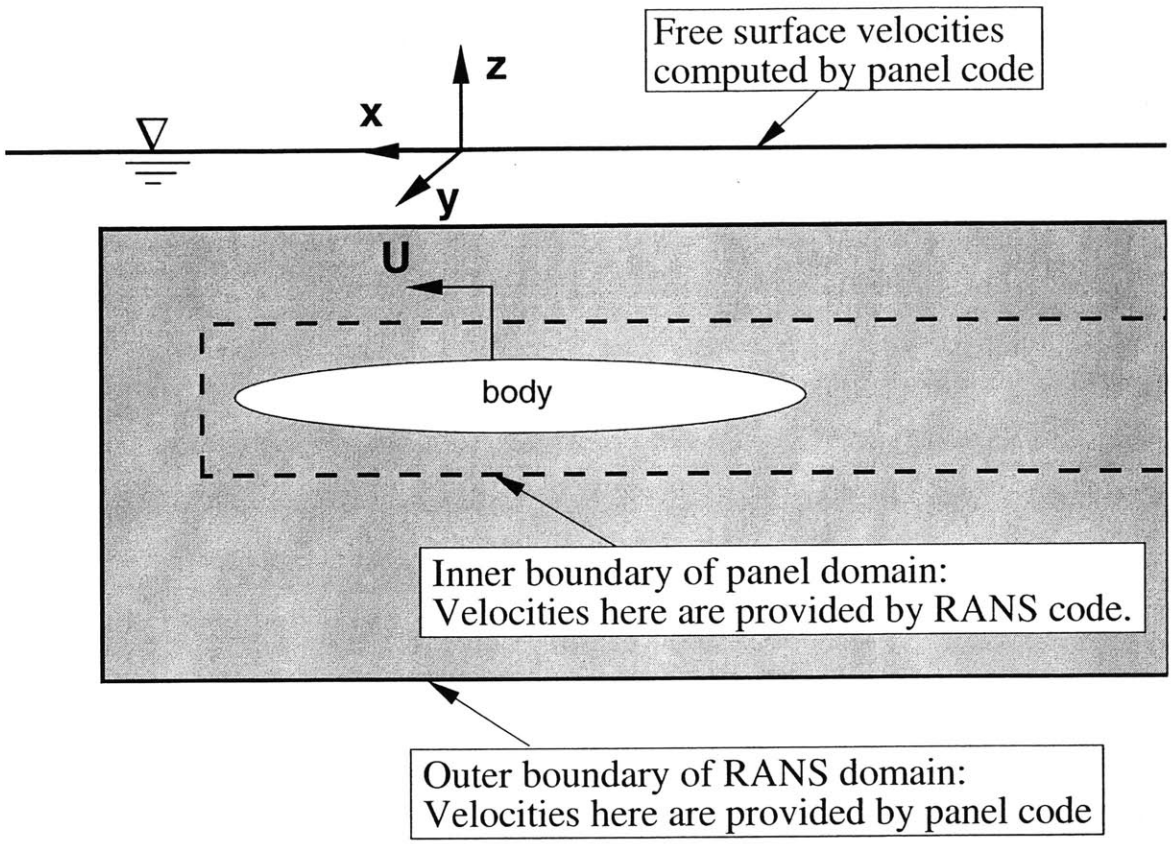

Figure 5-1: Schematic illustrating inner and outer flow domains for a submarine operating near the free-surface. The inner domain is shaded. The outer domain encompasses everything outside the dashed line and under the free-surface.

8. Compute flow in inviscid domain with panel code.

9. Update velocities at the outer boundary of RANS domain with the inviscid solution from step 7.

10. Repeat steps 5 thru 8 until solution is converged. (see discussion below regarding convergence criteria)

11. Compute hydrodynamic properties including forces and moments and surface wave elevations.

12. Repeat steps 1-10 until all speeds, depths, angles of attack and geometries are considered.

Conventional convergence criteria were used to determine the number of RANS/panel couplings. The root mean square of the pressure residual was required to drop by 4 to 5 orders of magnitude before a calculation was declared converged. In the present research steps 5 thru 8 were repeated 5 times, which was adequate to satisfy the imposed criteria. Each RANS iteration consisted of 40 iterations for a total of 200 RANS iterations and five FKX calculations for each condition.

A sophisticated UNIX shell script was created to manage the entire coupling process. This script consisted of commands to execute the grid, RANS and panel codes as well as several codes that assisted in the coupling of each. In addition the script was used to cycle through the various sets of parameters studied here, such as geometry, speed, depth, grid resolution, etc.

Since the GRID, IFLOW and FKX codes are all serial codes and since the author had access to a multi-CPU Cray computer, several shell scripts were run in parallel such that parametric studies were accomplished in a minimum amount of time.

Chapter 6

Geometries, Grids and Domains

6.1 Introduction

As with any new method it is essential to make every effort to validate and verify the method with theory and or experimental data under as many different conditions as possible. This is the only way to understand the limitations of the new method. A great deal of work was devoted to verification and validation in the current research. An unusually large number of geometries and flow conditions were considered. Each of the five geomtries and a few of the grids and domains used are presented in this chapter.

All geometries and grids were generated using the GRID numerical grid generation code described earlier in Chapter 4.

Due to time and resource limitations it is never possible to exercise any method under every possible condition. However, a significant step toward validation and verification of the current method was made here. Procedures used to conduct verification and validation have been established by Roache[20]. These procedures include grid and iterative convergence studies as well as comparisons with experimental data.

Five three-dimensional geometries were considered based in part on their relevance to the research and in part on the availability of theoretical and experimental data with which to validate the numerical method. Grid insensitive solutions were obtained for each under a wide variety of conditions including changes in depth, speed and angle

of attack, i.e. the solutions did not change significantly with increased grid resolution all else being the same.

6.2 Geometries

The five geometries used were the SUBOFF bare hull, the SUBOFF with sail, the SUBOFF with four stern appendages (no sail), the Albacore bare hull and the Albacore with four stern appendages (no sail).

The geometries considered here are shown in profile in Figure 6-1 and Figure 6-2. Figure 6-1 shows the geometries *without* lifting tail surfaces. Figure 6-2 shows the geometries *with* lifting surfaces. These geometries were chosen due to the availability of force and moment measurements which were used to verify the current method.

Detailed descriptions of the characteristics of the SUBOFF geometries and experimental setup can be found in Roddy [21]. Descriptions of the Albacore geometries and experimental setup can be found in Dempsey [7].

6.3 Domain

The computational domain for the Albacore bare hull in an infinite domain, i.e. not near the free-surface, is shown in Figure 6-3. In physical space the x-direction corresponds to the longitudinal axis of the hull and increases from bow to stern, the y-direction is the transverse direction and is positive to starboard, the z-direction forms a right hand coordinate system and is positive in the upward direction. The origin of the physical coordinate system is at the bow of the submarine.

In computational space the i-direction runs along the body in the longitudinal direction, the j-direction starts at the top of the submarine and traverses the azimuthal direction, and the k-direction starts at the body and is roughly normal to it. The origin of the computational coordinate system is also at the bow of the submarine.

The grid is made up of a c-grid[1] in the longitudinal-body normal (i-k) plane and

[1]See Chapter 4 for a discussion of c, o and h grids

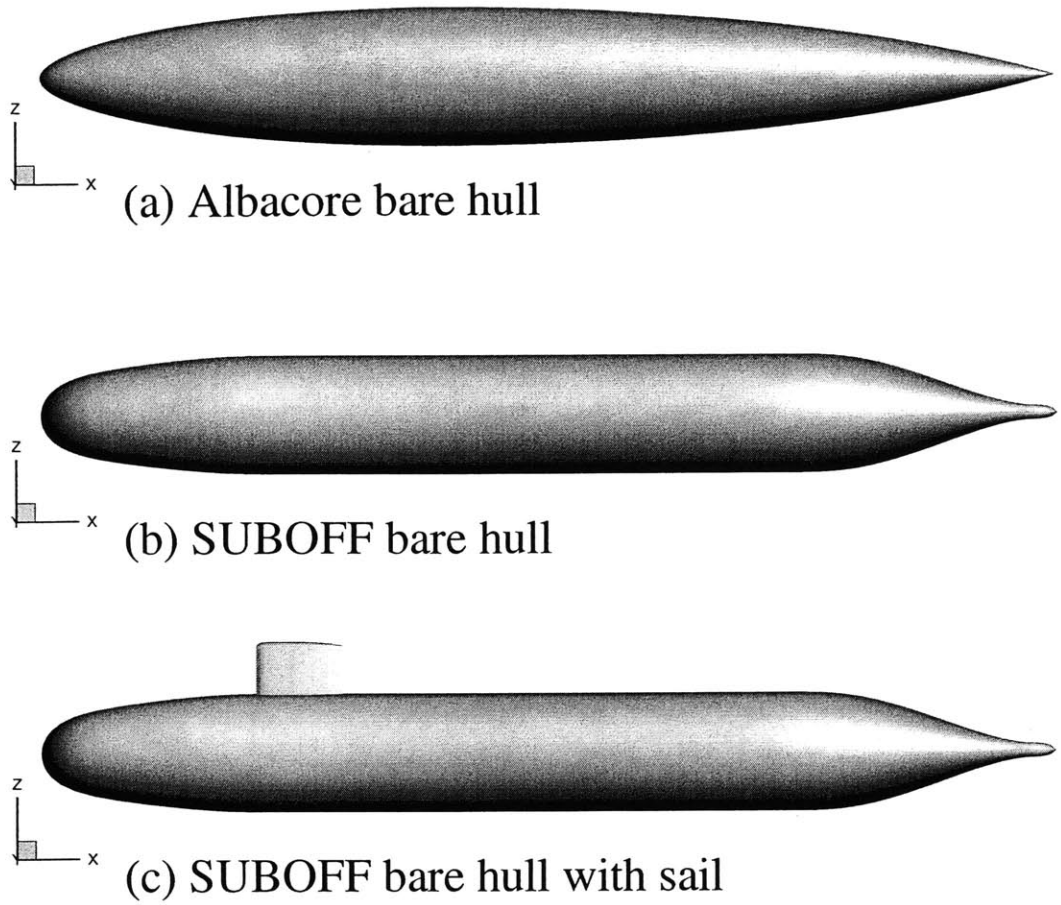

Figure 6-1: Geometries considered in the present research *without* lifting surfaces.

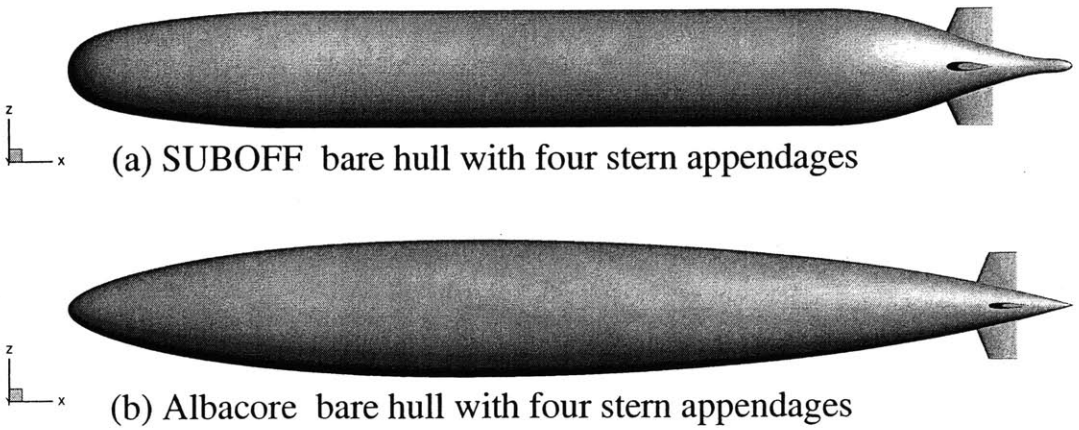

Figure 6-2: Geometries considered in the present research *with* lifting surfaces.

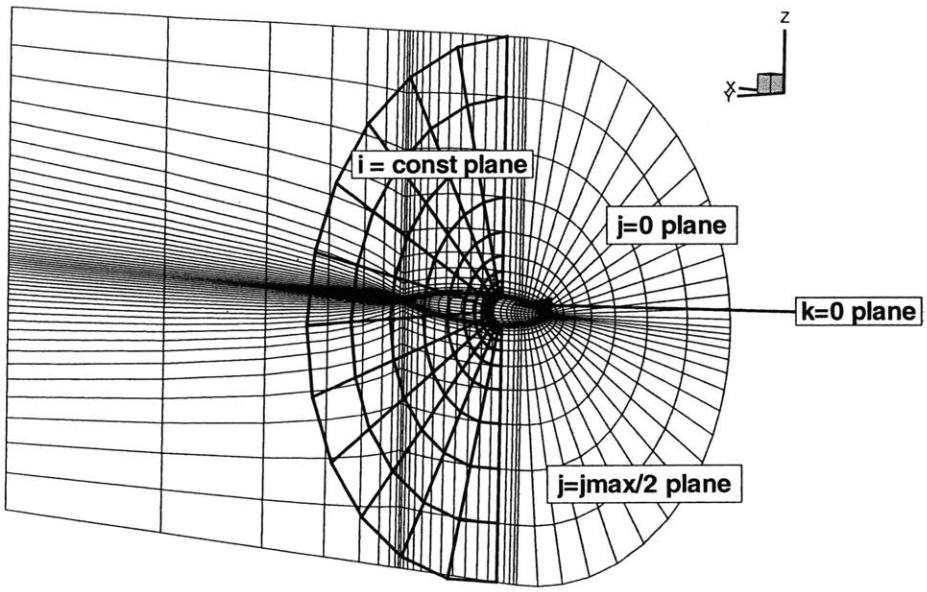

Figure 6-3: Domain: Coarse grid (40 x 24 x 24) for the Albacore bare hull in an "infinite" domain.

an o-grid in the azimuthal-body normal (j-k) plane. All other grids for all other geometries conform to a similar topology.

Figure 6-4 shows the coordinate system used.

6.4 Grids

Three parameters were varied that made it necessary to generate a large number of numerical grids:

1. Grid resolution
2. Body Depth
3. Angle of Attack

The remainder of this section serves to illustrate just a few examples of the grids generated as a result of these parameter variations.

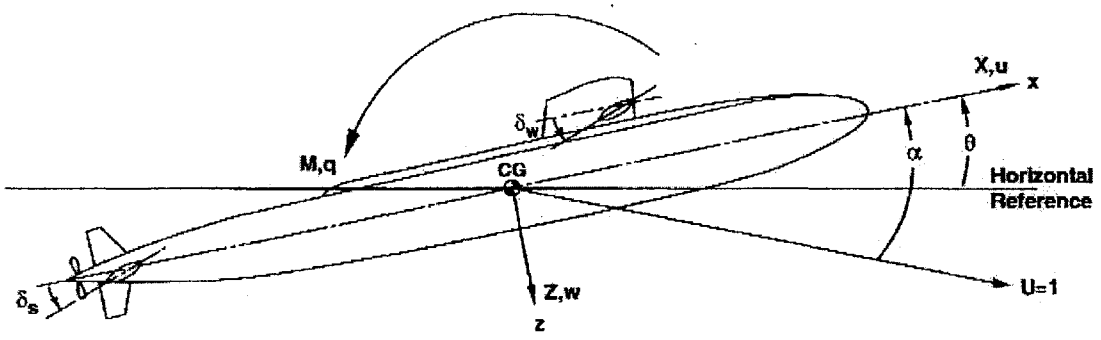

Figure 6-4: Coordinate system.

6.4.1 Grid Resolution

In the verification of any CFD calculation it is necessary to determine the dependency of the solution on the resolution of the numerical grid. If the calculations are shown to be dependent on grid resolution then they cannot be trusted. In the current research grid insensitive solutions were obtained for each of the five geomtries at a number of conditions. Due to time limitations a representative subset of the parametric study mentioned above was tested for grid sensitivity.

Three grids around the Albacore bare hull are shown in Figure 6-5.

The number of grid points listed in the figure corresponds to the longitudinal, azimuthal and body-normal directions, respectively. The solution was shown to have no significant difference when comparing the medium grid solution with the fine grid solution. Therefore, the medium grid resolution was used throughout the parameter studies presented in later chapters.

6.4.2 Body Depth

Figure 6-6 shows how grids around the Albacore bare hull varied with depth. Grid lines were not allowed to cross the free-surface as that would lead to an undefined boundary condition.

Figure 6-7 shows the effect that changing depth has on the physical domain of

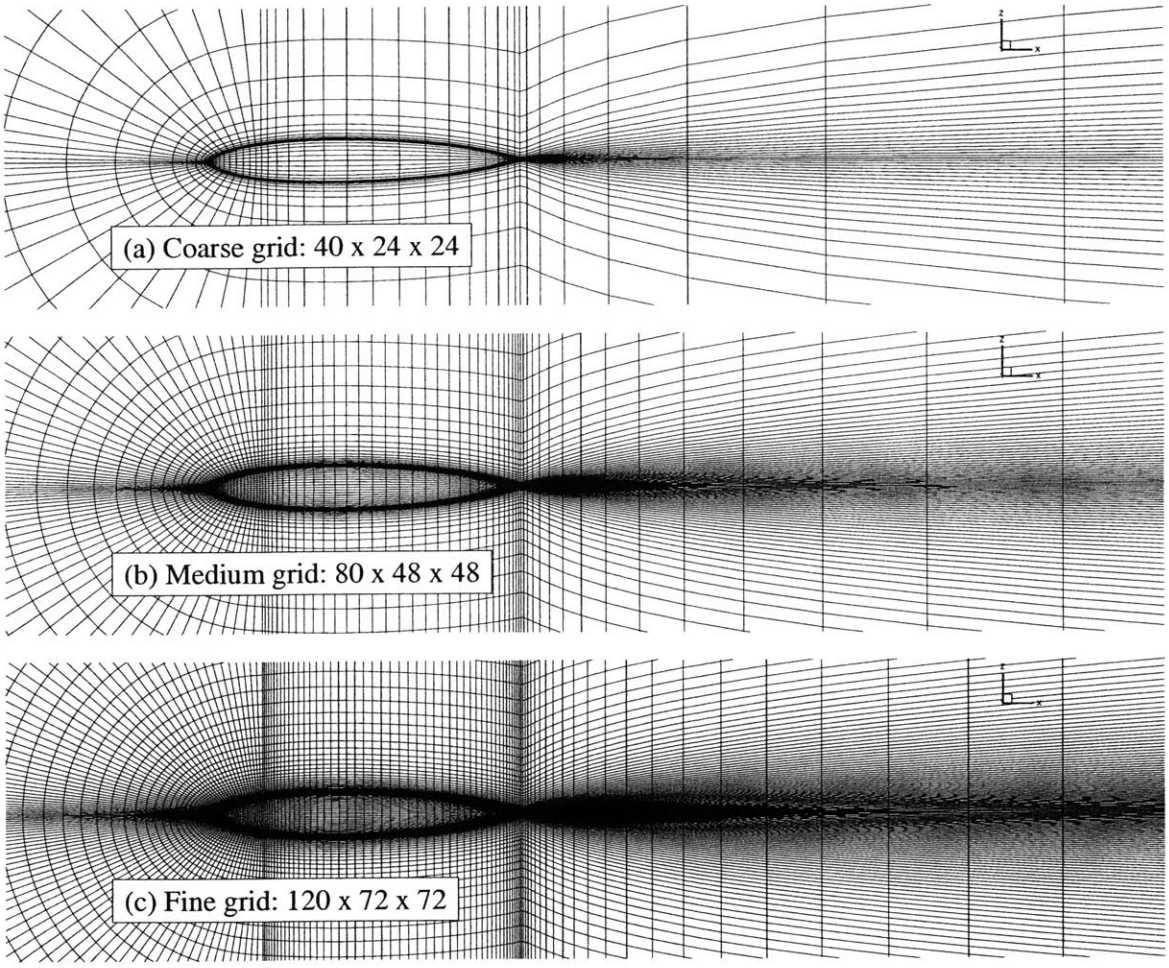

Figure 6-5: Resolution: Representative coarse, medium and fine grids for the Albacore bare hull. The grid numbers listed are for the longitudinal, azimuthal and body-normal directions, respectively.

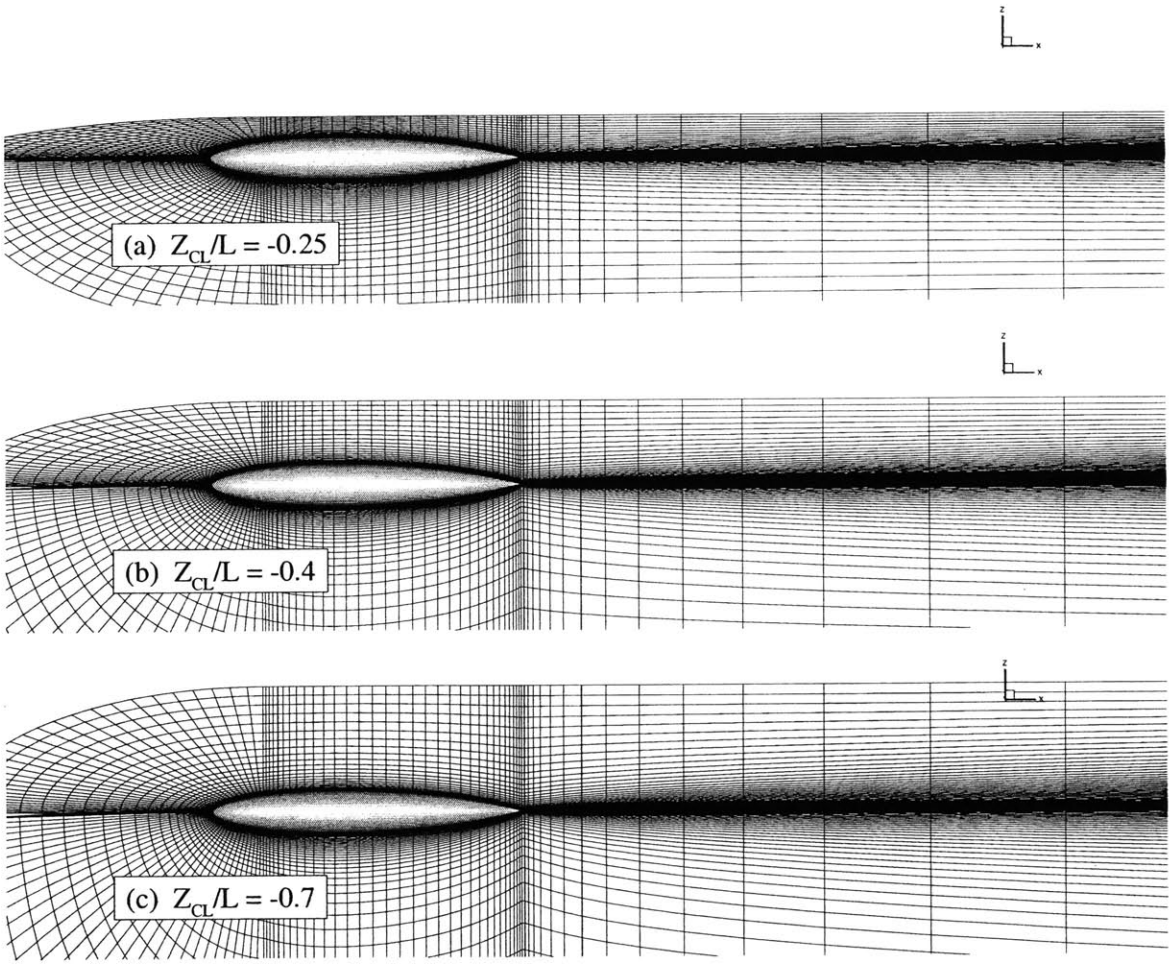

Figure 6-6: Depth: Albacore bare hull at various depths.

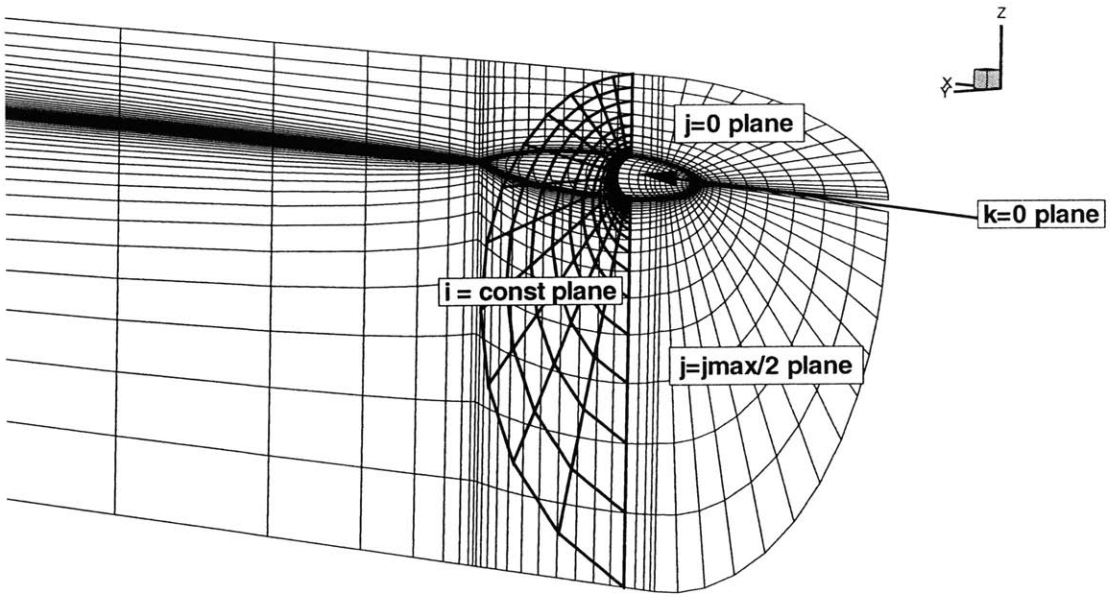

Figure 6-7: Depth and Domain: Coarse grid for Albacore bare hull with body-near the free-surface.

the solution. Great care was taken to implement a robust numerical grid generation scheme that automatically disallowed crossing grid lines as the domain size and shape changed.

6.4.3 Angle of Attack

To allow the calculation of vertical plane maneuvering coefficients it was necessary to vary the angle of attack of each geometry for all speeds and depths. This led to a complication not usually encountered in "infinite domain" calculations.

Traditional "infinite domain" calculations at angle of attack require only that the velocities at the outer boundary of the domain be transformed to comply with the angle of attack under consideration leaving the grid unaltered. In the present research this was not possible because of the relationship between the body and the free-surface. Obviously, the free-surface is "fixed" in space and, thus, the body must be rotated relative to the "fixed" mean free-surface.

That meant that a new grid had to be generated for each angle of attack. Figures 6-8, 6-9 and 6-10 shows several examples of the grids generated for the various angles

of attack.

This requirement increased the difficulty of keeping the grid lines from crossing. A simple algebraic grid generation technique was used to rotate the submarine without introducing unwelcome negative grid cell volumes. In brief, this procedure went as follows:

1. Generate entire grid at zero AOA.
2. Rotate submarine body to desired AOA.
3. Smoothly dampen the rotation of the grid surrounding the body such that no rotation occurred at the outer boundary of the grid.

6.5 Conclusion

The GRID code was used to generate thousands of unique, three-dimensional numerical grids. Parametric studies were carried out on grid resolution, grid distribution, geometry, configuration, domain size and angle of attack. The results of these studies are presented in the following chapters.

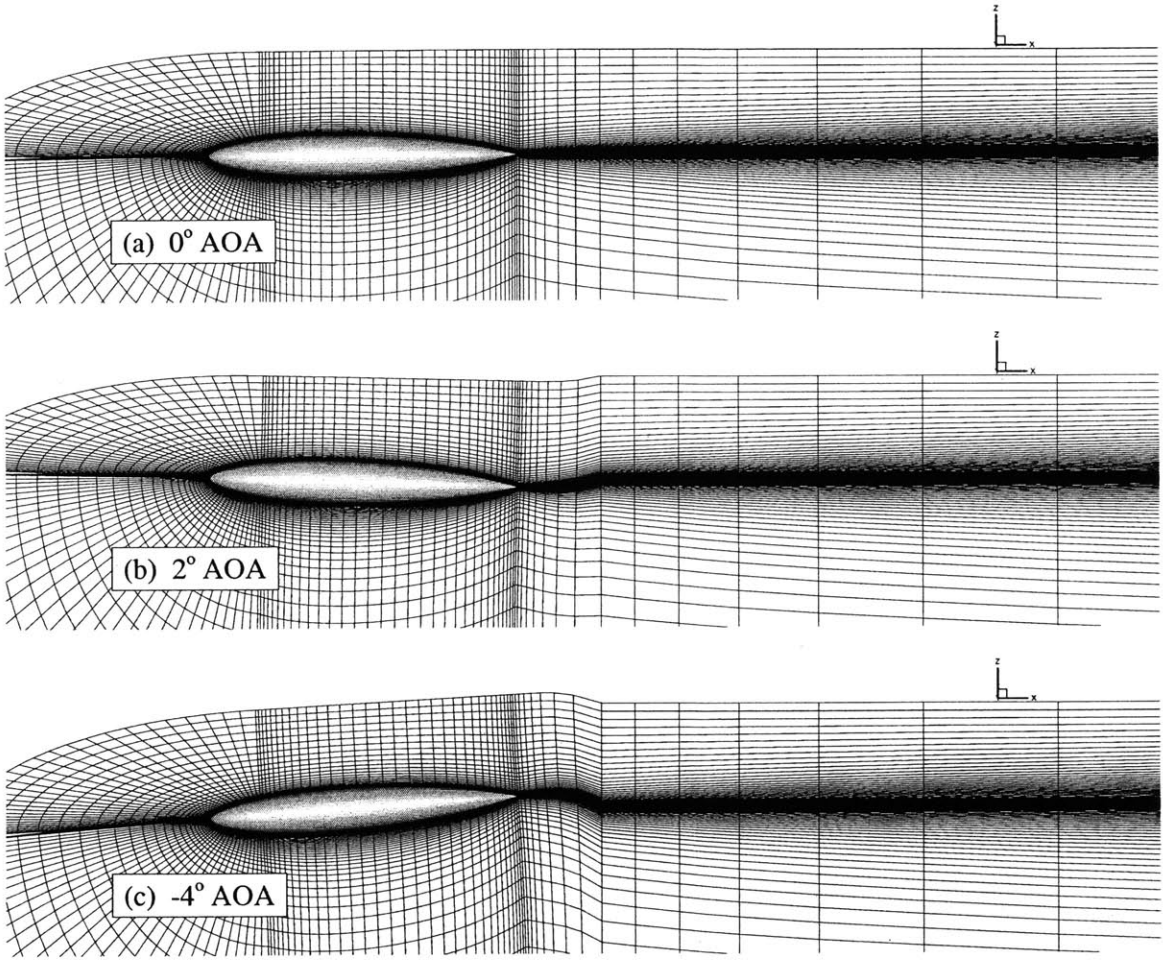

Figure 6-8: Albacore bare hull at various angles of attack and near the free-surface. All grids were generated algebraically, i.e. with no elliptic smoothing.

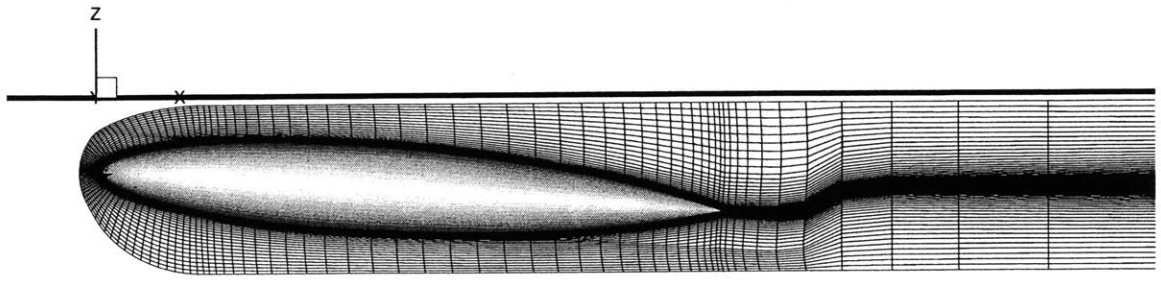

(a) Albacore bare hull, $\alpha = 4^{\circ}$, Z_{CG}/L=-0.15, 80 x 24 x 48

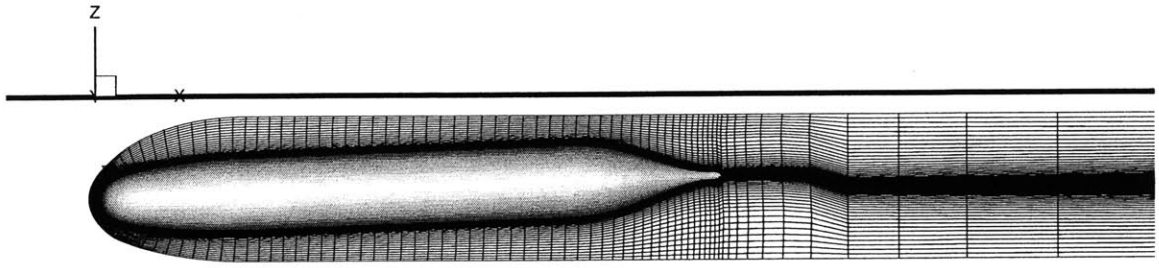

(b) SUBOFF bare hull, $\alpha = -2^{\circ}$, Z_{CG}/L=-0.15, 80 x 24 x 48

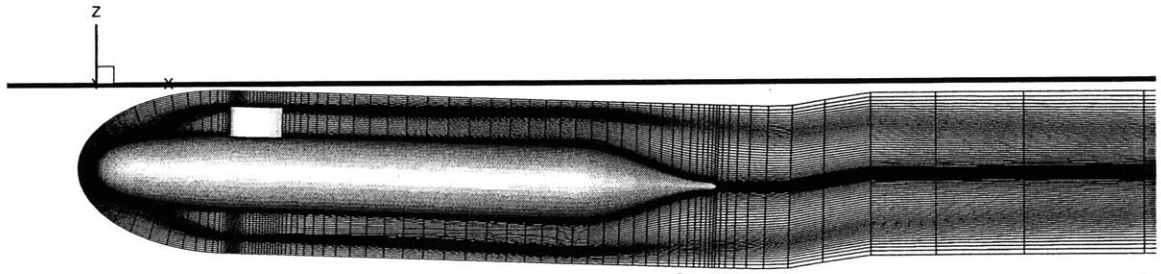

(c) SUBOFF bare hull with sail, $\alpha = 2^{\circ}$, Z_{CG}/L=-0.15, 96 x 24 x 48

Figure 6-9: The symmetry plane and bodies from some of the 3-D grids used in the present research with particularly small domains. NOTE: the thick horizontal line just above the grid represents the mean free-surface.

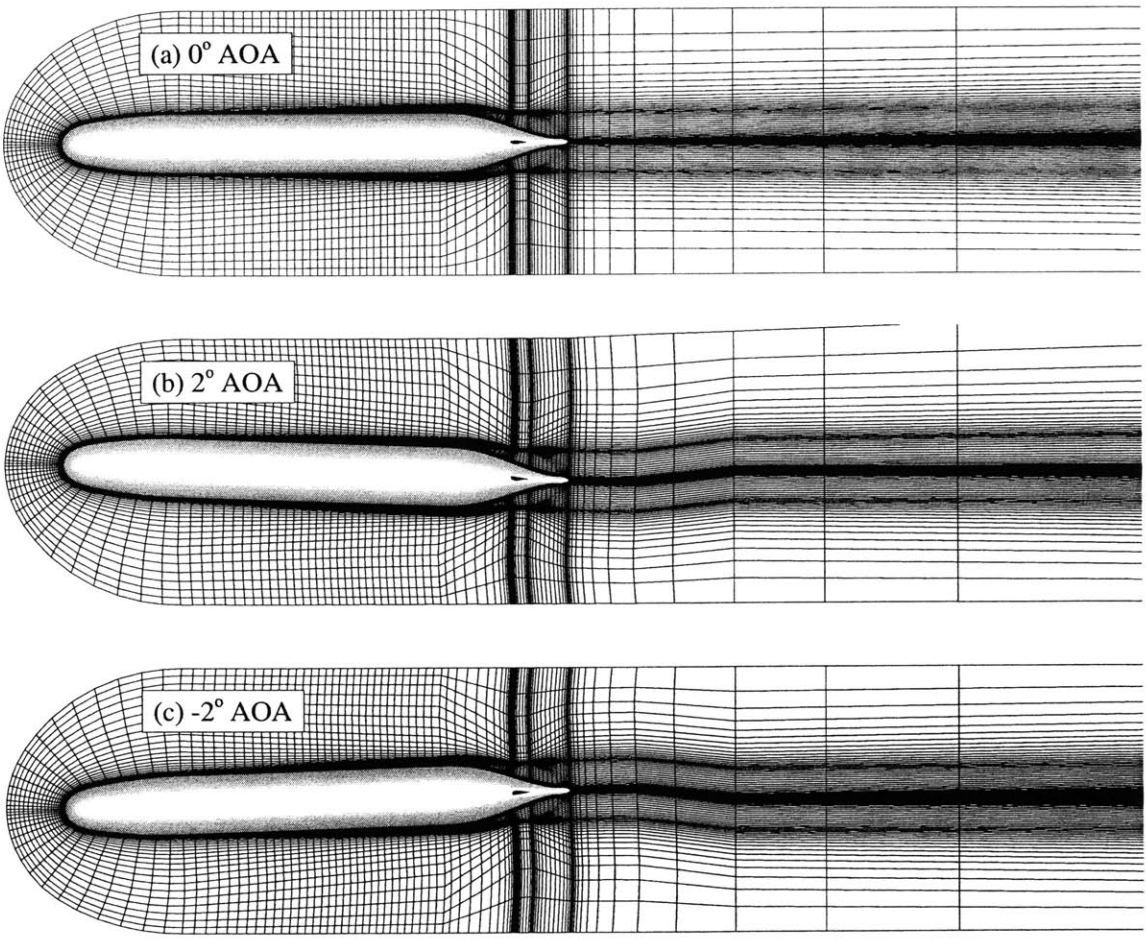

Figure 6-10: SUBOFF with four stern appendages at various angles of attack near the free-surface. Notice that the grids are identical at the outer boundary, where the coordinate transformation has been suppressed.

Chapter 7

RANS Verification and Validation

7.1 Introduction

Although a great deal of prior effort had been made to verify and validate IFLOW by Sung et al.[24], [25], [26], [27], [28], Tsai et al.[32], Huang et al.[13] and Griffin et al.[9], there remained a reasonable amount of uncertainty that IFLOW could do an adequate job of calculating maneuvering coefficients for the current research.

Therefore, a significant additional effort was made at the outset of this research to minimize this uncertainty by further validating IFLOW against available experimental data without considering the effects of the free-surface. This experimental data was taken such that free-surface effects were minimal or assumed to be nonexistent. The results of those efforts are presented in this chapter.

7.2 Iterative Convergence

Iterative convergence is measured by the log of the RMS of the pressure residual here. In general, it is essential that the pressure residual decrease by 4 to 5 orders of magnitude to establish an iteratively converged RANS solution. It is not practical for the residual to be driven to machine zero.

It should be said that iterative convergence is just as much a grid generation verification as a RANS verification. A "bad" grid can be responsible for poor iterative

convergence. There are some basic guidelines for what makes a good grid versus what makes a bad grid, but grid generation remains to a great extent an effort of trial and error. The GRID code described earlier allows for the easy redistribution of grid points and changes in grid resolution. A great many trials have been performed by the author to understand what makes a "good" submarine grid. Only a small fraction of those grids are presented here.

Figure 7-1 shows the iterative convergence for three grids at various angles of attack. Clearly, the six solutions meet the criteria for iterative convergence.

The angles of attack considered are representative of the angles of attack considered with the coupled method in later chapters. There is one important difference, however. For the RANS only calculations shown in Figure 7-1 angle of attack was achieved by transforming the angle of attack of the flow at the outer boundary. Only grid resolution was changed. For the coupled method presented in the remaining chapters, the angle of attack was changed by rotating the body of the submarine with respect to the mean free-surface. Therefore, it was important to give consideration to what makes a good grid when the body is rotated. It was also important to measure iterative convergence with these new types of grids. This convergence data is presented in the next chapter.

7.3 Grid Convergence

A series of successively finer grids were generated in an attempt to determine the sensitivity of the solution to the resolution of the grid. The goal of this type of effort is to determine the minimum requirements for grid resolution and to establish confidence in the solutions.

Relatively small grids were used throughout this research. The proper distribution of grid points is essential to using such small grids to achieve correspondingly accurate solutions. Again, many more grids were generated and tested than are presented here. It was this trial and error effort that "found" grids small enough and, therefore, efficient enough to be used in the parametric studies that necessitated thousands of

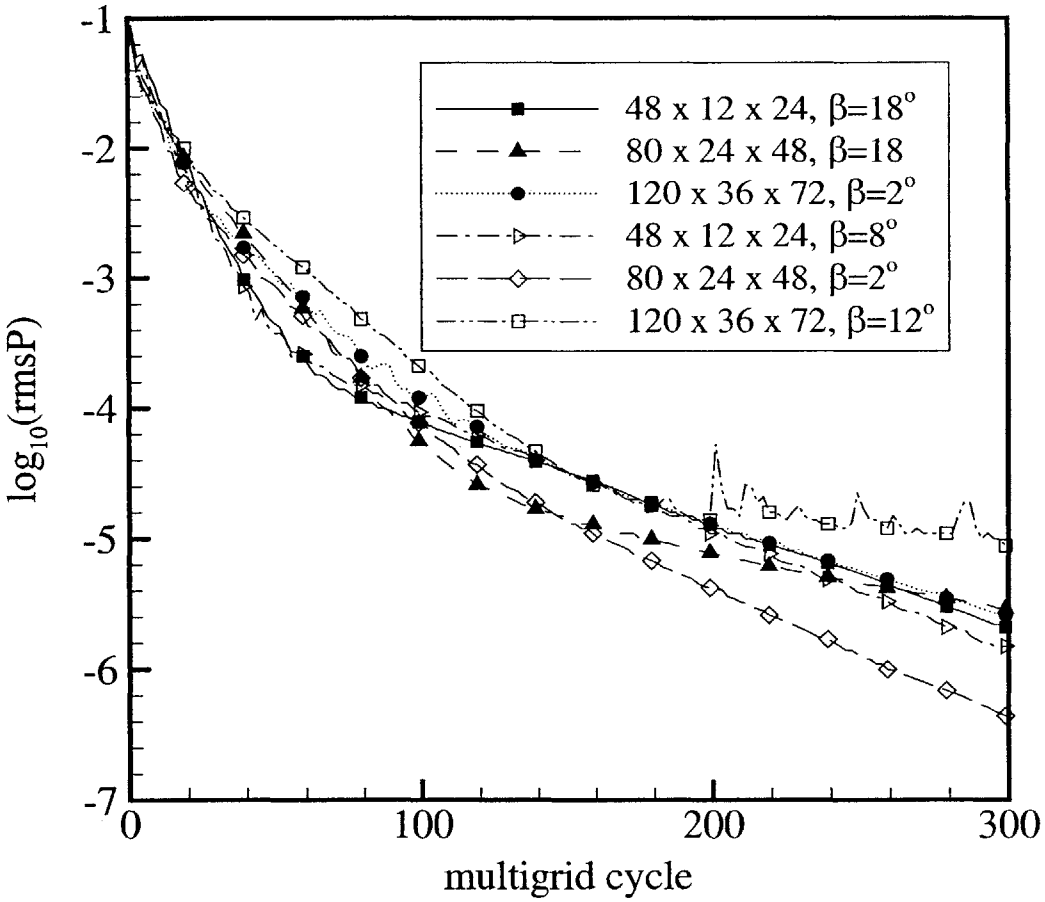

Figure 7-1: Iterative convergence for SUBOFF bare hull calculations.

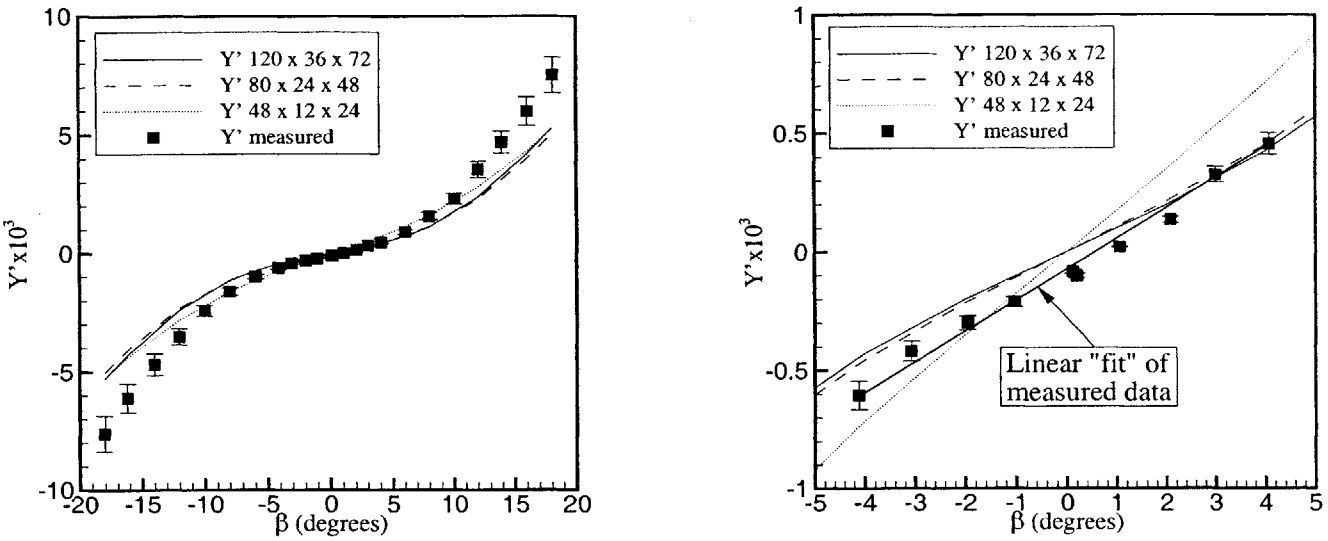

Figure 7-2: Side force vs. angle of attack for SUBOFF bare hull.

three-dimensional calculations.

7.3.1 Bare Hull

Figures 7-2 and 7-3 show the side forces and yawing moments, respectively, for a range of angles of attack for the SUBOFF bare hull. The calculations show that the RANS code is not very accurate for angles of attack larger than 10°. This is likely due to the use of the *linear* $k - \omega$ turbulence model here.

Nonlinear turbulence models available in the IFLOW code are more accurate at high angles of attack, but they are much more CPU intensive. The intent of the current research is to predict maneuvering coefficients. The maneuvering coefficients computed here require only small angles of attack. Therefore, it was determined that the linear $k - \omega$ turbulence model was adequate for these purposes.

These calculations indicate that the solutions are grid converged for all angles of attack, i.e. the solutions do not change significantly from the $80 \times 24 \times 48$ grid to the $120 \times 36 \times 72$ grid. From these calculations it was determined that the $80 \times 24 \times 48$ grid would be adequate for the free surface calculations presented in later chapters.

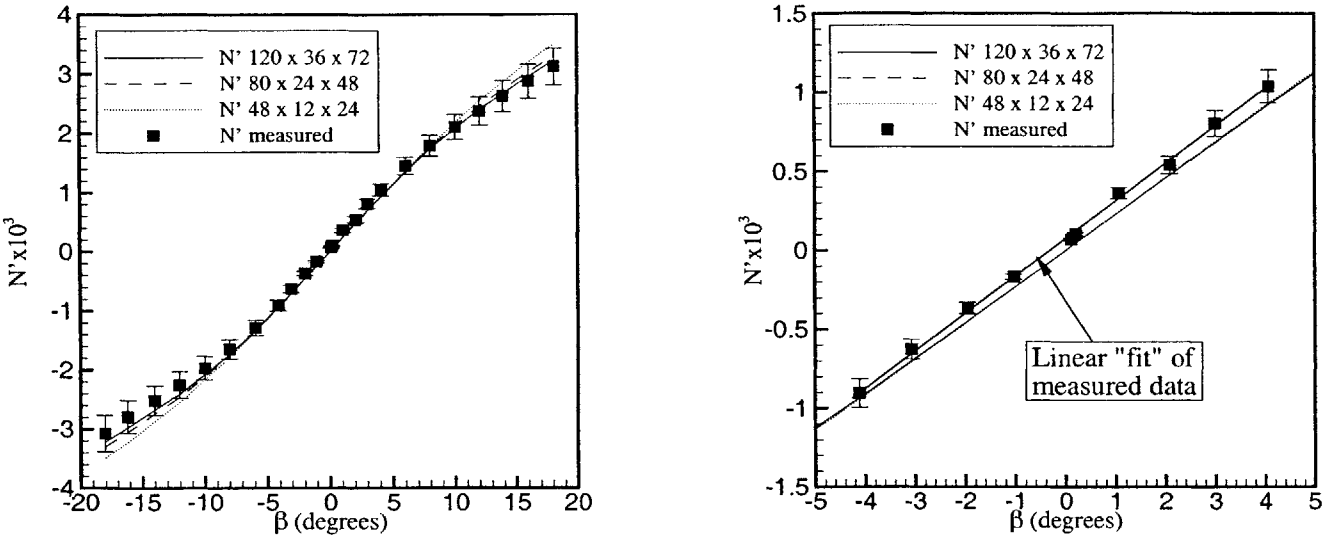

Figure 7-3: Yawing moment vs. angle of attack for SUBOFF bare hull.

7.3.2 Bare Hull with Stern Appendages

Figures 7-4 and 7-5 show the side forces and yawing moments for a range of angles of attack for the SUBOFF with stern appendages. Both figures indicate that the solution is both accurate and grid converged.

The solution is accurate in the sense that the forces and moments fall mostly within the error bars of the experimental data. It should be noted that the measurements are not perfectly symmetric for positive and negative angles of attack. The calculations are perfectly symmetric and the line representing the experiemental data is not parallel to the line representing the calculated results. This is probably due to the presence of struts and maybe even due to the presence of the free surface.

The solution is grid converged in the sense that solutions do not change significantly for all angles of attack from the $112 \times 48 \times 48$ grid to the $168 \times 72 \times 72$ grid.

From these calculations it was determined that a grid resolution of $112 \times 48 \times 48$ would be adequate for the free-surface calculations presented in the next chapters.

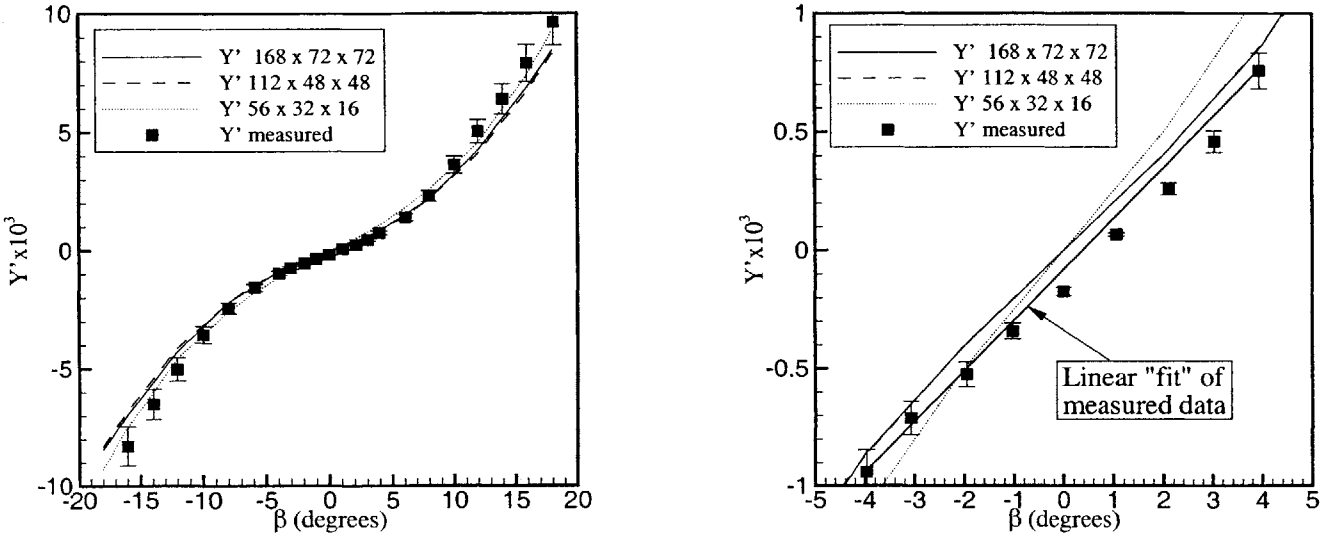

Figure 7-4: Side force vs. angle of attack for SUBOFF with stern appendages.

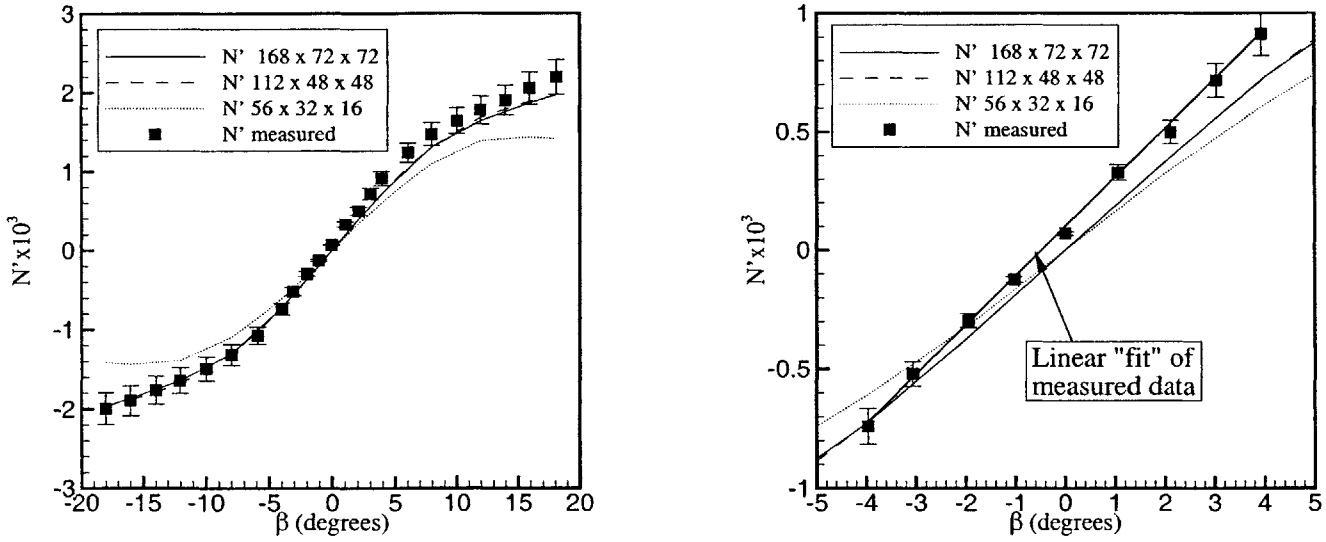

Figure 7-5: Yawing moment vs. angle of attack for SUBOFF with stern appendages.

7.4 Summary

Prior to verifying and validating the new method, the IFLOW code by itself was verified and validated. This effort was successful in establishing the limits of the IFLOW code and in determining the minimum (near optimum) number of grid points that could be used in all configurations in all subsequent calculations.

The successful effort made to verify and validate IFLOW at the beginning of this research showed that it was at least reasonable to expect that a coupled method that included IFLOW could predict the maneuvering characteristics of near-surface submarines. The grid sensitivity study performed here served to guide the grid generation for the coupled calculations. In subsequent chapters all vertical plane maneuvering coefficients are shown. All horizontal plane experimental data can be transformed to vertical plane data as the bodies are studied here are symmetric about both the vertical and horizontal planes, and the experimental data exists for deep water only.

Chapter 8

Coupled Verification and Validation

8.1 Introduction

As with any other computational method, the current method must be verified and validated. According to Roache [20], *verification* is the process of determining if the computational models are the correct implementation of the conceptual models, and if the resulting code can be properly used for an analysis. Verification looks for errors in the programming and implementation of the models. *Validation* is the process of determining the degree to which a model accurately represents the real world. It isn't possible to validate an entire CFD code. Here, as in any other validation attempt the code was validated for a range of applications for which there exists experimental data.

Verification is often described as "solving the equations right", while validation is described as "solving the right equations". In this research the verification that was done involved determining that the solutions satisfied iterative and grid convergence criteria. *Verification* also showed that the calculated free-surface waves generated by the submerged bodies are qualitatively in agreement with theory. *Validation* involved comparing calculated and measured vertical forces and pitching moments.

This chapter is devoted to the validation, verification, performance and limita-

tions of the method developed to predict the maneuvering coefficients of near-surface submarines.

8.2 Iterative Convergence

For any RANS calculation it is necessary to check the convergence history to verify or establish confidence in the solution. This is even more important in the present research since a large number of calculations were performed without the benefit of direct comparison with experimental data to validate the numerical results. In addition, experience had shown that the small domains like the ones used here often yield slower convergence rates and even divergence for RANS calculations. (As explained later this problem was avoided in the present research.)

To improve convergence and reduce CPU time the solution from one condition was used as the initial guess for the solution to the next condition. This technique proved to be quite efficient despite the fact that only a cursory attempt was made to optimize it, i.e. to find the minimum number of RANS multigrid cycles per flow condition.

Given the large number of calculations, it is not practical to show all the convergence histories. Figure 8-1 shows convergence histories for some of the SUBOFF bare hull calculations. This style of plotting convergence history was used to clearly show as many convergence histories as possible in one plot and to illustrate the efficiency gained by using one solution as the initial conditions for the next solution.

A drop of four to five orders of magnitude in the root mean square of the pressure residual[1] is considered adequate convergence for most applications. For this figure Froude number and depth were held constant and the angle of attack was varied from 0° to 18°. The larger spikes in the plot indicate a change in the angle of attack. The smaller (barely visible) spikes in the plot indicate the sudden change in the RANS boundary condition due to the coupling with the panel code. This plot indicates that

[1]The pressure residual is the measure of the maximum change in pressure from one iteration to the next. Therefore, for the purposes of determining if a calculation is converged changes in the calculated pressure are tolerated only in the fourth of fifth significant digit.

perhaps as few as 80 cycles could be used per condition rather than 150.

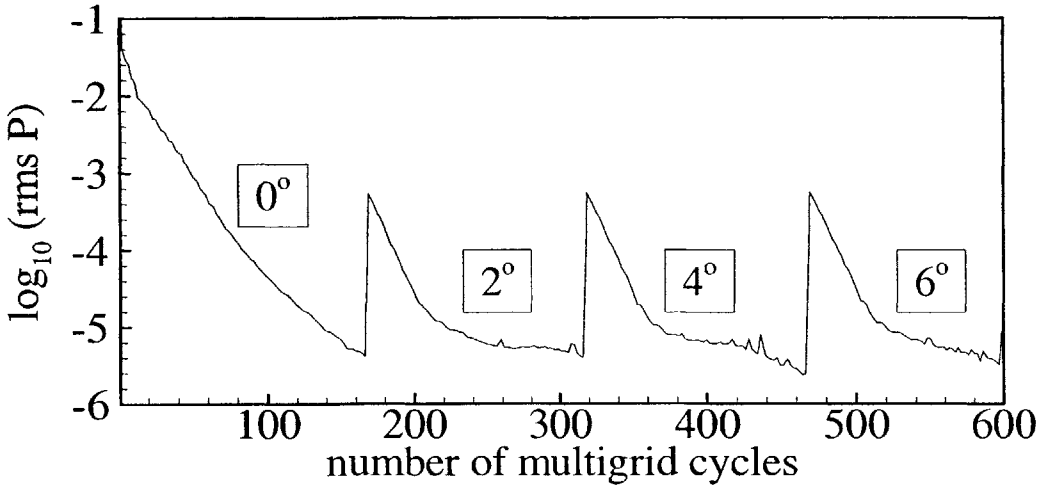

Figure 8-1: Convergence history for the SUBOFF bare hull, α varies from 0° to 6°, $Fr_L = 0.5$, $Z_{CG} = -0.7L$, $Re_L = 14 \times 10^7$, grid: $80 \times 24 \times 48$. Conditions to simulate experimental conditions as in Figure 8-4. The large spikes in the plot result from a change of angle of attack. Z_{CG}/L is the vertical location of the center of gravity.

Figure 8-2 shows the convergence history for the SUBOFF with sail configuration with a grid resolution of $96 \times 24 \times 48$. As the depth was varied from deep to shallow the solution from the previous depth was used as the initial guess for the next depth. More RANS multigrid cycles were used for the initial depth and the final two depths than for the intermediate depths to ensure iterative convergence. This figure was included because it represents one of the more challenging sets of conditions.

8.3 Grid Convergence

A second essential step in establishing confidence in RANS calculations is a grid refinement or grid convergence study. By comparing the solutions produced by successively finer meshes, the possibility that the grid is a source of solution error is minimized. In other words, if two grids of different resolution produce the same answer any error in that answer is more likely due to the numerical method than the grid. Research presented in Chapter 7 showed that the grid resolutions used in the present study

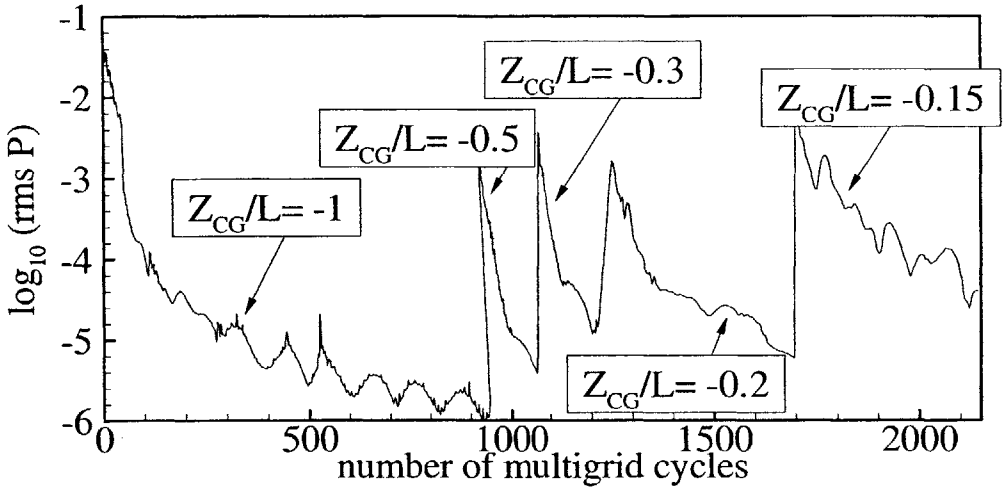

Figure 8-2: Convergence history for the SUBOFF with sail, Z_{CG}/L varies from -1.0 to -0.15, $\alpha = 0$, $Fr_L = 0.1$, $Re_L = 14 \times 10^7$, grid: $96 \times 24 \times 48$. NOTE: the large spikes in the plot result from a change in depth.

yield grid independent force and moment calculations in an "infinite" fluid.

Consistent with those results the plot of vertical force and pitching moment versus angle of attack for the SUBOFF bare hull in Figure 8-3 for three different grids indicates that the solution no longer changes significantly beyond a resolution of $80 \times 24 \times 48$ for the SUBOFF bare hull. Similar results not shown here were obtained for the Albacore bare hull. A grid convergence study for the SUBOFF with sail geometry showed that a grid of 96 x 24 x 48 was adequate.

8.3.1 Validation of the Coupling

The successful coupling of IFLOW with FKX was confirmed by comparison of the forces and moments of the coupled solution with the forces and moments of the uncoupled solution for pitch angles between zero and six degrees.

Z' and M' were calculated for the SUBOFF and Albacore bare hulls with the coupled code and with the RANS code only and are compared in Figures 8-4 and 8-5.

The coupled vertical force and the uncoupled vertical force solutions are nearly identical. The slope of the pitching moment curve with the free-surface is higher than without the free surface and appears to compare less favorably with the measured

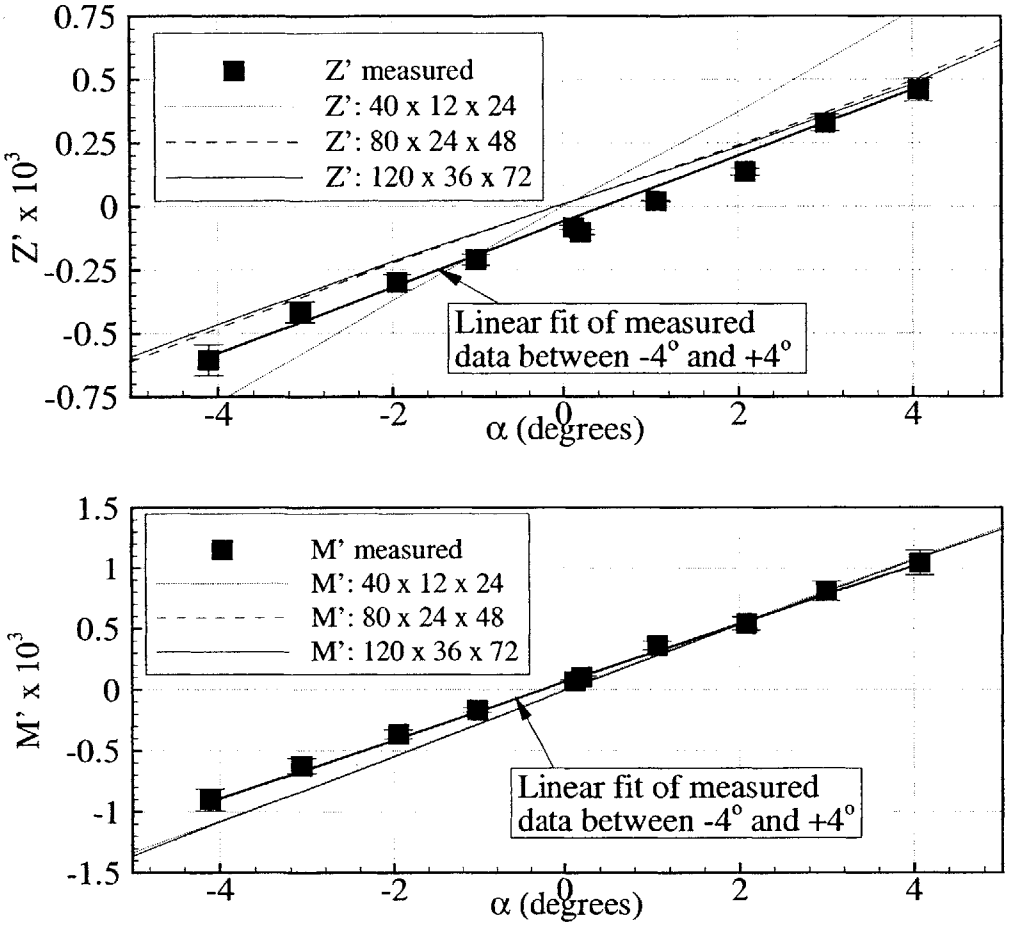

Figure 8-3: Vertical force and pitching moment for SUBOFF bare hull with three grid resolutions. $Re_L = 14 \times 10^7$, $Z_{CG}/L = -0.7$, $Fr_L = 0.1$.

data. It should be noted that the experimental data is not symmetric about the origin. This is probably due to the use of struts to support the model on the towing carriage. These struts may play a larger role in influencing the pitching moment than the vertical force especially when the body is pitched downward. If this is true than the pitching moment from the coupled solution may in fact be more accurate than the uncoupled solution since it more nearly matches the measured data at positive pitch angles. This will be the subject of further investigation.

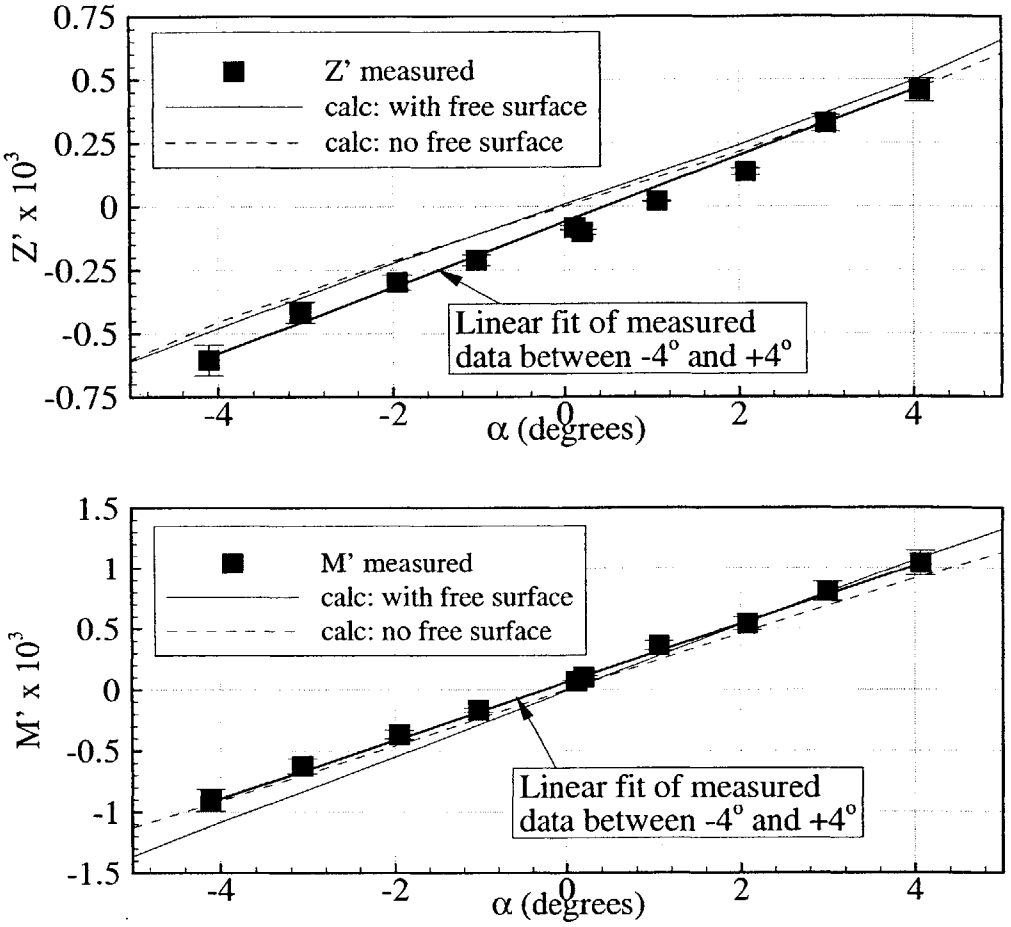

Figure 8-4: Vertical force and pitching moment for SUBOFF bare hull with and without the effects of the free-surface. $Re_L = 14 \times 10^7$, $80 \times 24 \times 48$. Conditions with free-surface are $Z_{CG}/L = -0.7$, $Fr_L = 0.5$.

8.4 Performance

In addition to verification and validation, it is perhaps equally important to measure and discuss the performance of a new method. The intention of the present research was to develop a technique that could be used to develop a large database of maneuvering coefficients, thereby, making it useful to the engineer designing submerged vehicles. To achieve this goal it was essential to develop a very efficient method that required little human interaction and little CPU time.

Typically, one set of SUBOFF bare hull flow conditions could be simulated using an $80 \times 24 \times 48$ grid in 200 RANS multigrid cycles with 5 panel code couplings and

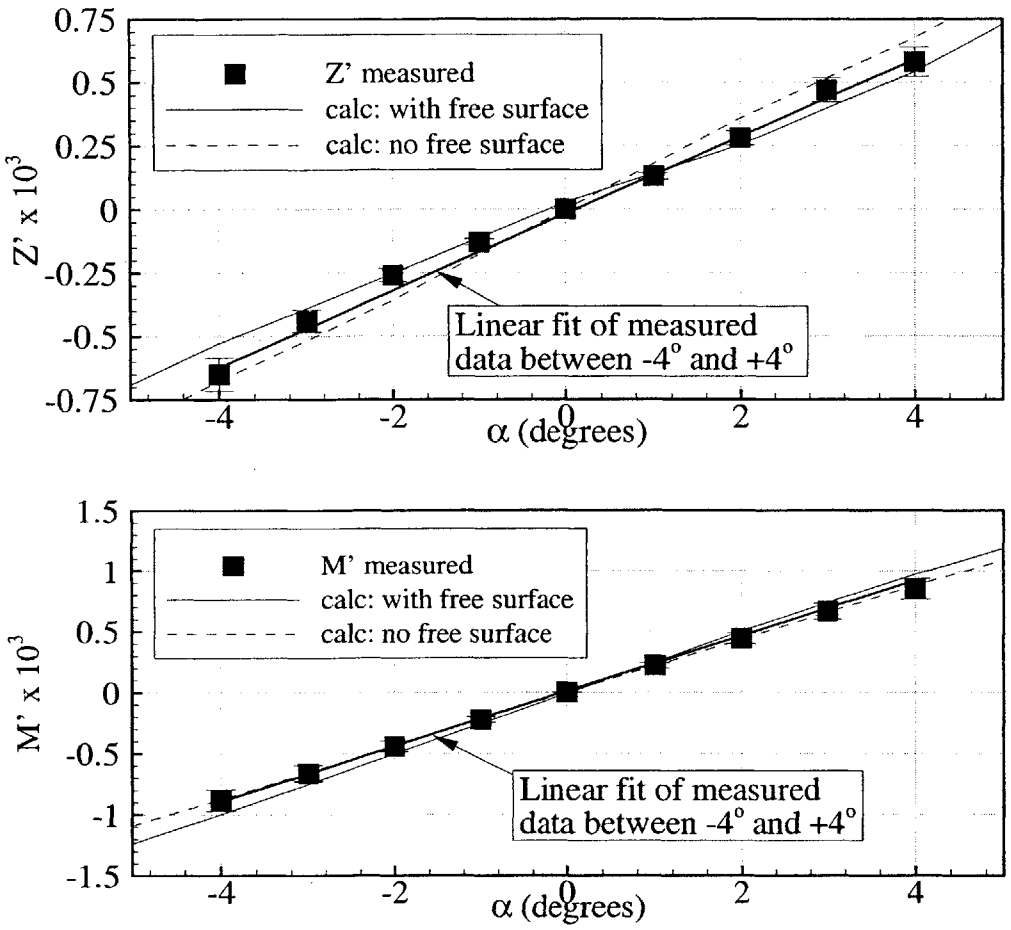

Figure 8-5: Vertical force and pitching moment for Albacore bare hull with and without the effects of the free-surface. $Re_L = 14 \times 10^7$, $80 \times 24 \times 48$. Conditions with free-surface are $Z_{CG}/L = -0.7$, $Fr_L = 0.5$.

a total CPU time of 82 minutes on a single processor Cray J90. Approximately, 82% of the CPU time was used by the RANS code and 18% was used by the panel code. The single processor Cray J90 is approximately as fast as a 1 Ghz Pentium.

These performance characteristics were very similar for all geometries and conditions considered. As a result a wide range of conditions were considered and a correspondingly large database of maneuvering characteristics was created.

8.5 Limitations of Method

An effort was made to determine the range of applications for which the method can be applied. A number of parameters were varied in the current research. The limits on those variations are discussed below. In most cases the limit of variation was determined by the iterative convergence history.

8.5.1 Geometry

No geometric limitations were discovered in the current research, i.e. computations were successful for all geometries considered. This is not a claim that the current method can deal with any geometry, but there is no known submarine-like geometry that could not analyzed with the current method subject to the following limitations.

8.5.2 Domain Size

Because neither the bodies nor the grids were allowed to penetrate the free-surface the size of the domain above the submarine decreased as the depth of submergence decreased. Small domains are well known to cause iterative convergence difficulties. A cursory study of the convergence history versus domain size showed almost no relationship, however.

It is believed that this is due to the method itself. The FKX code computes the flow field at the outer boundary of the IFLOW domain where the flow is considered to be inviscid. It is well known that panel codes such as FKX are quite accurate where the flow is considered to be inviscid. Therefore, the boundary condition used by IFLOW in the current method is quite accurate. As a result instabilities inherent in small-domain RANS only methods are completely avoided here.

8.5.3 Depth

The depth of submergence was limited in the sense that neither the grid or the body itself was not allowed to penetrate the free-surface. This is an important limitation

and eliminates some very interesting flow conditions. The complexity of such flows, however, made it impractical to include in the present research.

The iterative convergence of the solution tended to deteriorate slightly as the body approached the free-surface. Some not inconsiderable care was given to grids generated for centerline depths of $Z/L < 0.25$ to insure good iterative convergence.

In addition, as the depth of submergence was decreased the solution from the previous depth was used as the initial guess for the solution at the shallower depth. This improved iterative convergence as well.

8.5.4 Speed

Since the lengths of the bodies were fixed, varying the Froude number varied the speed of the vehicles. In the present research Froude numbers were varied between 0.1 and 1.0. It is believed that this will account for most of the speeds at which submarines operate near the free-surface.

Iterative convergence did not appear to be correlated with the speed of the submerged vehicle, i.e. convergence did not suffer with either increasing or decreasing speed.

8.5.5 Angle of Attack

There are two reasons why angle of attack can be limited in the current method:

1. negative cell volumes

2. grid or body penetration of the free-surface

As mentioned in earlier chapters, to simulate an angle of attack the body itself must be rotated to that angle of attack. This led to some initial difficulties in generating grids with no negative cell volumes. However, careful coding of the numerical grid generation computer program virtually eliminated negative cell volumes as a limiting factor. As long as the domain was big enough the submarines could be rotated to angles of attack as high as $\pm 18^\circ$ without introducing negative cell volumes.

There is no way to prevent the grid or body from penetrating the free-surface at shallow depths and high angles of attack. Therefore, future effort must be made to improve the method to allow the body to penetrate the free-surface.

The current limitations on the angle of attack of the body near the free-surface are likely to *not* limit the usefulness of the method as submarines do not usually operate at high angles of attack near the free-surface.

8.6 Summary

Despite the availability of a relatively large amount of experimental data by the normal standards of computational fluid dynamics calculations, the range of applications presented here far outstripped the range of validation. It is important to recognize, however, that the code was *verified* for the entire range of applications. The obvious conlcusion is that more experimental data is needed to more completely validate the method. Of course, collecting this data is expensive and time-consuming. In the mean time, the current method can be used to illustrate interesting or potentially problematic characteristics in the design of submarines.

Chapter 9

Maneuvering Characteristics of Near-Surface Submarines

9.1 Introduction

After the time-consuming but necessary verification and validation effort was completed, attention was turned to predicting maneuvering coefficients across a wide range of conditions. A great deal of effort was made in the present research to develop a database of maneuvering coefficients that could used by submarine designers to guide their work. Figures within this chapter illustrate much of this database.

To accomplish this goal several thousand unique, three-dimensional computations were completed. Parameters such as speed, depth, angle of attack and geometry were systematically varied to create the most comprehensive computational database of maneuvering coefficents available today.

The results of this research are presented here.

9.2 Processing the Results

In the present research depth, Froude number, angle of attack, geometry and grid resolution were varied producing several thousand unique combinations and thus several thousand unique three-dimensional computations. IFLOW, FKX, GRID and the

coupling method proved to be very robust and computationally efficient. Without a robust and efficient method the creation of this database would not have been accomplished.

Due to the great number of computations performed, it was necessary to develop a data management system to perform and track the computations. This system helped to minimize the necessity for human interaction, which in turn minimized the introduction of human error. The data management system consisted of a series of UNIX shell scripts that could be easily ported from the Cray environment to any other UNIX environment.

Shell scripts are simply text files made up of commands much like a computer program. Upon execution of a shell script the operating system interprets each command and carries it out. In other words, shell scripts are not compiled. Shell scripts allow many of the same functions found in conventional programming languages like C and Fortran such as variables, loops, and conditionals. It was through these loops and conditional statements that the parameter studies were carried out, where the variables were the parameters.

There are three main steps to these analyses: 1) pre-processing of the input data, which includes grid generation, 2) analysis of the flow field, 3) post-processing of the output data, including the calculation of forces and moments on the bodies. The shell script was used to manage and automate to the greatest extent each of the three steps. It is safe to say that most of the results presented in this thesis would not appear there if shell scripts had not been used.

A great advantage of using shell scripts rather than performing modifications to the coupled computer codes is that future releases of the GRID, IFLOW and FKX codes can be easily interchanged with the versions used in this research. Additional parametric studies can also be accomplished by modifying the current scripts without modifying the underlying software. In general, it is easier to modify and maintain shell scripts, which are interpreted rather than compiled, than it is to maintain compiled computer code.

The results of the parametric studies performed for this research are presented in

the following sections.

9.3 Forces and Moments

9.3.1 Description of Computations

The experimental force and moment measurements available for comparison were not made with the intention of including the effects of the free-surface. However, since they are the only publicly available force and moment data for submarine-like bodies these measurements are the logical starting point for the validation of the present method. Indeed, the first step in validating the coupling of the RANS and panel codes should be to verify that the coupling has done "no harm", i.e. that the coupled method yields the same results as the RANS only method when the free-surface effects are expected to be negligible.

The experimental measurements were made in the towing tank at the David Taylor Model Basin in Maryland by Roddy [21] (SUBOFF) and Dempsey [7] (Albacore). The models were towed at a depth of about $Z_{CG}/L = 0.7$ with $Re_L = 14x10^7$ and $Fr_L \approx 0.5$, where Z_{CG}/L is the vertical location of the center of gravity of the body. A positive angle of attack was accomplished by inclining the bow upward toward the free-surface. A positive vertical force is defined as upward toward the free-surface and a positive pitching moment is defined as a moment that causes the vehicle to pitch up.

There is no experimental data available with which to directly compare the results presented in this section. However, the attention given to validation of the RANS code and to the verification and indirect validation of the coupled codes it is believed that the results presented in this chapter are at least reasonable. As stated earlier relationships between the vertical force/pitching moment and depth/Froude number have been established. These relationships are shown in Figures 9-1 - 9-5.

Seven Froude numbers and 6 depths are represented in each of the figures. The vertical force and pitching moment are shown for the SUBOFF bare hull in Figure 9-1,

the Albacore bare hull in Figure 9-2, the SUBOFF with sail in Figure 9-3, the SUBOFF with stern appendages in Figure 9-4 and the Albacore with stern appendages in Figure 9-5.

9.3.2 Effect of Speed and Depth

Clearly, the vertical force and pitching moment are depth and speed dependent for all of the geometries investigated here. In fact, these relationships are quite complex. For Froude numbers less than about 0.3, Z' and M' do not change significantly as the depth changes. However, as speed increases at shallow depths Z' increases to larger positive values as Froude number approaches 0.4. As the speed continues to increase the vertical force decreases to *negative* values.

The free-surface wave patterns in Figures 9-10 thru 9-12 aid in the understanding of the effect speed has on vertical force and pitching moment. These figures show the free-surface disturbance at a fixed depth of $Z_{CG}/L = -0.2$ for various speeds for the SUBOFF bare hull, the SUBOFF with sail and the Albacore with stern appendages, respectively.

The initial observation to make is that the wave patterns change dramatically as speed changes. Both the amplitude and the wavelength increase with speed. It is, therefore, not surprising that the vertical force and pitching moment vary sharply with speed.

In addition, it is well known that the amplitude of the waves produced by the submerged bodies increases as depth decreases.

Another interaction takes place here. The free-surface tends to have a "lifting effect" on the body. As the body approaches the free-surface the volume of fluid between the body and the free-surface decreases, and therefore the speed of the fluid above the body tends to be higher than the speed of the fluid below the body. This induces a lift force on the body in the upward or positive direction. It is these changes in amplitude and wavelength that drive the complexity of these relationships.

The following discussion serves to further illustrate the source of this complexity for the SUBOFF bare hull geometry. It can, however, be applied to the other

geometries considered here as all wave patterns and all force and moment maps are somewhat similar.

From Figure 9-1 it can be seen that at a depth of $Z_{CG}/L = -0.2$ the vertical force goes from small positive values (upward direction) to large positive values and then to negative values as speed increases. This curious behaviour can be better understood if one observes the free-surface wave patterns in Figure 9-10 created by the body as its speed increases.

Throughout all speeds the body will tend to have a positive vertical force due to the above mentioned "lifting effect". If the free-surface were fixed then the submarine would experience a positive vertical force for all speeds. The discussion below will explain why the positive vertical force increases sharply at $Fr_L = 0.4$ and then decreases to negative or downward values for $Fr_L > 0.65$.

It is useful to consider the peaks and troughs of the waves generated at the free-surface. If a peak is directly over the submerged body that fluid will tend to push the body downward and the body will experience a negative vertical force due to the peak. If a trough is directly over the body the body will experience a positive or upward vertical force due to the trough.

The pressure on the hull due to the surface wave that contributes to the vertical force acts in the body-normal direction. If a peak or trough is located above a section of the hull (like the bow or stern) that has curvature in the x-z plane, then the peak or trough effects both the vertical and longitidunal forces acting on the body, i.e. it does not act solely in the vertical direction.

At $Fr_L = 0.25$ the wave pattern above the body is mostly symmetrical fore and aft. Therefore, the effect of the peaks and troughs on the vertical force largely cancel each other. At $Fr_L = 0.4$ the peak of the wave resides directly over the bow of the submarine, while the trough is spread over the aft two-thirds of the submarine. The bow of the submarine has the highest curvature in the x-z plane. Therefore, the vertical (downward) force on the body due to the peak is not as great as the vertical (upward) force on the body due to the trough, which resides directly over the parallel middle body of the submarine. This is the source of the large increase in upward

vertical force seen at $Fr_L = 0.4$ in

For $Fr_L > 0.7$ there is only a peak over the body and no trough. This downward vertical force due to this peak overcomes the lifting effect of the free-surface to cause the submarine to experience a net downward vertical force as seen in Figure 9-1.

Similar reasoning can be applied to the other geometries studied here to explain the effect of speed on the vertical force and pitching moment of near surface submarines.

9.3.3 Effect of Downstream Boundary

To determine the sensitivity of the solutions to the location of the donwstream boundary a parameter study was performed on the Albacore with stern appendages with the downstream boundary located at 1.5 body lengths downstream of the stern in addition to the already computed parameter study with the downstream boundary located at three body lengths downstream of the stern.

Figures 9-6 through 9-9 compare the vertical force and pitching moment versus speed and depth for the Albacore with stern appendages computed in the two domains.

Figure 9-6 shows the vertical force with the downstream boundary set at three body lengths downstream of the stern. Figure 9-7 shows the vertical force with the downstream boundary set at 1.5 body lengths downstream of the stern.

Figure 9-8 shows the pitching moment with the downstream boundary set at three body lengths downstream of the stern. Figure 9-9 shows the pitching moment with the downstream boundary set at 1.5 body lengths downstream of the stern.

Only very small differences are noted in the solutions for the two domains. This indicates that the location of the boundary at 3 body lengths downstream of the stern is adequate.

9.3.4 Effect of Geometry

Figures 9-1 - 9-5 also indicate the important role geometry plays in vehicle performance near the free-surface. While the trends seen in Figures 9-1 - 9-5 for the five geometries are similar, the magnitude of the vertical force changes significantly from geometry to geometry.

Figures 9-1,9-3 and 9-4 show the forces and moments for the three SUBOFF configurations. Figures 9-2 and 9-5 show the forces and moments for the two Albacore configurations. Obviously, the appendages play a significant role in the behaviour of the submarines near the free-surface. In general, the appendages tend to increase the magnitude of the forces and moments on the bodies at all speeds and depths.

In addition the hull shape tends to have a significant impact on the performance of the submarines. The Albacore bare hull experiences much higher downward forces than the SUBOFF bare hull. The SUBOFF bare hull appears to interact with the free-surface at greater depths than the Albacore bare hull.

As before it is helpful to look at the free-surface wave elevations generated by the three bodies in Figures 9-13 and 9-14 to understand why this is so.

Figure 9-13 shows the free-surface disturbances produced by the five geometries at $Z_{CG}/L = -0.2$ and $Fr_L = 0.4$. Figure 9-14 shows the free-surface disturbances produced by the five geometries at $Z_{CG}/L = -0.175$ and $Fr_L = 0.7$. In both Figures $\alpha = 0°$ and $Re_L = 14 \times 10^7$. The grid resolutions for the five geometries are: bare hulls - $80 \times 24 \times 48$; SUBOFF with sail - $96 \times 24 \times 48$; and bare hulls with stern appendages - $112 \times 48 \times 48$.

The following discussion serves to explain the dependence of forces and moments on hull shape by comparing the free-surface disturbances produced by the two bare hull configurations.

For the Albacore bare hull the first peak is focused on a part of the hull with a small cross section, while the first trough is spread out over about the remaining 2/3 of the hull. In addition the peak is over a relatively highly curved section of the hull decreasing its effect on the vertical force, whereas the trough is over a flatter section

of the hull increasing its effect on the vertical force. This causes the dramatic rise in upward vertical force seen in Figure 9-1 near $Fr_L = 0.4$

The SUBOFF bare hull shows a similar trend. However, the peak of the free-surface wave is over a flatter section of the hull which increases its impact on the vertical force and negates most of the upward vertical force generated by the trough. Thus the maximum magnitude of the upward vertical force is smaller for the SUBOFF bare hull than for the Albacore bare hull.

Another interesting result of these calculations is the change in sign of the vertical force and pitching moment with increasing Froude number for all five geometries. Only the vertical force will be discussed in detail here, but a similar analysis can be applied to the pitching moment. At low Froude numbers $Fr_L < 0.5$ the vertical force is positive which tends to pull the bodies toward the free-surface. At $Fr_L > 0.5$ the vertical force is negative which tends to push the bodies away from the free-surface. Again this can be understood by considering the free-surface waves produced each body. Figure 9-12 shows the free-surface waves generated by the SUBOFF body at $Fr_L = 0.65, 0.8$ and 1.0. In this figure the body is covered by nearly all of the wave peak. This peak tends to push the body away from the free-surface. Similar results were found for the Albacore and SUBOFF with sail bodies but are not shown for brevity.

Much the same analysis can be applied to understand the pitching moment the bodies experience. The distribution of the free-surface peaks and troughs changes the magnitude and the sign of the pitching moment.

Figures 9-1 - 9-5 also show clearly that the appendages have a significant effect on the amplitude of the free-surface waves. This effect translates into higher magnitudes of forces and moments

9.4 Maneuvering Coefficients

By varying the angle of attack of each of the geometries for all of the conditions considered it was possible to compute the vertical plane maneuvering coefficients.

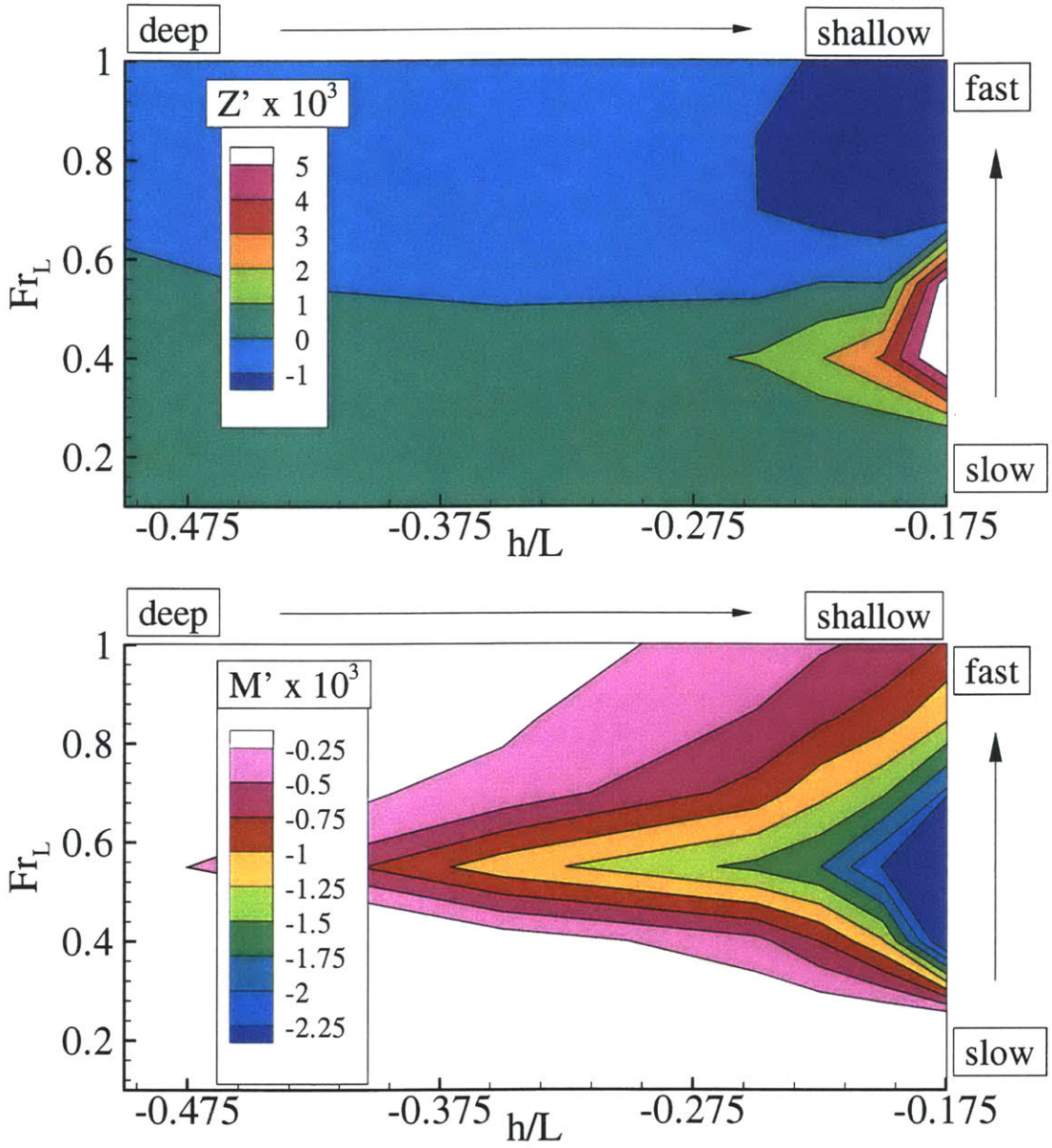

Figure 9-1: Vertical force and pitching moment for SUBOFF bare hull as a function of depth and Froude number. ($80 \times 24 \times 48$).

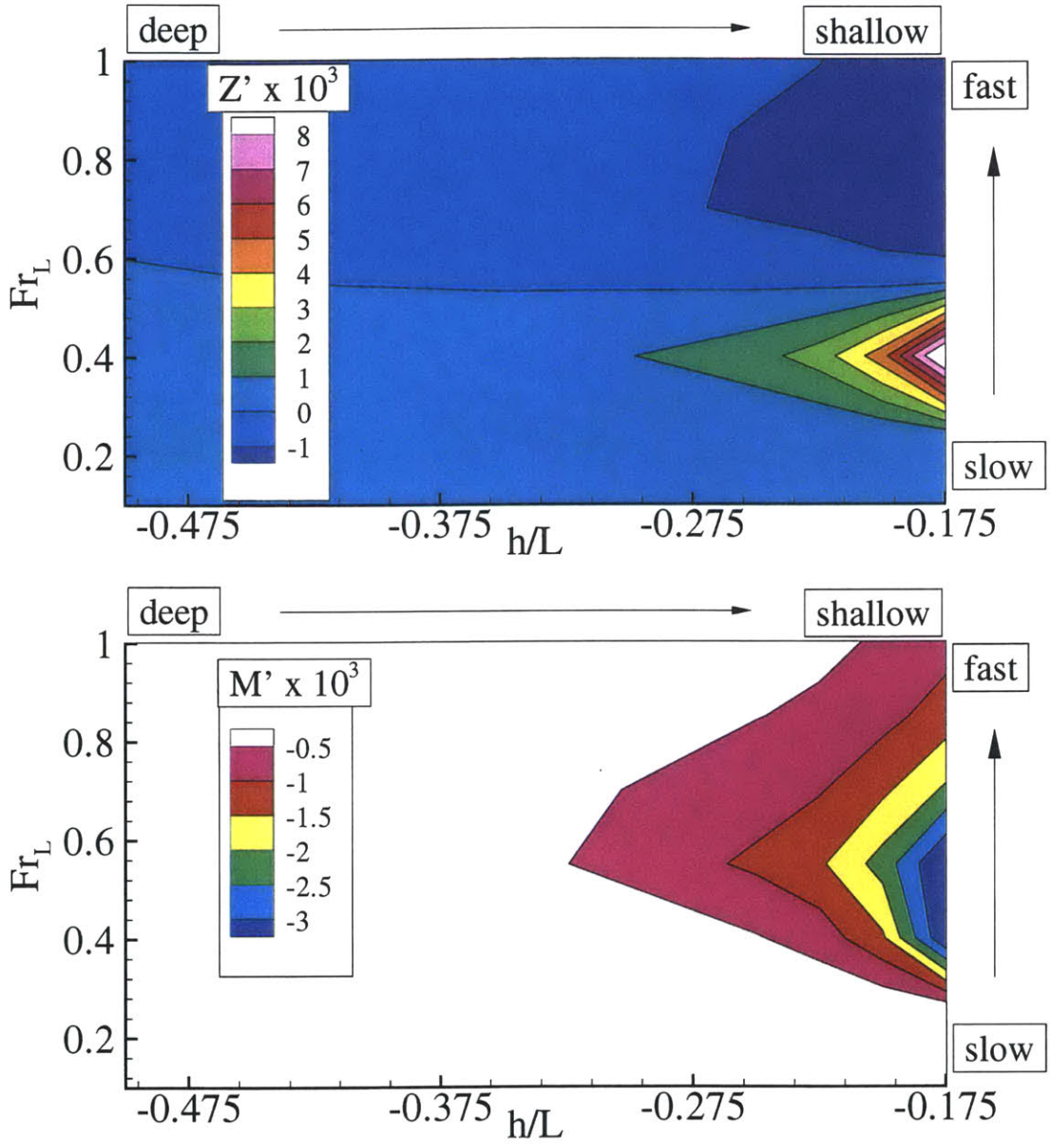

Figure 9-2: Vertical force and pitching moment for Albacore bare hull as a function of depth and Froude number. ($80 \times 24 \times 48$).

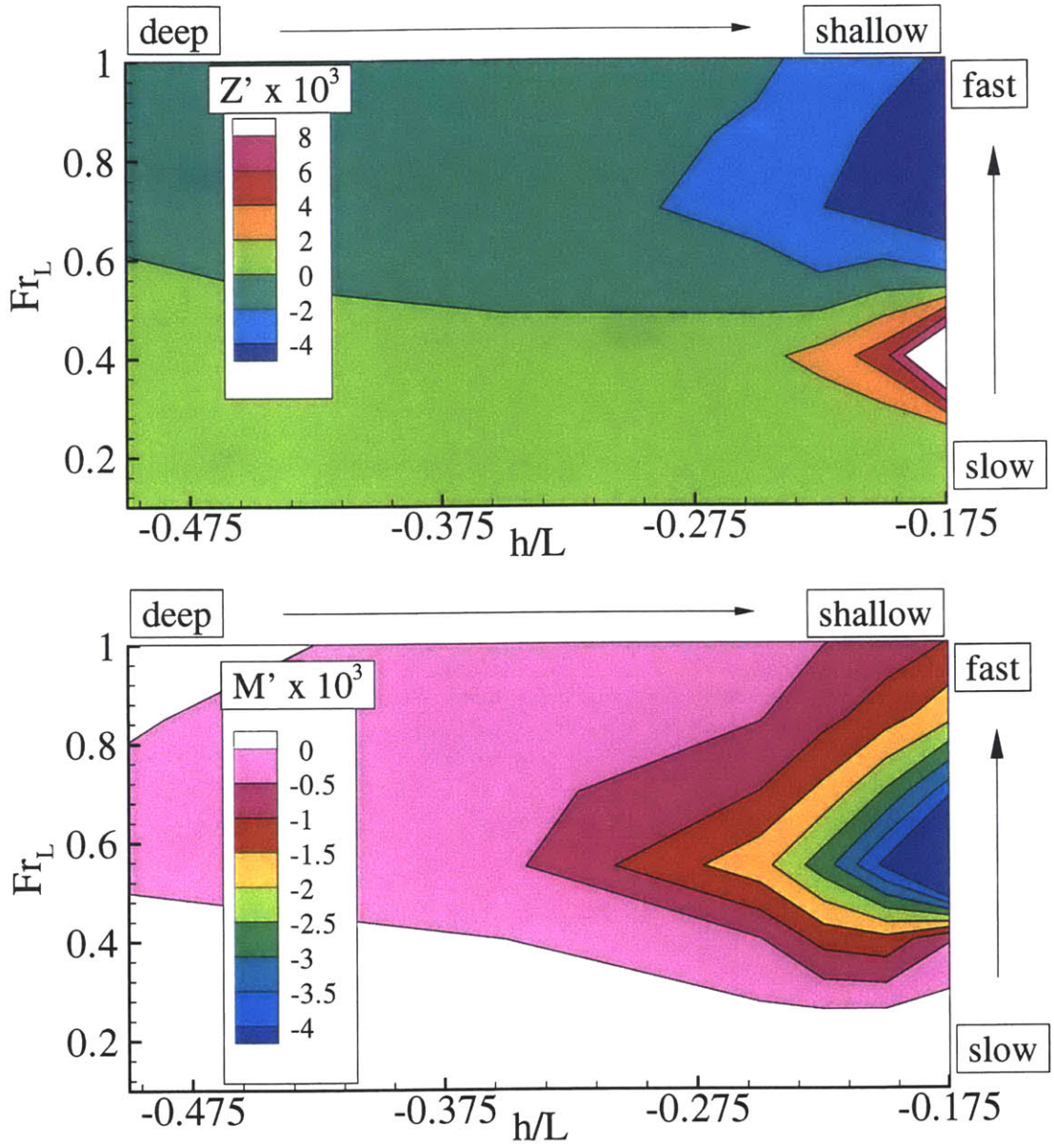

Figure 9-3: Vertical force and pitching moment for SUBOFF with sail as a function of depth and Froude number. ($96 \times 24 \times 48$).

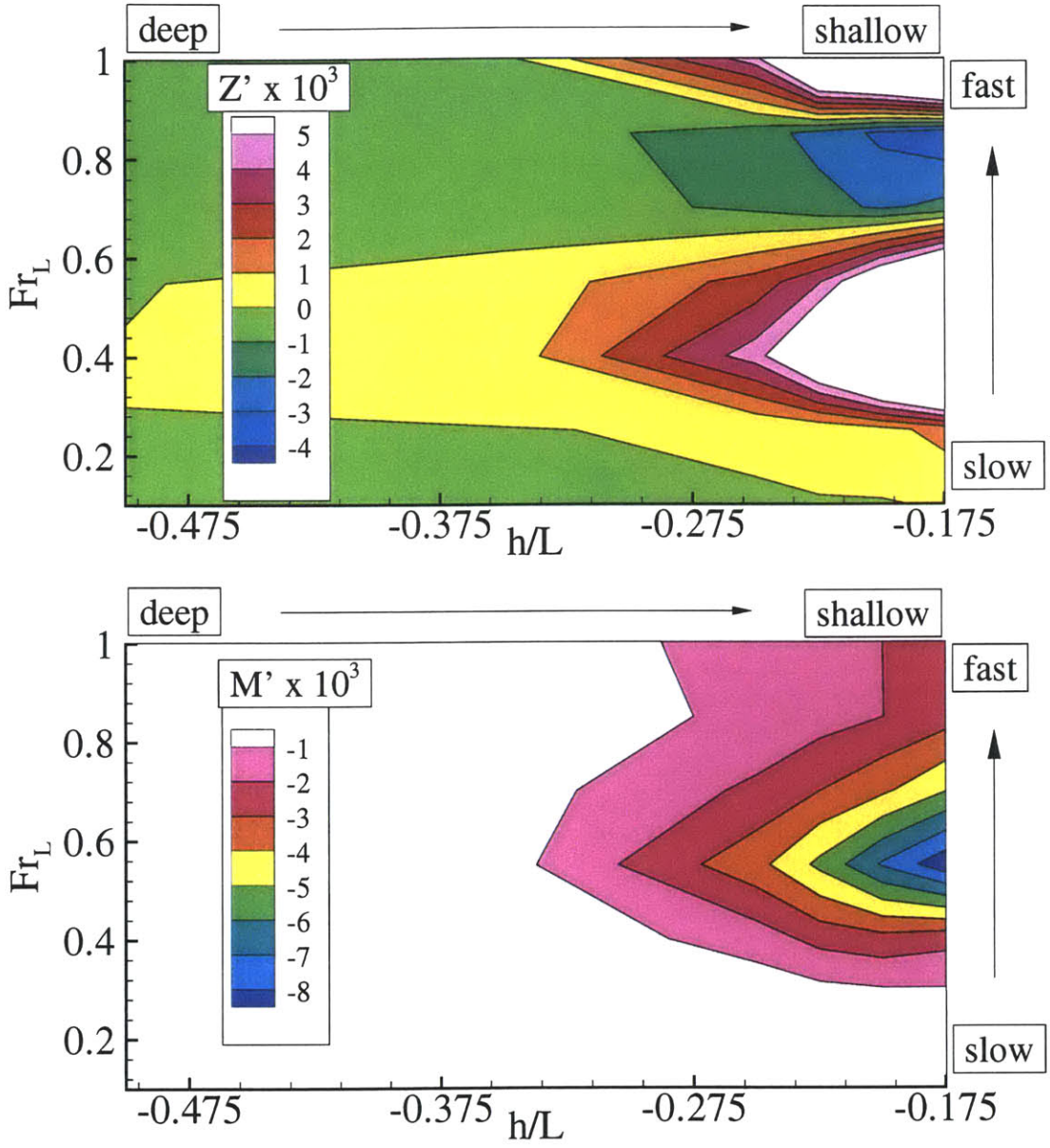

Figure 9-4: Vertical force and pitching moment for SUBOFF with stern appendages as a function of depth and Froude number. ($112 \times 48 \times 48$).

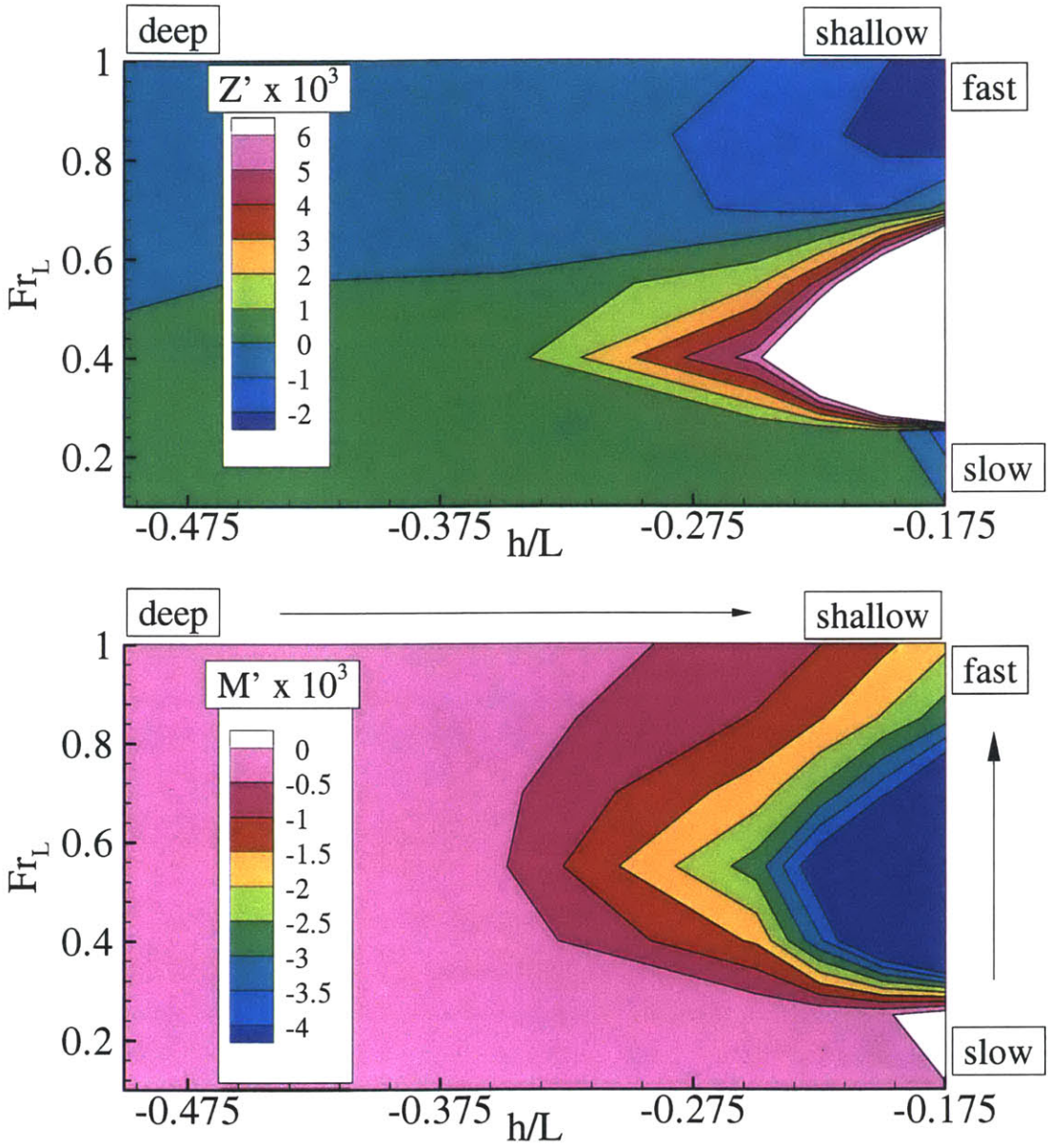

Figure 9-5: Vertical force and pitching moment for SUBOFF with stern appendages as a function of depth and Froude number. ($112 \times 48 \times 48$).

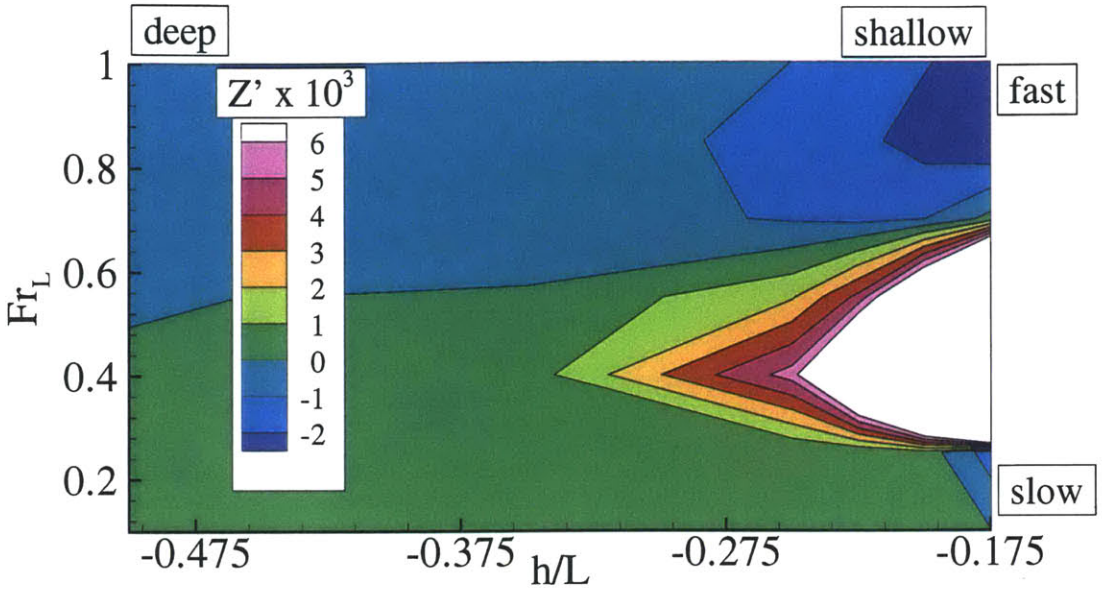

Figure 9-6: Vertical force for Albacore with stern appendages as a function of depth and Froude number. Downstream boundary 3 body lengths from stern. (112×48×48).

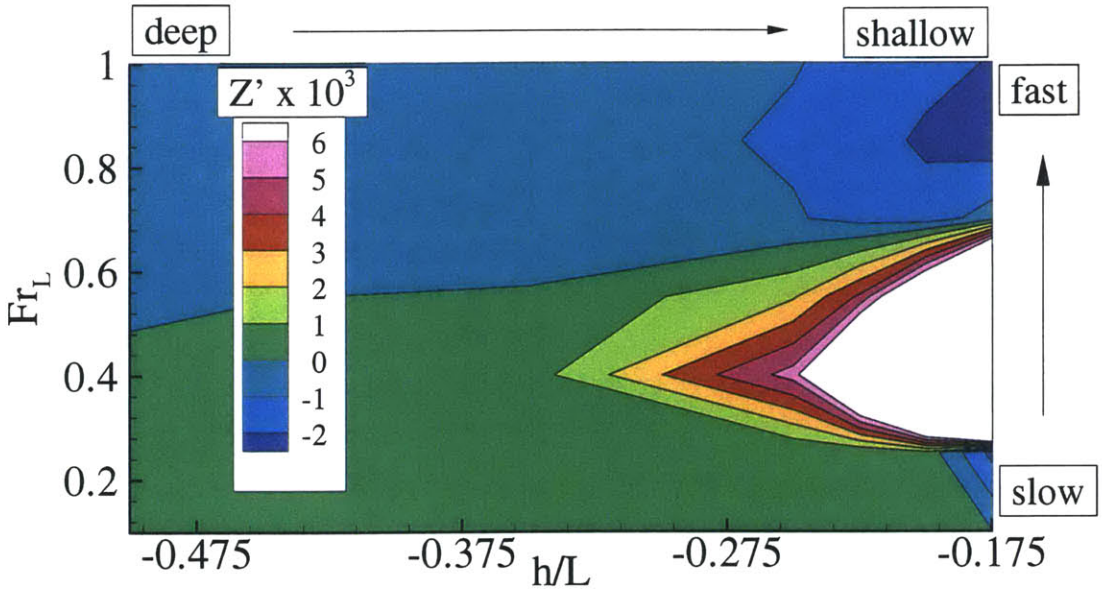

Figure 9-7: Vertical force for Albacore with stern appendages as a function of depth and Froude number. Downstream boundary 1.5 body lengths from stern. ($112 \times 48 \times 48$).

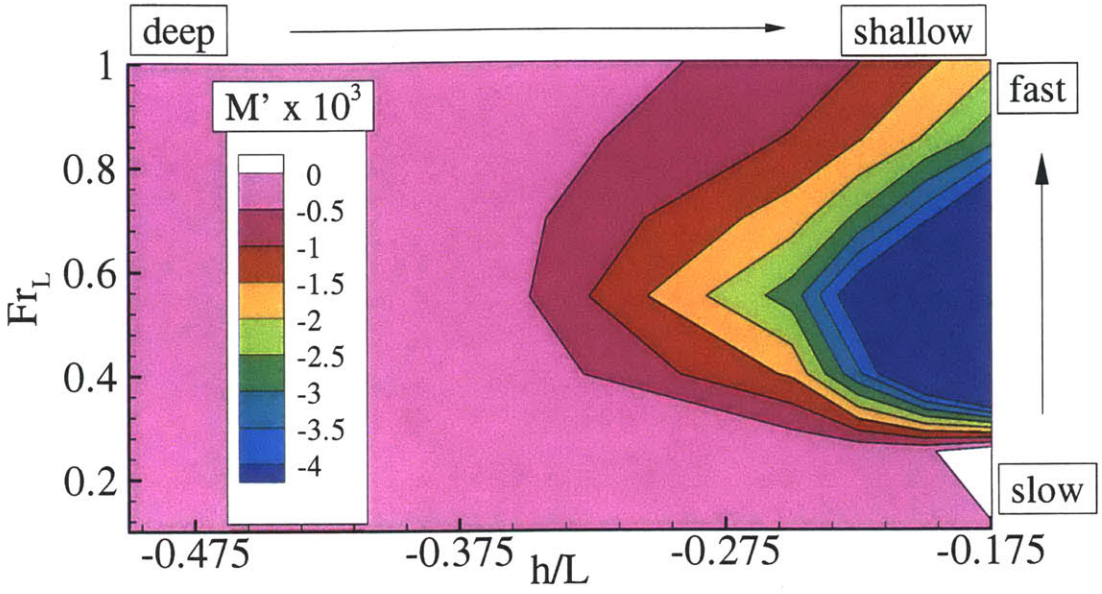

Figure 9-8: Pitching moment for Albacore with stern appendages as a function of depth and Froude number. Downstream boundary 3 body lengths from stern. ($112 \times 48 \times 48$).

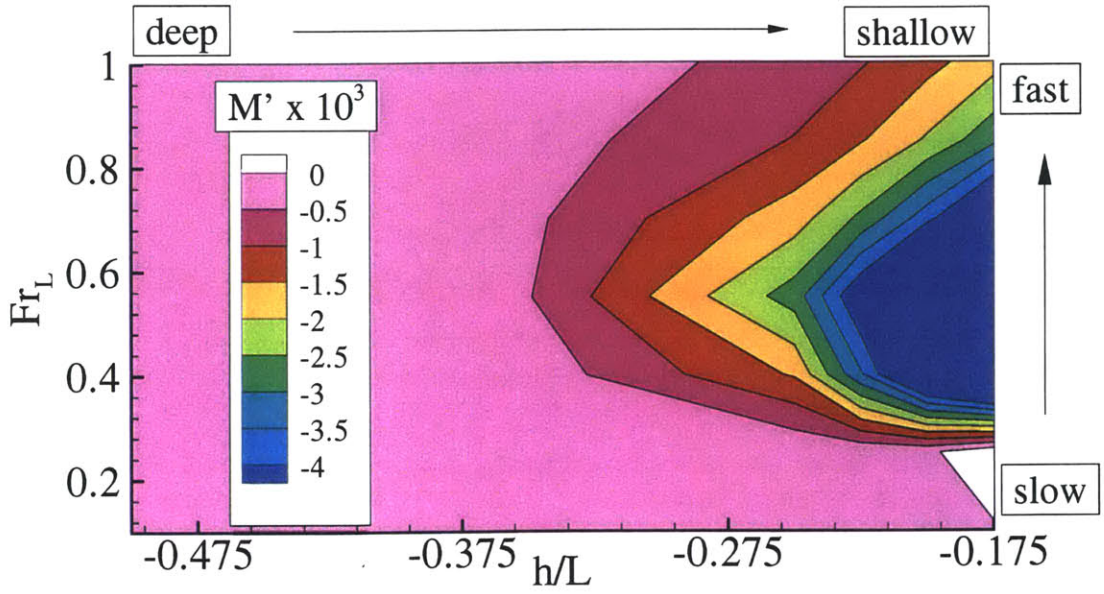

Figure 9-9: Pitching moment for Albacore with stern appendages as a function of depth and Froude number. Downstream boundary 1.5 body lengths from stern. ($112 \times 48 \times 48$).

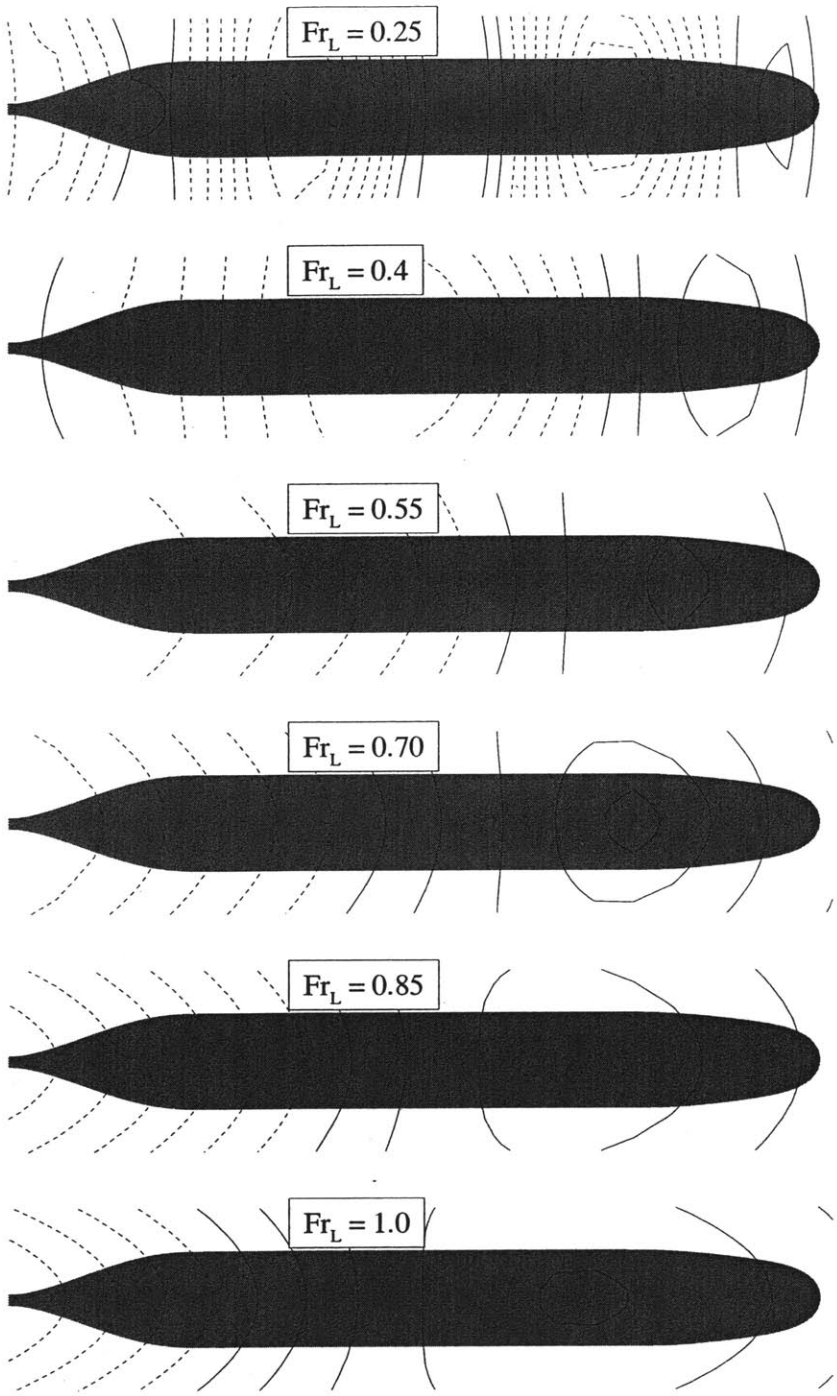

Figure 9-10: SUBOFF bare hull free-surface wave elevations at various Froude numbers. $Z_{CG}/L = -0.2$, $\alpha = 0°$, $Re_L = 14 \times 10^7$, $80 \times 24 \times 48$. The same elevations are plotted for each speed. Negative elevations (troughs) are indicated by dashed contours. This figure serves to illustrate why the vertical force and pitching moment change with respect to Froude number at shallow depths. Not only do the wave elevations change, but the peaks and troughs of the free-surface waves move relative to the body.

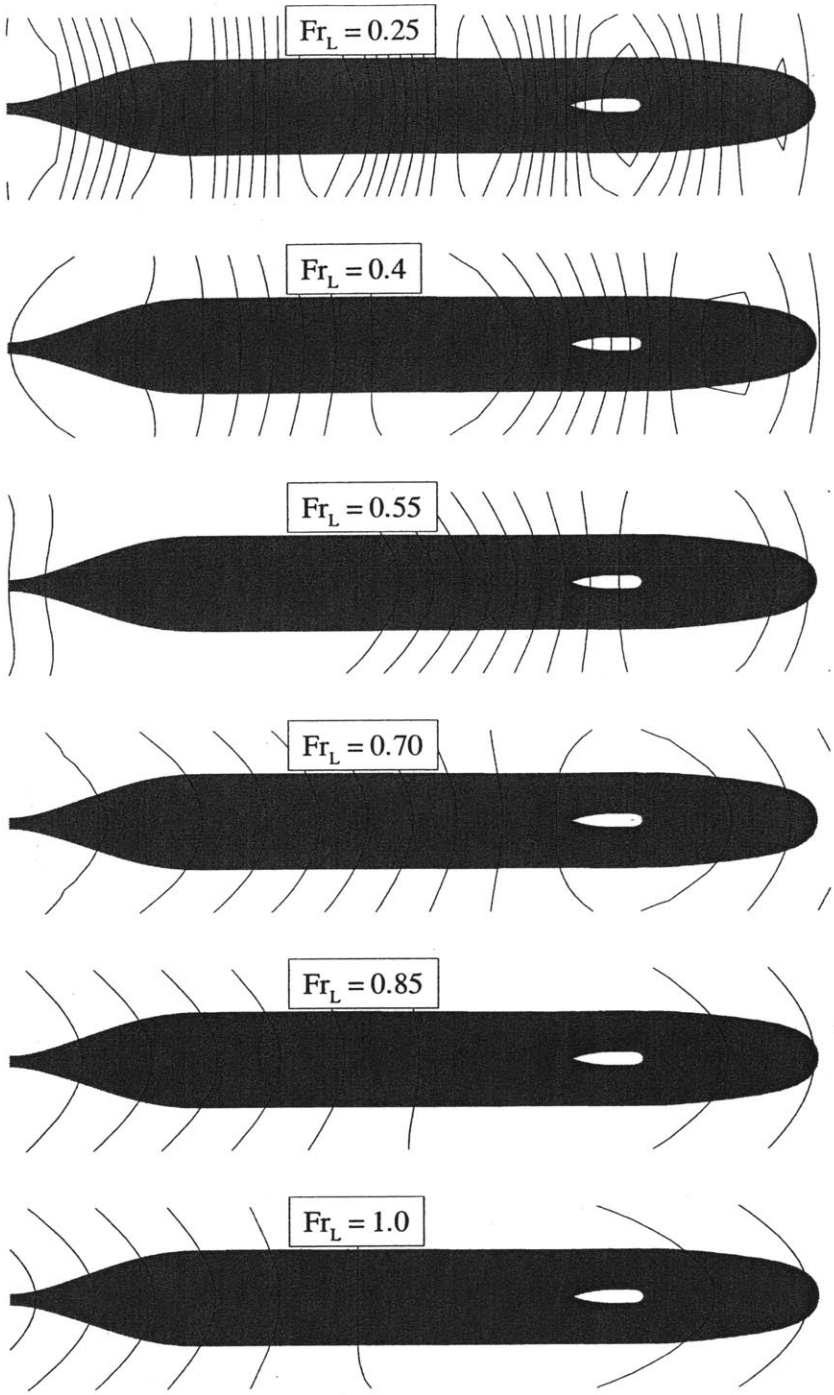

Figure 9-11: SUBOFF with sail free-surface wave elevations at various Froude numbers. $Z_{CG}/L = -0.2$, $\alpha = 0°$, $Re_L = 14 \times 10^7$, $96 \times 24 \times 48$. The same elevations are plotted for each speed. Negative elevations (troughs) are indicated by dashed contours. This figure serves to illustrate why the vertical force and pitching moment change with respect to Froude number at shallow depths. Not only do the wave elevations change, but the peaks and troughs of the free-surface waves move relative to the body.

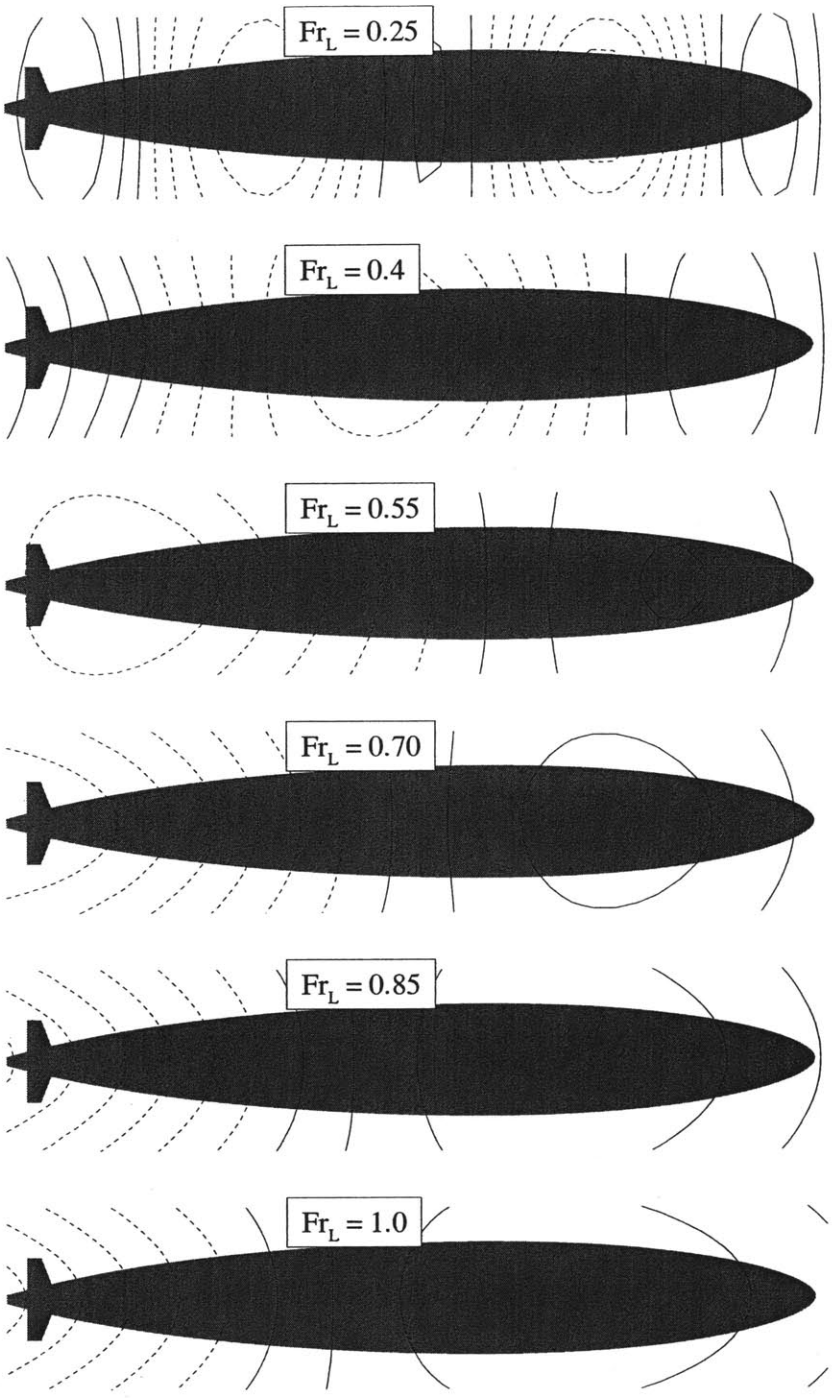

Figure 9-12: Albacore with stern appendages free-surface wave elevations at various Froude numbers. $Z_{CG}/L = -0.2$, $\alpha = 0°$, $Re_L = 14 \times 10^7$, $112 \times 48 \times 48$. The same elevations are plotted for each speed. Negative elevations (troughs) are indicated by dashed contours. This figure serves to illustrate why the vertical force and pitching moment change with respect to Froude number at shallow depths. Not only do the wave elevations change, but the peaks and troughs of the free-surface waves move relative to the body. The influence of the stern appendages on the free-surface disturbance also appears to be a function of speed.

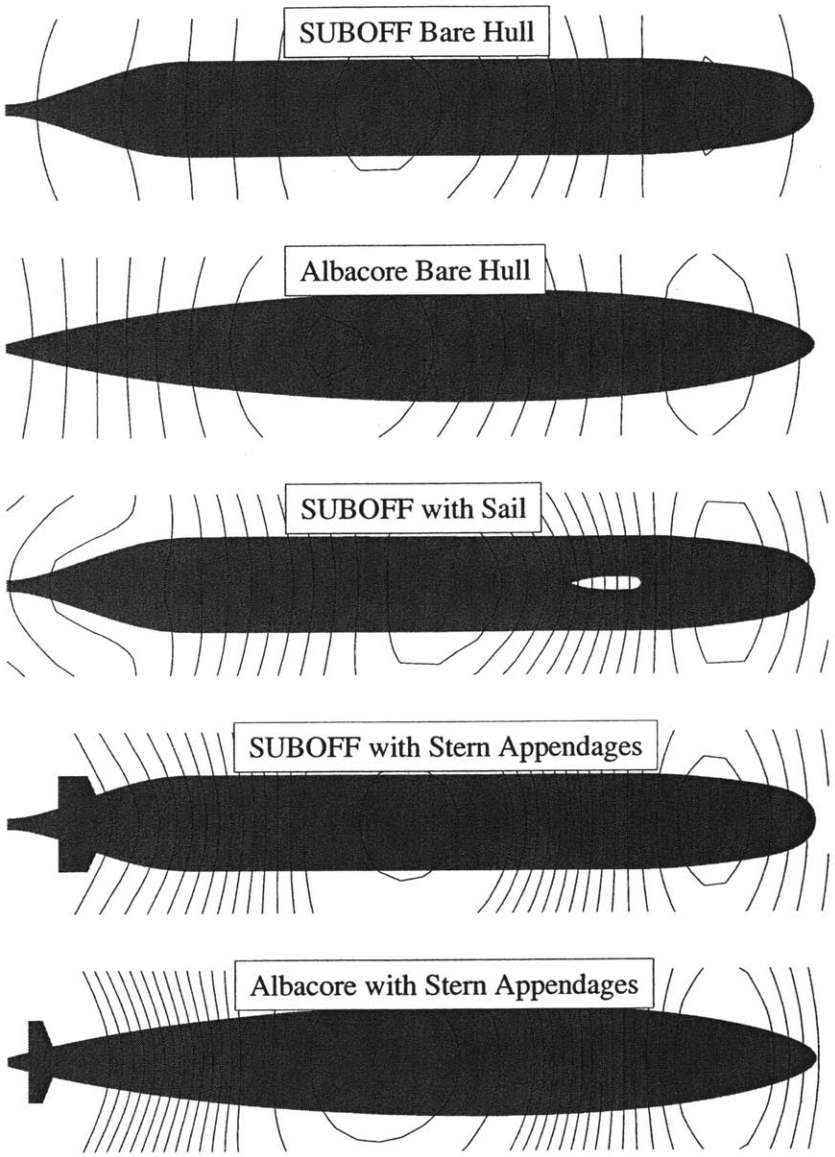

Figure 9-13: Free-surface wave elevations. $Z_{CG}/L = -0.2$, $Fr_L = 0.4$, $\alpha = 0°$, $Re_L = 14 \times 10^7$. The grid resolutions for the five geometries are from top to bottom: $80 \times 24 \times 48$, $80 \times 24 \times 48$, $96 \times 24 \times 48$, $112 \times 48 \times 48$ and $112 \times 48 \times 48$. The same elevations are plotted for each geometry. Negative elevations (troughs) are indicated by dashed contours. This figure serves to illustrate why the vertical force and pitching moment change with respect to geometry at shallow depths. The stern appendages have a significant impact on the free-surface disturbance.

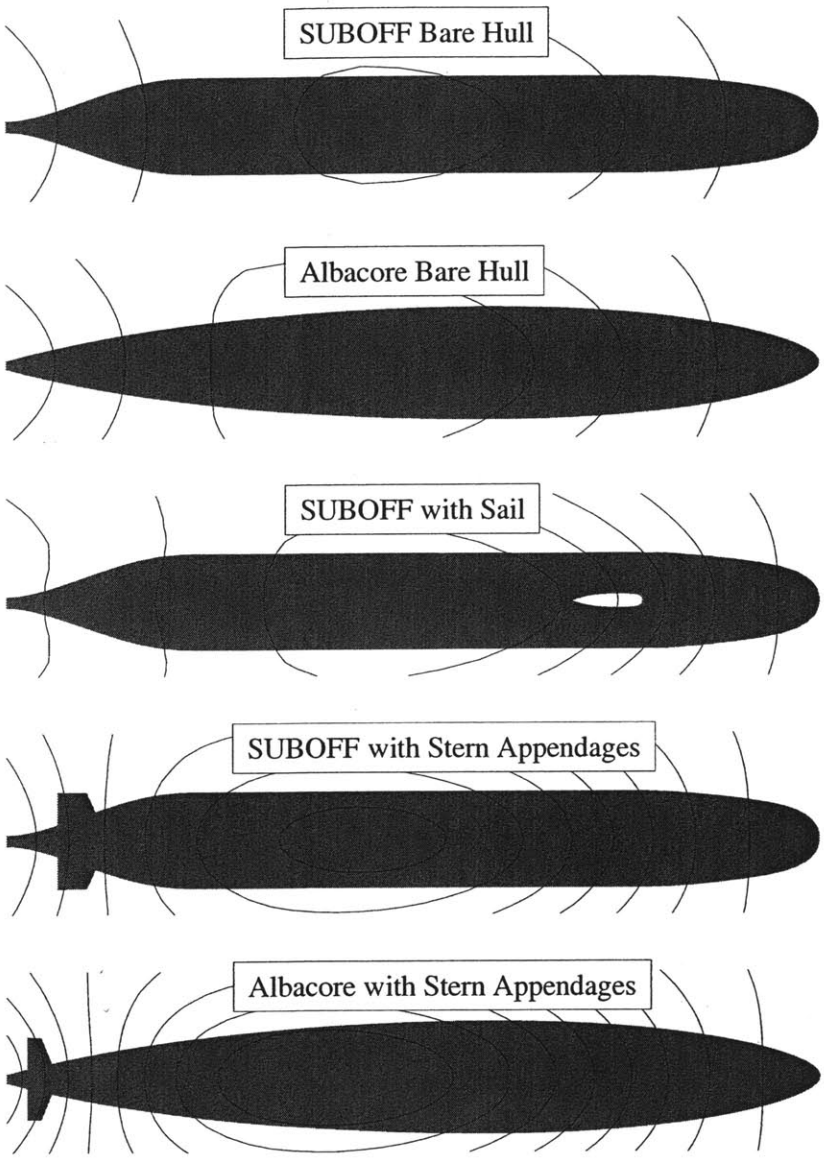

Figure 9-14: Free-surface wave elevations. $Z_{CG}/L = -0.175$, $Fr_L = 0.7$, $\alpha = 0°$, $Re_L = 14 \times 10^7$. The grid resolutions for the five geometries are from top to bottom: $80 \times 24 \times 48$, $80 \times 24 \times 48$, $96 \times 24 \times 48$, $112 \times 48 \times 48$ and $112 \times 48 \times 48$. The same elevations are plotted for each geometry. Negative elevations (troughs) are indicated by dashed contours. This figure serves to illustrate why the vertical force and pitching moment change with respect to geometry at shallow depths. The stern appendages have a significant impact on the free-surface disturbance.

These coefficients, Z'_w and M'_w, for the five geometries as functions of depth and Froude number are shown in Figures 9-15 thru 9-19. The effect of speed and depth on Z'_w and M'_w is quite significant. The tendency for small deviations in pitch angle to cause large changes in vertical force and pitching moment is, in general, increased with a decrease in vehicle depth.

It is not entirely clear from these figures, but inspection of the calculations reveals that as Froude number is increased while depth is kept constant at $Z_{CG}/L = -0.175$ Z'_w actually changes sign for all five geometries. This implies that positive pitch angles cause a *decrease* in vertical force and negative pitch angles cause an *increase* in vertical force for $Fr_L \approx 0.5$.

Another interesting result can be seen in Figure 9-17. The Z'_w coefficient for the SUBOFF with sail configuration is not a function of speed or depth for $Fr_L > 0.6$. This implies that the free-surface waves near the body generated by the body are not dependent on the angle of attack at high speeds.

Similar reasoning can be applied to Figures 9-15 and 9-16 to infer that the free-surface waves generated by the bare hull configurations are only slightly dependent on the angle of attack for $Fr_L > 0.6$.

The M'_w coefficients are generally better "behaved" in that they tend to be more a function of depth than Froude number for all geometries.

Figures 9-18 and 9-19 indicate that the stern appendages have a significant impact on the vertical plane maneuvering coefficients as expected. The magnitude of both Z'_w and M'_w for the appended bodies was greater than that for the unappended bodies.

Due to the comprehensive number of calculations, performed it is possible to calculate maneuvering coefficients that are functions of speed and depth. These coefficients could be used to directly indicate the maneuvering characteristics of the submarines with respect to speed and depth. The magnitude of these coefficients can be approximated by observing the gradients in Figures 9-15 thru 9-19. In other words, closely spaced contour lines in these figures imply that vehicle is unstable in this region. By this reasoning all vehicles are unstable in shallow depths near $Fr_L = 0.4$.

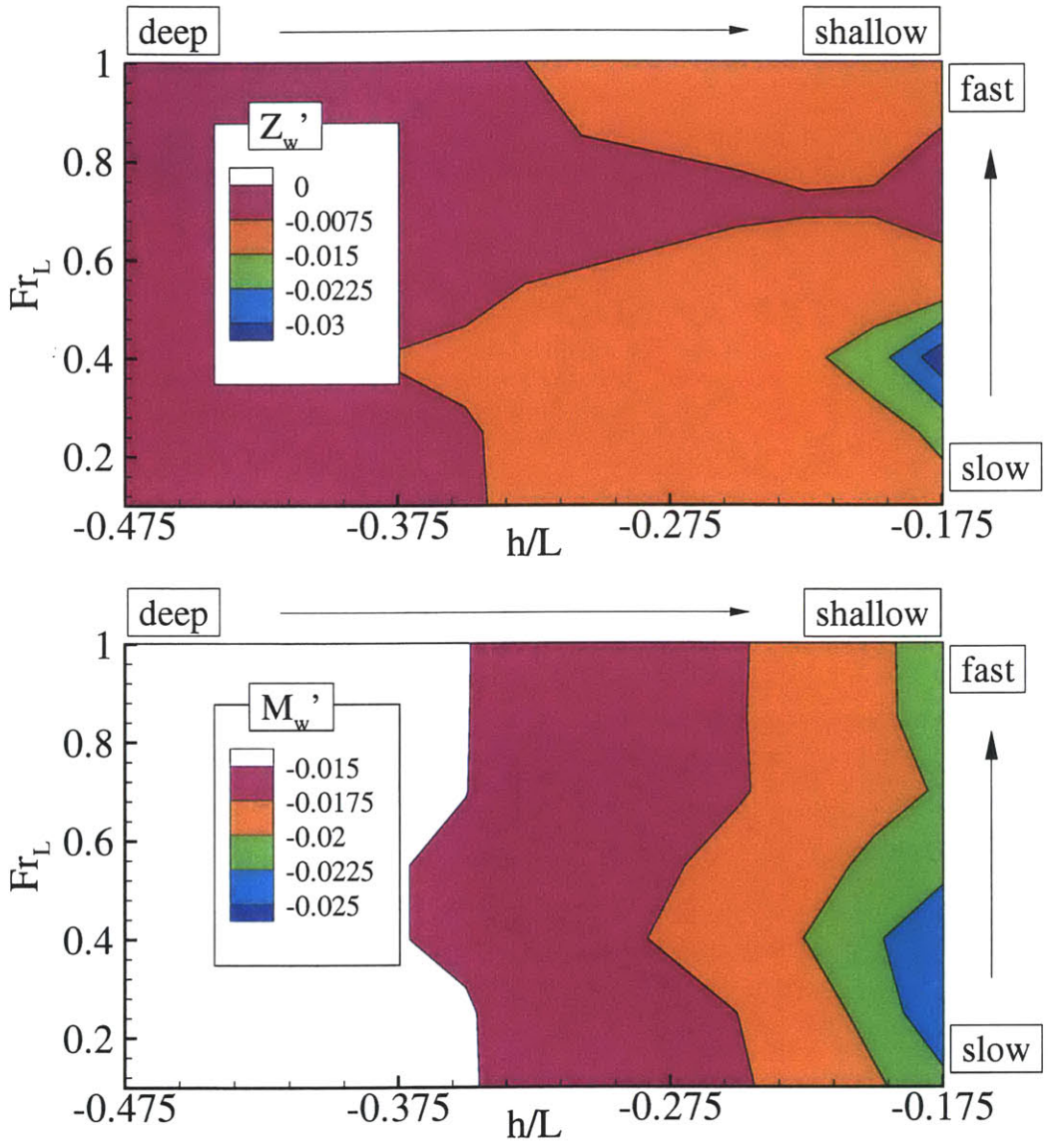

Figure 9-15: Vertical plane maneuvering coefficients for Albacore bare hull as a function of depth and Froude number. Based on calculations with pitch angles of $-2°$, $0°$ and $2°$. ($80 \times 24 \times 48$).

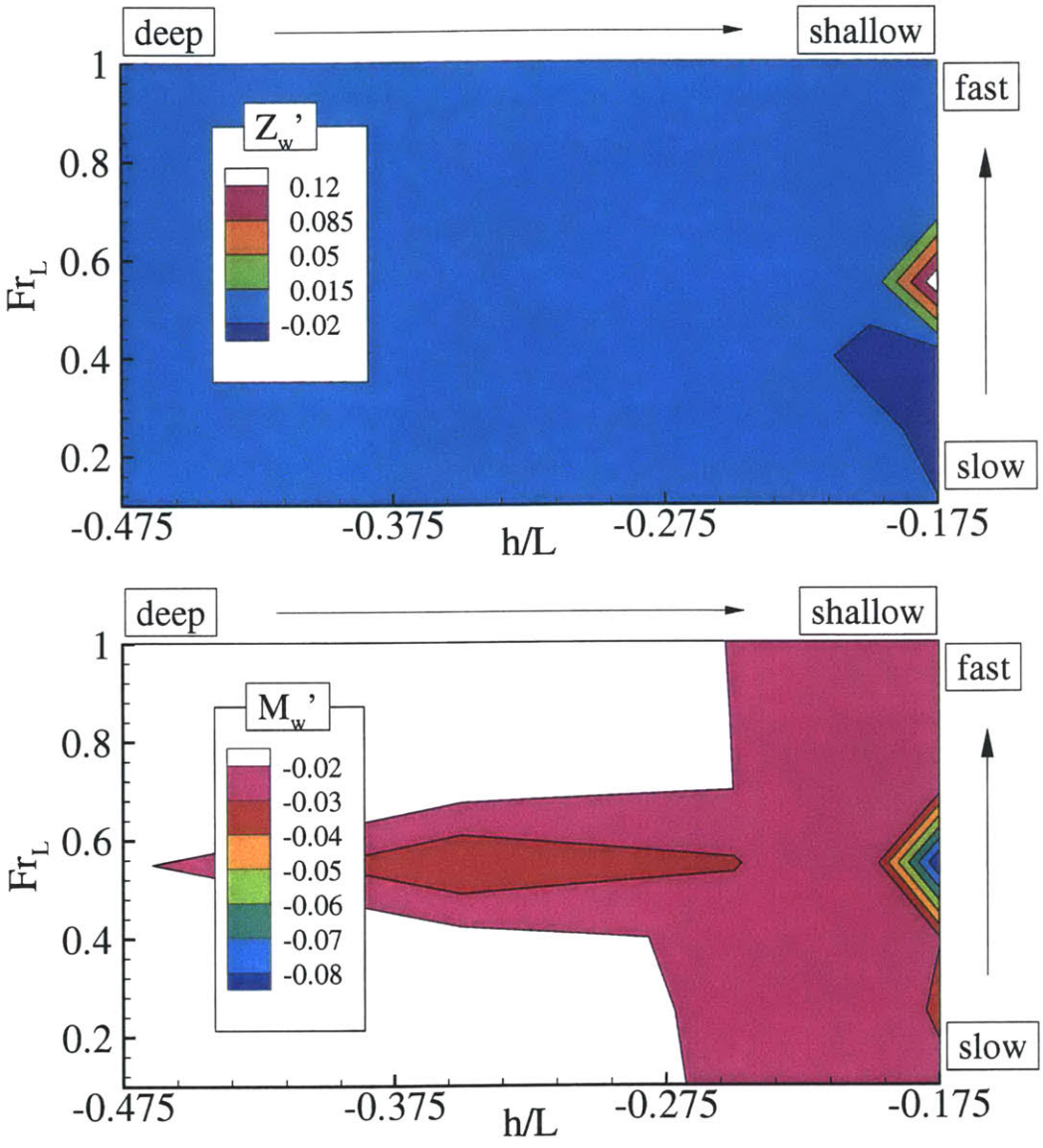

Figure 9-16: Vertical plane maneuvering coefficients for SUBOFF bare hull as a function of depth and Froude number.Based on calculations with pitch angles of $-2°$, $0°$ and $2°$. ($80 \times 24 \times 48$).

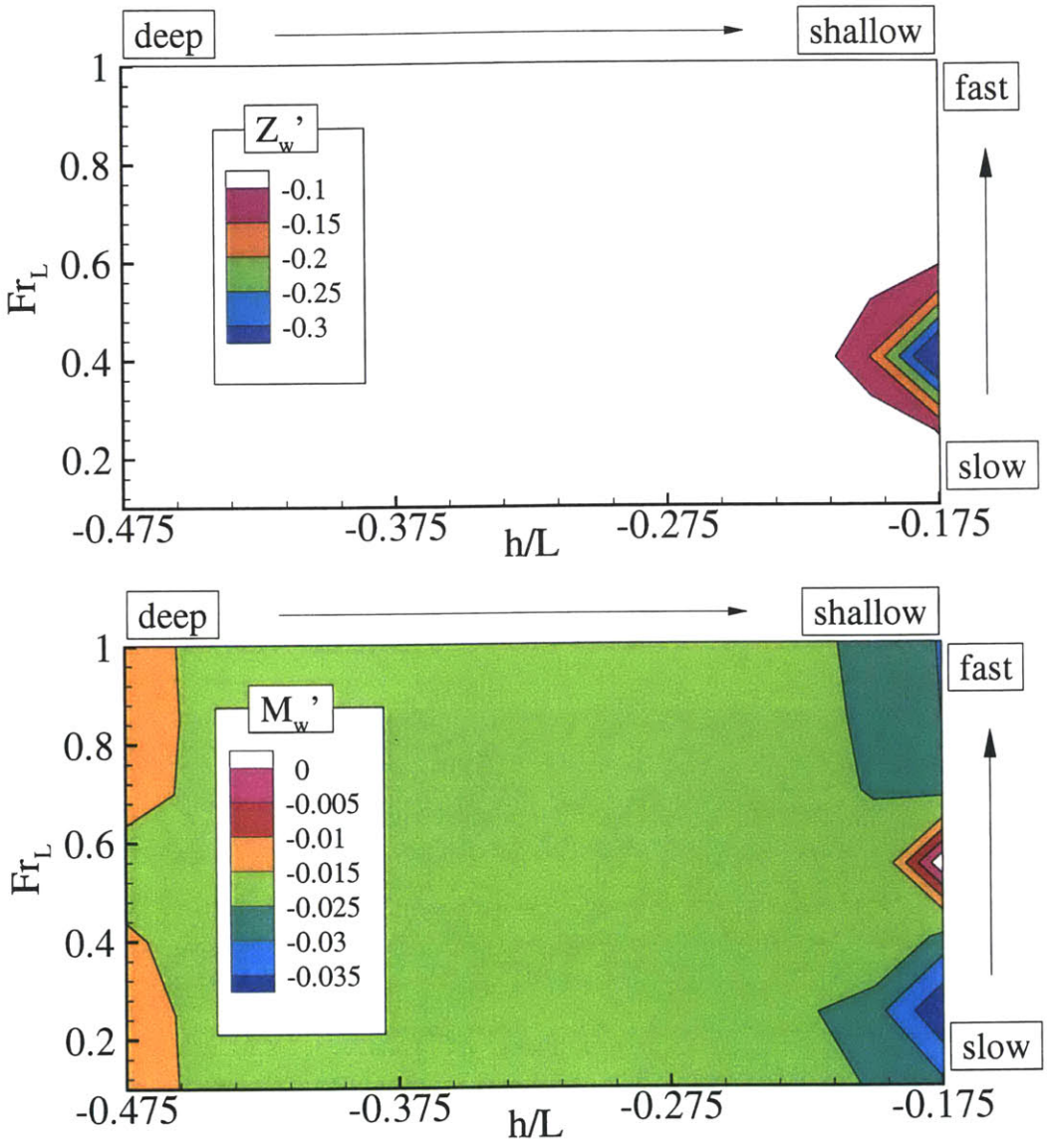

Figure 9-17: Vertical plane maneuvering coefficients for SUBOFF with sail as a function of depth and Froude number. Based on calculations with pitch angles of $-2°$, $0°$ and $2°$. ($96 \times 24 \times 48$).

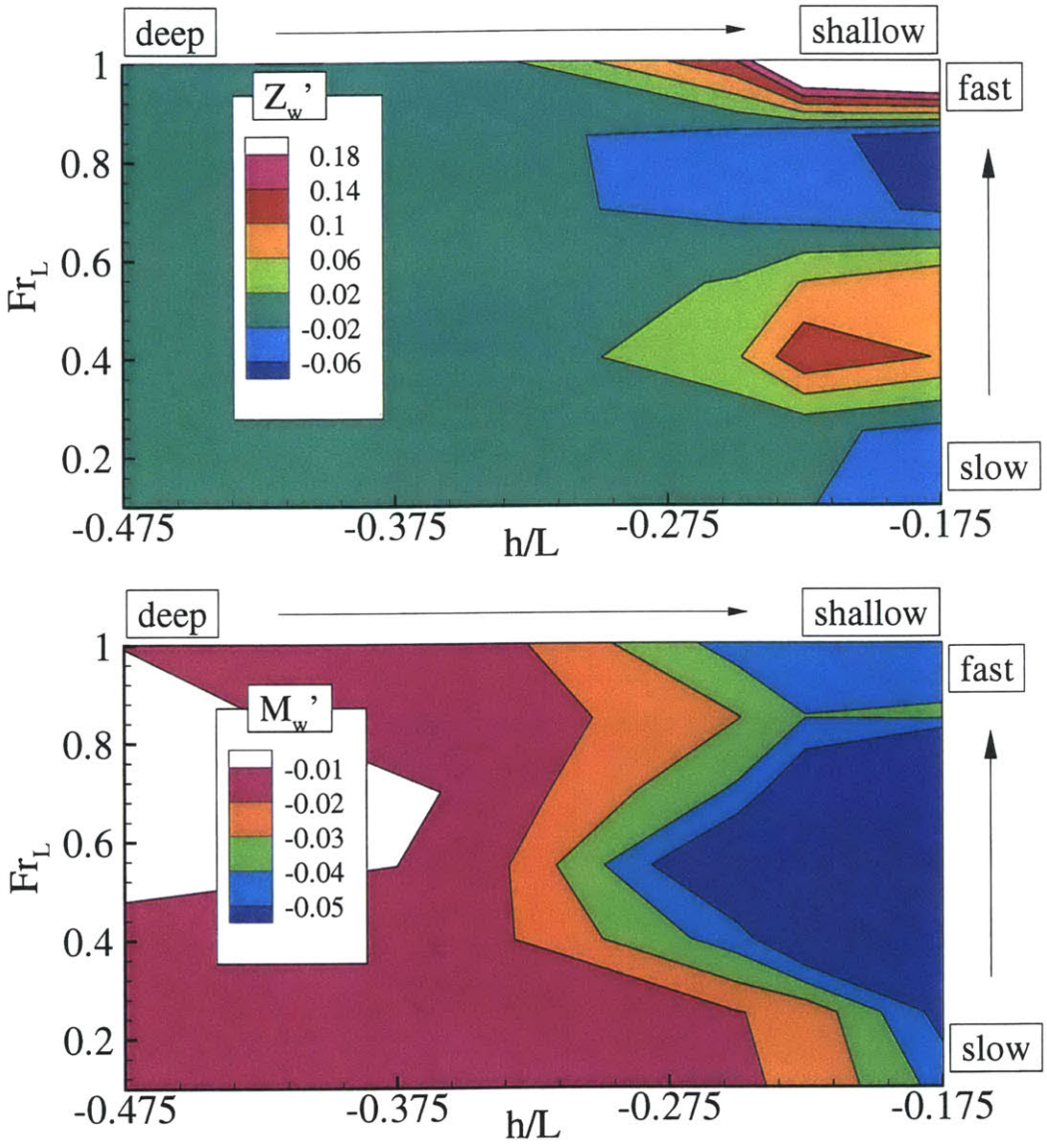

Figure 9-18: Vertical plane maneuvering coefficients for SUBOFF with stern appendages as a function of depth and Froude number. Based on calculations with pitch angles of $-2°$, $0°$ and $2°$. $(112 \times 48 \times 48)$.

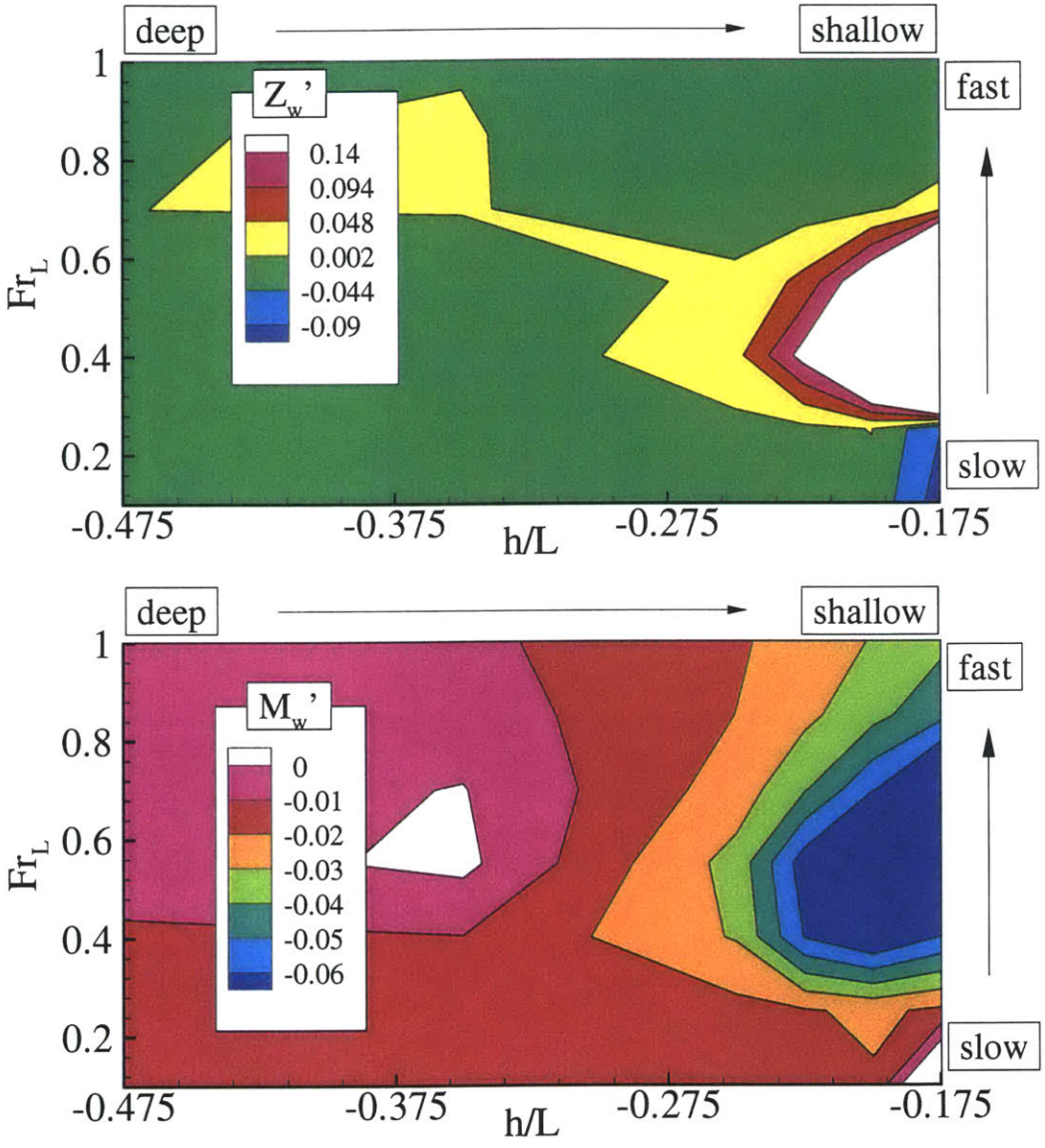

Figure 9-19: Vertical plane maneuvering coefficients for Albacore with stern appendages as a function of depth and Froude number. Based on calculations with pitch angles of $-2°$, $0°$ and $2°$. $(112 \times 48 \times 48)$.

9.5 Summary

The method developed here was efficient and robust enough to allow the development of a comprehensive database of maneuvering coefficients to assist in the complex task of designing submarines. A sophisticated data management system was developed to perform and manage all stages of the several thousand unique computations necessary to create this database.

Due to the large number of computations performed, a new type of map was created to visualize the results. Traditional line plots of coefficients versus one parameter were discarded in favor of contour maps of coefficients versus two parameters, e.g. speed and depth. These maps can be used to quickly identify combinations of operating conditions where the submerged vehicle is unstable. The concept of the coefficient map can be applied to virtually any combination of parameters of interest.

The results of the parameter studies indicate that vertical force, pitching moment and vertical plane maneuvering coefficients are significantly effected by geometry, speed and depth. The effect of geometry includes the presence or absence of appendages as well as the shape of the hull.

The use of free-surface disturbance patterns was found to be useful in understanding why forces, moments and maneuvering coefficients are so strongly dependent on geometry, speed and depth.

The vertical plane maneuvering coefficients were calculated for all geometries at all conditions by varying the angle of attack of the body at all conditions. Several interesting observations were made from these results. For example, it was observed that Z'_w was independent of speed and depth for $Fr_L > 0.6$ for the SUBOFF and Albacore bare hulls and the SUBOFF with sail configurations. This implies that the near-body free-surface disturbances created by the bodies was not altered by the angle of attack at high speeds.

Several other maneuvering coefficient could be computed from this data. These coefficients could be used to directly predict the maneuvering characteristics of the submarine with respect to speed and depth. These coefficients can be approximated

by observing the gradient of the vertical force, the pitching moment and the vertical plane maneuvering coefficients with respect to both speed and depth. This information can be used to guide the design of submarines operating near the free surface.

Finally, because the new method is efficient and robust many more parameter studies can be performed with relative ease. For example, another study underway is addressing the effect of the length of the parallel middle body on the performance of submarines.

Chapter 10

Surface Wake Patterns

10.1 Introduction

No discussion of the maneuvering characteristics of near-surface submarines would be complete without the consideration of the free-surface wakes generated by the submarines. As demonstrated in the previous chapter free-surface wakes interact with the body to modify their maneuvering characteristics and performance. Free-surface wakes also tend to be very durable and easily detectable via satellite instrumentation. Proper calibration of satellite image analysis can elucidate the size, speed, location, depth and direction of slightly to moderately submerged vehicles.

It is important to note that there is no experimental data with which to compare the results presented in this chapter. It is equally important to understand, however, this does not mean that the results presented here are of no use. Given the constraints of the present research, the calculations of the free-surface wakes were verified to the greatest extent possible, where verification is defined loosely as having *solved the equations right.* In other words, the solutions presented here were iteratively converged, found to be insensitive to grid resolution and qualitatively consistent with the results that were expected.

Further research is needed to validate the predictions of the free-surface wakes as experimental data becomes available.

10.2 Surface Wakes

A number of parameter studies were performed including speed, depth and geometry. The predictions of the free-surface elevations were made by the FKX code as the very last step of the coupling procedure. Many thousands of such predictions were made. Only a selected few are presented here. Those presented here serve to illustrate the effects that speed, depth and geometry have on the free-surface disturbance.

Figures 10-1 - 10-4 show the free-surface wakes for the SUBOFF bare hull, Albacore bare hull, SUBOFF with stern appendages and Albacore with stern appendages for three different speeds at a depth of $Z_{CG}/L = -0.25$.

Clearly, the wave patterns are dependent on the speed of the body. The lengths of the waves generated are approximately equal to twice the Froude number. At this scale the influence of the geometry on the free-surface disturbance is barely noticeable. Distinct differences are seen at higher resolution as was shown in the previous chapter.

However, these similarities indicate that it may be difficult to distinguish geometrical differences via satellite imagery.

The free-surface wakes created by the five submarine configurations at a depth of $Z_{CG}/L = -0.25$ are shown in Figures 10-5 and 10-6 at 0° and 2° angles of attack, respectively.

It is somewhat easier in these figures to see the subtle differences in free-surface wakes caused by the geometric variations. These differences are primarily confined to small differences in wave slope. The SUBOFF geometries produce a slightly steeper bow wave due to the blunter nose on these bodies. The sail also increases the slope of the bow wave.

Differences aft of the midbody are not prominent. It may be difficult to distinguish geomtries via satellite imagery of their wakes.

10.3 Summary

The method developed here was able to predict the free-surface disturbance as a function of speed, depth, geometry and angle of attack. The method was shown to be both robust and efficient. Several thousand free surface wakes were calculated in this research. Only a small fraction of those are shown here.

The free-surface disturbances were shown to

Relatively subtle differences in the free-surface disturbances can serve to distinguish between geometries.

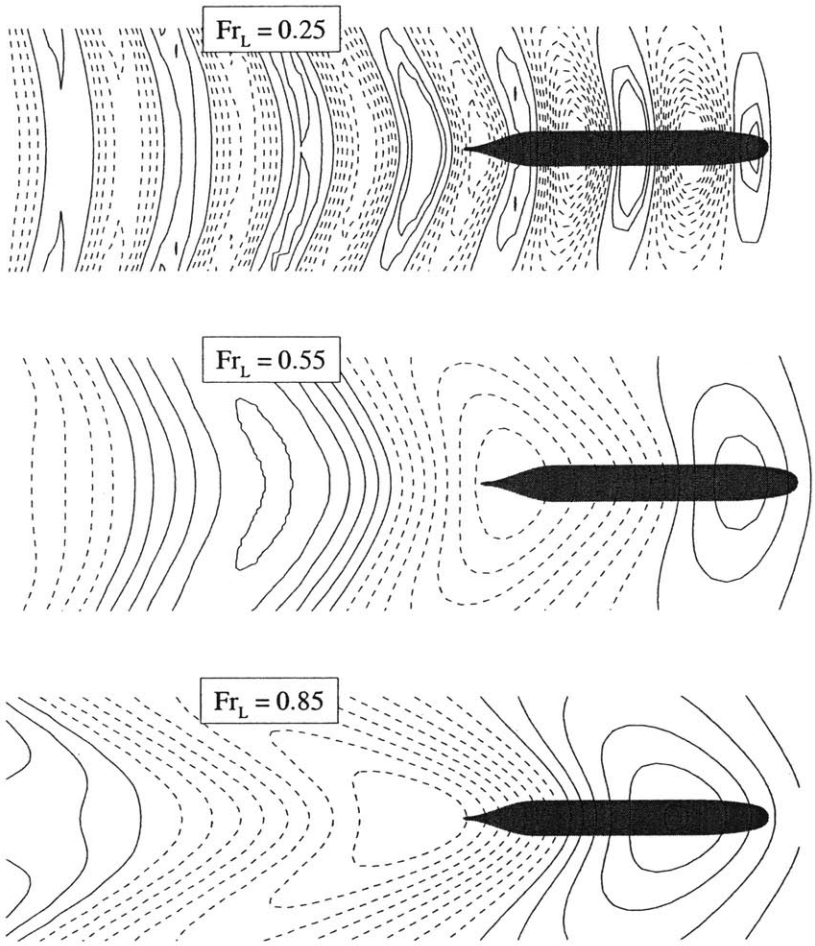

Figure 10-1: Free-surface wave elevations SUBOFF bare hull. $Z_{CG}/L = -0.25$, $\alpha = 0°$, $Re_L = 14 \times 10^7$. The wave elevations shown are different for each speed. Negative elevations (troughs) are indicated by dashed contours.

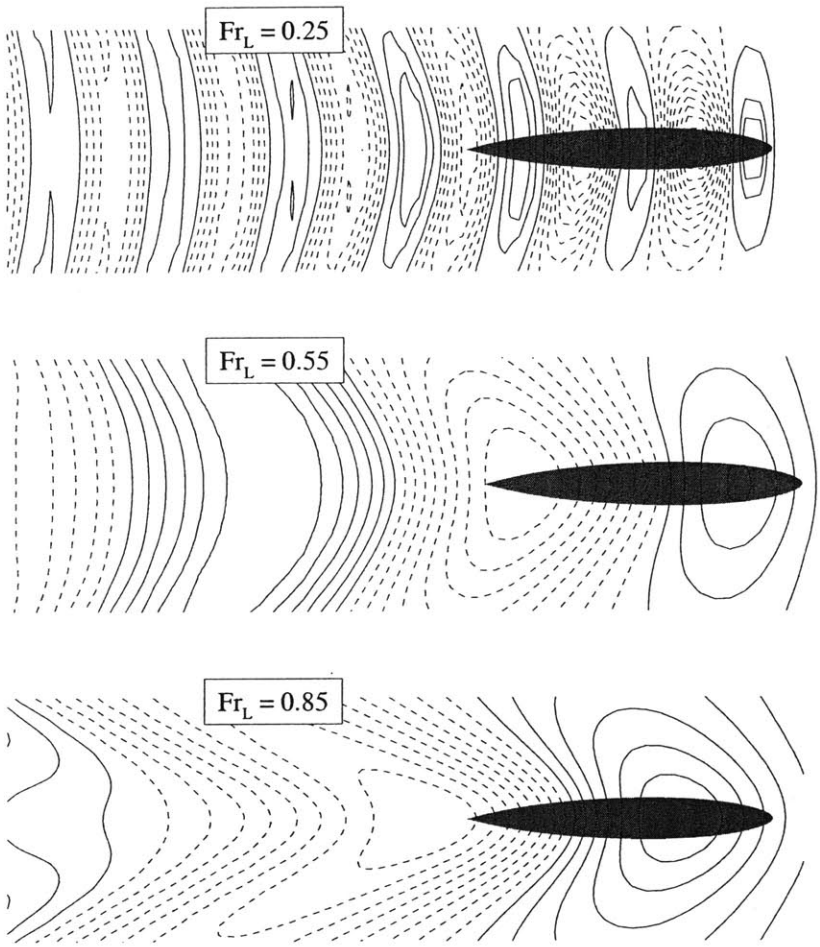

Figure 10-2: Free-surface wave elevations Albacore bare hull. $Z_{CG}/L = -0.25$, $\alpha = 0°$, $Re_L = 14 \times 10^7$. The wave elevations shown are different for each speed. Negative elevations (troughs) are indicated by dashed contours.

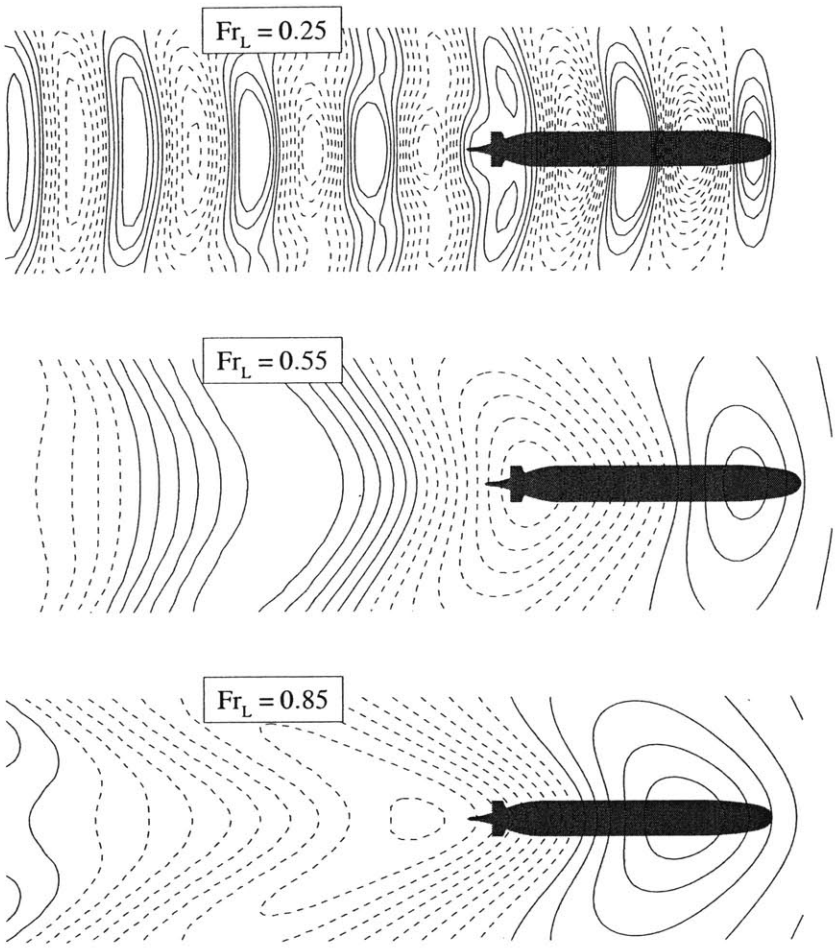

Figure 10-3: Free-surface wave elevations SUBOFF with stern appendages. $Z_{CG}/L = -0.25$, $\alpha = 0°$, $Re_L = 14 \times 10^7$. The wave elevations shown are different for each speed.

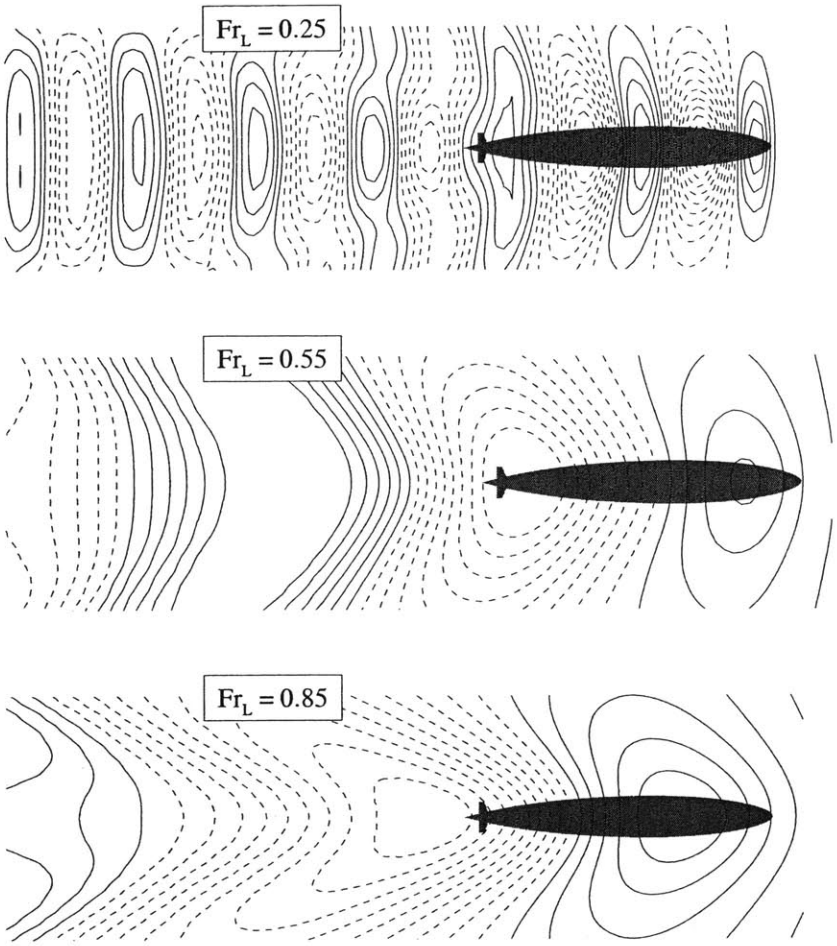

Figure 10-4: Free-surface wave elevations Albacore with stern appendages. $Z_{CG}/L = -0.25$, $\alpha = 0°$, $Re_L = 14 \times 10^7$. The wave elevations shown are different for each speed. Negative elevations (troughs) are indicated by dashed contours.

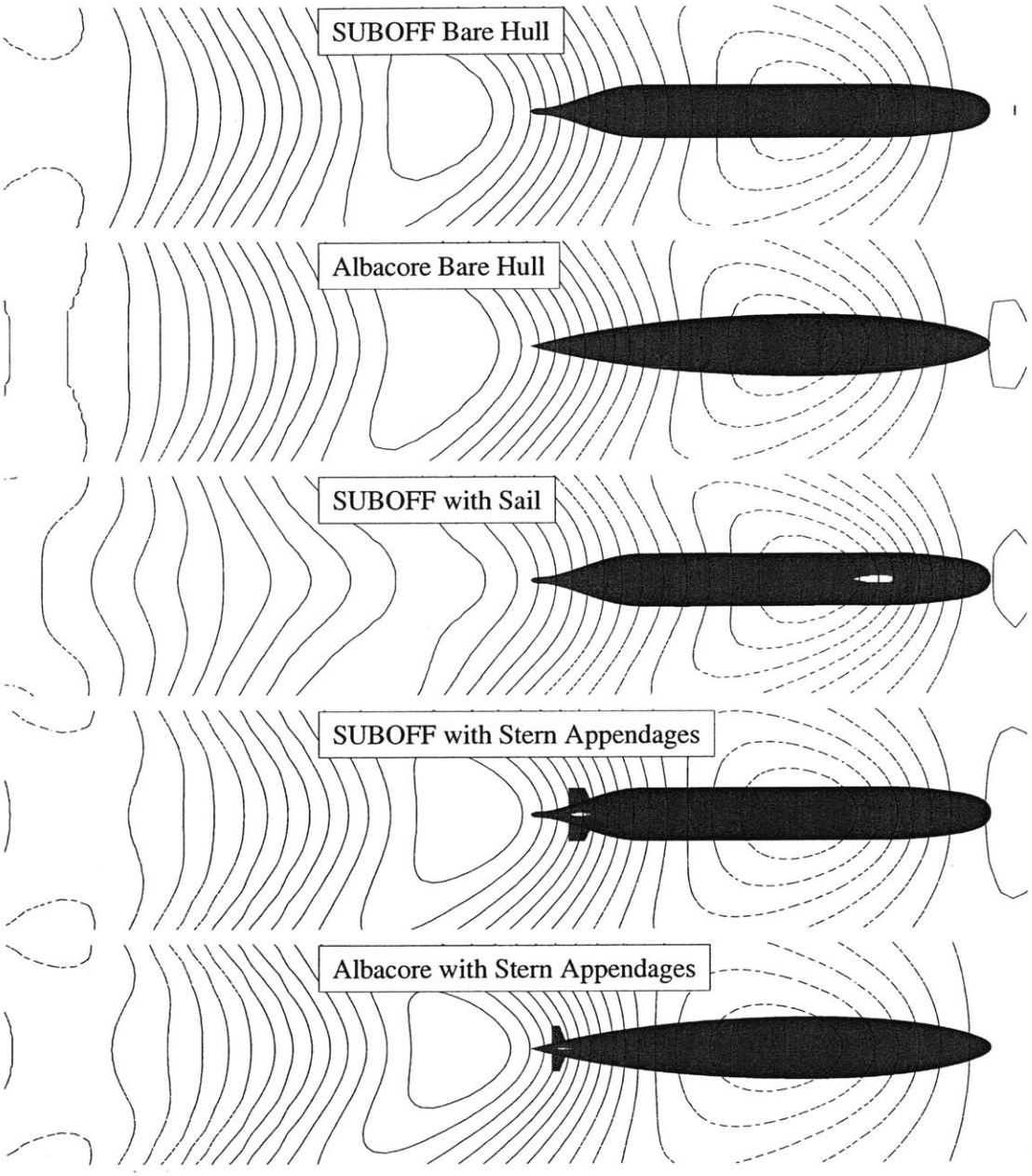

Figure 10-5: Free-surface wave elevations. $Fr_L = 0.55$, $Z_{CG}/L = -0.25$, $\alpha = 0°$, $Re_L = 14 \times 10^7$. Negative elevations (troughs) are indicated by dashed contours.

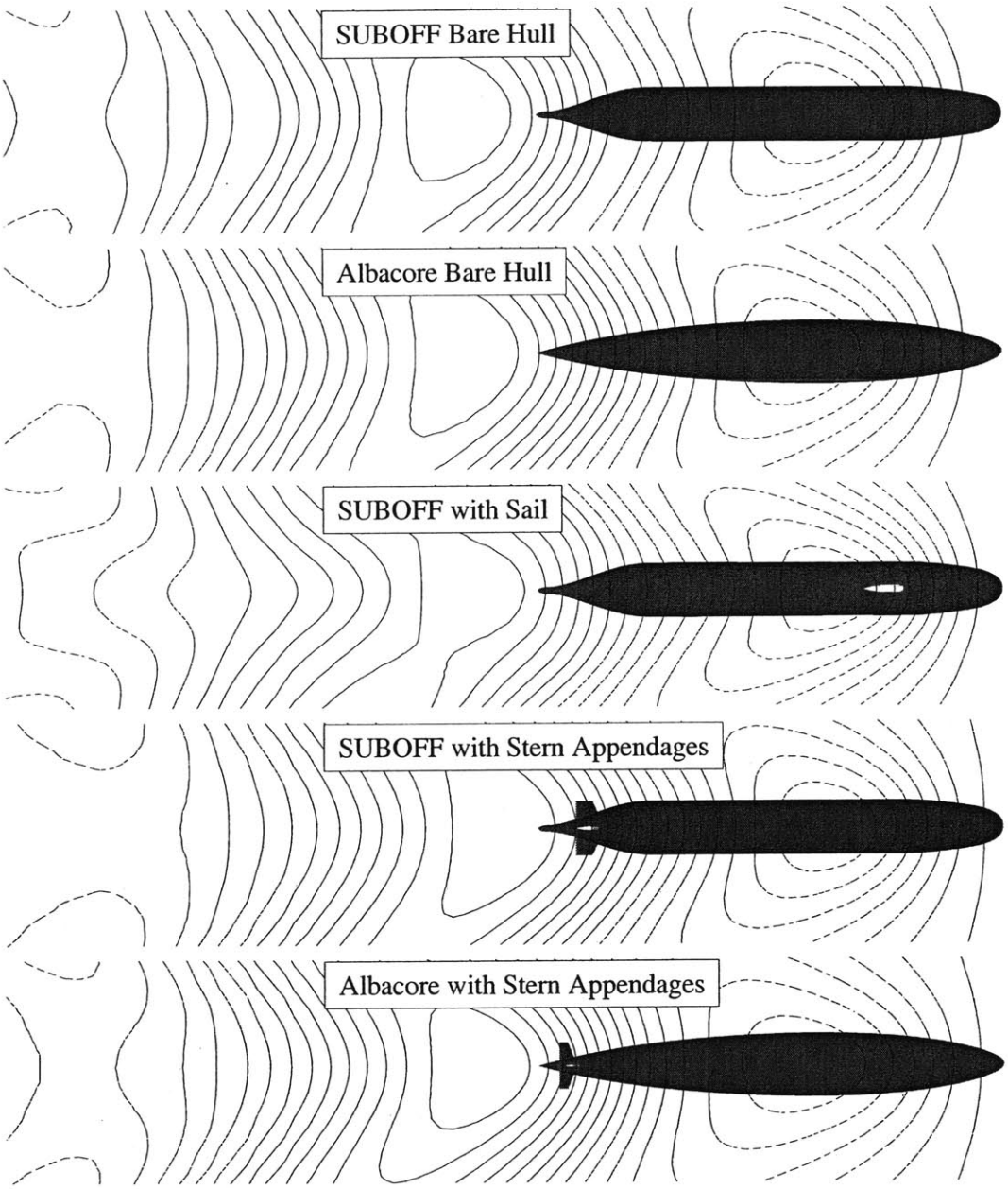

Figure 10-6: Free-surface wave elevations. $Fr_L = 0.55$, $Z_{CG}/L = -0.25$, $\alpha = 2°$, $Re_L = 14 \times 10^7$. Negative elevations (troughs) are indicated by dashed contours.

Chapter 11

Conclusion

The method developed in the present research is an efficient and robust technique for calculating the forces, moments and maneuvering coefficients on submerged vehicles as functions of depth, Froude number and geometry. This method can be a useful tool for both experimentalists and vehicle designers.

A comprehensive study to verify and validate the method was undertaken. This included never before performed verification and validation of the stand-alone RANS code as well as of the coupled method. Considerable effort was devoted to ensure that acceptable iterative convergence, grid convergence and comparisons with available data were made.

Five different geometries were considered: SUBOFF bare hull, SUBOFF with sail, SUBOFF with stern appendages, Albacore bare hull, Albacore with stern appendages. Three levels of grid resolution were used for each geometry to establish the sensitivity of the solution to grid resolution. Calculations were made for each geometry at eight speeds, eight depths and five angles of attack.

Several thousand unique calculations were made with various Froude number, depth, angle of attack, grid and geometry variations on a computer no faster than a 1 GHz PC. This was possible because of the efficiency and reliability of the GRID, IFLOW and FKX codes. In addition it would not have been possible to complete so many calculations in such a short time without the use of shell scripts for the pre- and postprocessing as well as the coupling of the IFLOW and FKX codes.

The results of these thousands of calculations have been compiled into the largest database of computed maneuvering coefficients available today. A new technique to visualize such data was developed to assist in understanding the dependencies of the coefficients on two parameters.

It has been shown that the vertical plane forces, moments and maneuvering coefficients are strongly dependent on vehicle speed, depth and geometry. As was expected the surface waves generated are also strongly dependent on the same variables. It was demonstrated that the surface wave patterns can be used to better explain the complex relationships between speed, depth, geometry and performance.

The limitations of the method are detailed in Chapter 8. Experimentalists can use this method and/or these results to quantify the effects of the free-surface on their experimental measurements within the mentioned limits of the method.

Designers can use this method to better understand and account for the complexity of the relationships between geometry, depth, Froude number and vertical force and pitching moment for near-surface submarine operations.cha

In addition, surface wave elevations computed by this method can be used to calibrate satellite imaging techniques to better determine vehicle speed, depth, location, direction and type.

Finally, much experimental data remains to be collected to validate the new method presented here. Measurements needed include both the maneuvering coefficients and the free surface wakes.

Appendix A

Maneuvering Coefficients

Table A.1: Maneuvering Coefficients for SUBOFF Bare Hull.

Z_{CG}/L	Fr_L	$Z' \times 10^{-3}$	$M' \times 10^{-3}$	$Z'_w \times 10^{-5}$	$M'_w \times 10^{-5}$
-0.500	0.10	-0.006	-0.014	-0.564	-1.405
-0.500	0.25	-0.006	-0.014	-0.556	-1.409
-0.500	0.40	-0.006	-0.014	-0.558	-1.413
-0.500	0.55	-0.006	-0.014	-0.574	-1.410
-0.500	0.70	-0.006	-0.014	-0.575	-1.407
-0.500	0.85	-0.006	-0.014	-0.582	-1.405
-0.500	1.00	-0.006	-0.014	-0.578	-1.407
-0.350	0.10	-0.007	-0.016	-0.694	-1.635
-0.350	0.25	-0.007	-0.016	-0.694	-1.636
-0.350	0.40	-0.007	-0.017	-0.712	-1.664
-0.350	0.55	-0.010	-0.039	-0.993	-3.888
-0.350	0.70	-0.006	-0.016	-0.635	-1.636
-0.350	0.85	-0.006	-0.016	-0.648	-1.632
-0.350	1.00	-0.007	-0.016	-0.659	-1.633
-0.250	0.10	-0.011	-0.021	-1.086	-2.078
-0.250	0.25	-0.011	-0.021	-1.102	-2.101
-0.250	0.40	-0.013	-0.022	-1.255	-2.154
-0.250	0.55	-0.019	-0.031	-1.874	-3.102
-0.250	0.70	-0.007	-0.020	-0.667	-2.001
-0.250	0.85	-0.007	-0.020	-0.678	-2.005
-0.250	1.00	-0.008	-0.020	-0.751	-2.011
-0.225	0.10	-0.013	-0.023	-1.277	-2.257
-0.225	0.25	-0.013	-0.023	-1.320	-2.307
-0.225	0.40	-0.016	-0.024	-1.645	-2.362
-0.225	0.55	-0.012	-0.021	-1.158	-2.135
-0.225	0.70	-0.007	-0.021	-0.688	-2.129
-0.225	0.85	-0.007	-0.021	-0.660	-2.139
-0.225	1.00	-0.008	-0.021	-0.759	-2.148
-0.200	0.10	-0.016	-0.025	-1.554	-2.501
-0.200	0.25	-0.017	-0.026	-1.668	-2.605
-0.200	0.40	-0.024	-0.026	-2.381	-2.603
-0.200	0.55	-0.015	-0.023	-1.470	-2.261
-0.200	0.70	-0.007	-0.023	-0.743	-2.279
-0.200	0.85	-0.006	-0.023	-0.647	-2.301
-0.200	1.00	-0.008	-0.023	-0.783	-2.318
-0.175	0.10	-0.020	-0.028	-1.958	-2.847
-0.175	0.25	-0.023	-0.031	-2.342	-3.091
-0.175	0.40	-0.042	-0.030	-4.187	-2.982
-0.175	0.55	0.146	-0.090	14.619	-9.014
-0.175	0.70	-0.010	-0.025	-0.965	-2.543
-0.175	0.85	-0.008	-0.026	-0.805	-2.569
-0.175	1.00	-0.009	-0.026	-0.934	-2.586

Table A.2: Maneuvering Coefficients for Albacore Bare Hull.

Z_{CG}/L	Fr_L	$Z' \times 10^{-3}$	$M' \times 10^{-3}$	$Z'_w \times 10^{-5}$	$M'_w \times 10^{-5}$
-0.500	0.10	-0.007	-0.014	-0.564	-1.405
-0.500	0.25	-0.007	-0.014	-0.556	-1.409
-0.500	0.40	-0.007	-0.014	-0.558	-1.413
-0.500	0.55	-0.007	-0.014	-0.574	-1.410
-0.500	0.70	-0.007	-0.014	-0.575	-1.407
-0.500	0.85	-0.007	-0.014	-0.582	-1.405
-0.500	1.00	-0.007	-0.014	-0.578	-1.407
-0.350	0.10	-0.007	-0.015	-0.694	-1.635
-0.350	0.25	-0.007	-0.015	-0.694	-1.636
-0.350	0.40	-0.008	-0.015	-0.712	-1.664
-0.350	0.55	-0.007	-0.015	-0.993	-3.888
-0.350	0.70	-0.007	-0.015	-0.635	-1.636
-0.350	0.85	-0.007	-0.015	-0.648	-1.632
-0.350	1.00	-0.007	-0.015	-0.659	-1.633
-0.250	0.10	-0.009	-0.017	-1.086	-2.078
-0.250	0.25	-0.009	-0.018	-1.102	-2.101
-0.250	0.40	-0.011	-0.019	-1.255	-2.154
-0.250	0.55	-0.009	-0.018	-1.874	-3.102
-0.250	0.70	-0.007	-0.017	-0.667	-2.001
-0.250	0.85	-0.008	-0.017	-0.678	-2.005
-0.250	1.00	-0.008	-0.017	-0.751	-2.011
-0.225	0.10	-0.010	-0.018	-1.277	-2.257
-0.225	0.25	-0.010	-0.019	-1.320	-2.307
-0.225	0.40	-0.013	-0.020	-1.645	-2.362
-0.225	0.55	-0.009	-0.019	-1.158	-2.135
-0.225	0.70	-0.007	-0.018	-0.688	-2.129
-0.225	0.85	-0.008	-0.018	-0.660	-2.139
-0.225	1.00	-0.008	-0.018	-0.759	-2.148
-0.200	0.10	-0.011	-0.020	-1.554	-2.501
-0.200	0.25	-0.012	-0.021	-1.668	-2.605
-0.200	0.40	-0.019	-0.022	-2.381	-2.603
-0.200	0.55	-0.009	-0.021	-1.470	-2.261
-0.200	0.70	-0.007	-0.019	-0.743	-2.279
-0.200	0.85	-0.008	-0.020	-0.647	-2.301
-0.200	1.00	-0.008	-0.020	-0.783	-2.318
-0.175	0.10	-0.012	-0.022	-1.958	-2.847
-0.175	0.25	-0.017	-0.025	-2.342	-3.091
-0.175	0.40	-0.035	-0.025	-4.187	-2.982
-0.175	0.55	-0.009	-0.022	14.619	-9.014
-0.175	0.70	-0.007	-0.020	-0.965	-2.543
-0.175	0.85	-0.007	-0.021	-0.805	-2.569
-0.175	1.00	-0.008	-0.021	-0.934	-2.586

Table A.3: Maneuvering Coefficients for SUBOFF with Sail.

Z_{CG}/L	Fr_L	$Z' \times 10^{-3}$	$M' \times 10^{-3}$	$Z'_w \times 10^{-5}$	$M'_w \times 10^{-5}$
-0.500	0.10	-0.020	-0.014	-0.564	-1.405
-0.500	0.25	-0.019	-0.014	-0.556	-1.409
-0.500	0.40	-0.020	-0.014	-0.558	-1.413
-0.500	0.55	-0.022	-0.015	-0.574	-1.410
-0.500	0.70	-0.019	-0.014	-0.575	-1.407
-0.500	0.85	-0.019	-0.014	-0.582	-1.405
-0.500	1.00	-0.019	-0.014	-0.578	-1.407
-0.350	0.10	-0.022	-0.017	-0.694	-1.635
-0.350	0.25	-0.022	-0.017	-0.694	-1.636
-0.350	0.40	-0.024	-0.017	-0.712	-1.664
-0.350	0.55	-0.024	-0.017	-0.993	-3.888
-0.350	0.70	-0.023	-0.017	-0.635	-1.636
-0.350	0.85	-0.023	-0.017	-0.648	-1.632
-0.350	1.00	-0.023	-0.017	-0.659	-1.633
-0.250	0.10	-0.033	-0.021	-1.086	-2.078
-0.250	0.25	-0.034	-0.022	-1.102	-2.101
-0.250	0.40	-0.039	-0.021	-1.255	-2.154
-0.250	0.55	-0.033	-0.022	-1.874	-3.102
-0.250	0.70	-0.034	-0.023	-0.667	-2.001
-0.250	0.85	-0.034	-0.022	-0.678	-2.005
-0.250	1.00	-0.034	-0.022	-0.751	-2.011
-0.225	0.10	-0.038	-0.023	-1.277	-2.257
-0.225	0.25	-0.040	-0.024	-1.320	-2.307
-0.225	0.40	-0.053	-0.023	-1.645	-2.362
-0.225	0.55	-0.044	-0.021	-1.158	-2.135
-0.225	0.70	-0.037	-0.023	-0.688	-2.129
-0.225	0.85	-0.038	-0.024	-0.660	-2.139
-0.225	1.00	-0.039	-0.024	-0.759	-2.148
-0.200	0.10	-0.045	-0.026	-1.554	-2.501
-0.200	0.25	-0.054	-0.028	-1.668	-2.605
-0.200	0.40	-0.151	-0.018	-2.381	-2.603
-0.200	0.55	-0.085	-0.022	-1.470	-2.261
-0.200	0.70	-0.042	-0.025	-0.743	-2.279
-0.200	0.85	-0.043	-0.026	-0.647	-2.301
-0.200	1.00	-0.044	-0.026	-0.783	-2.318
-0.175	0.10	-0.056	-0.029	-1.958	-2.847
-0.175	0.25	-0.103	-0.040	-2.342	-3.091
-0.175	0.40	-0.390	-0.027	-4.187	-2.982
-0.175	0.55	-0.116	0.004	14.619	-9.014
-0.175	0.70	-0.048	-0.028	-0.965	-2.543
-0.175	0.85	-0.054	-0.030	-0.805	-2.569
-0.175	1.00	-0.057	-0.030	-0.934	-2.586

Table A.4: Maneuvering Coefficients for SUBOFF with stern appendages.

Z_{CG}/L	Fr_L	$Z' \times 10^{-3}$	$M' \times 10^{-3}$	$Z'_w \times 10^{-5}$	$M'_w \times 10^{-5}$
-0.500	0.10	-0.010	-0.012	-0.564	-1.405
-0.500	0.25	-0.010	-0.012	-0.556	-1.409
-0.500	0.40	-0.012	-0.012	-0.558	-1.413
-0.500	0.55	-0.011	-0.008	-0.574	-1.410
-0.500	0.70	-0.005	-0.007	-0.575	-1.407
-0.500	0.85	-0.005	-0.008	-0.582	-1.405
-0.500	1.00	-0.006	-0.010	-0.578	-1.407
-0.350	0.10	-0.011	-0.014	-0.694	-1.635
-0.350	0.25	-0.011	-0.014	-0.694	-1.636
-0.350	0.40	-0.014	-0.014	-0.712	-1.664
-0.350	0.55	-0.012	-0.010	-0.993	-3.888
-0.350	0.70	-0.009	-0.010	-0.635	-1.636
-0.350	0.85	-0.009	-0.012	-0.648	-1.632
-0.350	1.00	-0.010	-0.012	-0.659	-1.633
-0.250	0.10	-0.016	-0.019	-1.086	-2.078
-0.250	0.25	-0.014	-0.020	-1.102	-2.101
-0.250	0.40	0.053	-0.045	-1.255	-2.154
-0.250	0.55	0.024	-0.068	-1.874	-3.102
-0.250	0.70	-0.031	-0.042	-0.667	-2.001
-0.250	0.85	-0.033	-0.029	-0.678	-2.005
-0.250	1.00	0.135	-0.045	-0.751	-2.011
-0.225	0.10	-0.018	-0.021	-1.277	-2.257
-0.225	0.25	-0.011	-0.023	-1.320	-2.307
-0.225	0.40	0.132	-0.066	-1.645	-2.362
-0.225	0.55	0.063	-0.109	-1.158	-2.135
-0.225	0.70	-0.043	-0.063	-0.688	-2.129
-0.225	0.85	-0.052	-0.040	-0.660	-2.139
-0.225	1.00	0.313	-0.046	-0.759	-2.148
-0.200	0.10	-0.046	-0.044	-1.554	-2.501
-0.200	0.25	-0.032	-0.054	-1.668	-2.605
-0.200	0.40	0.098	-0.320	-2.381	-2.603
-0.200	0.55	0.098	-0.306	-1.470	-2.261
-0.200	0.70	-0.067	-0.114	-0.743	-2.279
-0.200	0.85	-0.074	-0.038	-0.647	-2.301
-0.200	1.00	0.377	-0.047	-0.783	-2.318
-0.175	0.10	-0.042	-0.025	-1.958	-2.847
-0.175	0.25	-0.011	-0.034	-2.342	-3.091
-0.175	0.40	0.209	-0.020	-4.187	-2.982
-0.175	0.55	0.188	-0.162	14.619	-9.014
-0.175	0.70	-0.056	-0.097	-0.965	-2.543
-0.175	0.85	-0.088	-0.057	-0.805	-2.569
-0.175	1.00	0.474	-0.067	-0.934	-2.586

Table A.5: Maneuvering Coefficients for Albacore with stern appendages.

Z_{CG}/L	Fr_L	$Z' \times 10^{-3}$	$M' \times 10^{-3}$	$Z'_w \times 10^{-5}$	$M'_w \times 10^{-5}$
-0.500	0.10	-0.009	-0.012	-0.564	-1.405
-0.500	0.25	-0.009	-0.012	-0.556	-1.409
-0.500	0.40	-0.013	-0.011	-0.558	-1.413
-0.500	0.55	-0.009	-0.007	-0.574	-1.410
-0.500	0.70	0.001	-0.006	-0.575	-1.407
-0.500	0.85	0.001	-0.008	-0.582	-1.405
-0.500	1.00	-0.002	-0.009	-0.578	-1.407
-0.350	0.10	-0.009	-0.014	-0.694	-1.635
-0.350	0.25	-0.009	-0.014	-0.694	-1.636
-0.350	0.40	-0.030	-0.010	-0.712	-1.664
-0.350	0.55	-0.019	0.002	-0.993	-3.888
-0.350	0.70	0.004	0.000	-0.635	-1.636
-0.350	0.85	0.004	-0.005	-0.648	-1.632
-0.350	1.00	0.001	-0.008	-0.659	-1.633
-0.250	0.10	-0.010	-0.016	-1.086	-2.078
-0.250	0.25	-0.010	-0.017	-1.102	-2.101
-0.250	0.40	0.033	-0.031	-1.255	-2.154
-0.250	0.55	0.009	-0.034	-1.874	-3.102
-0.250	0.70	-0.014	-0.024	-0.667	-2.001
-0.250	0.85	-0.015	-0.020	-0.678	-2.005
-0.250	1.00	-0.015	-0.019	-0.751	-2.011
-0.225	0.10	-0.011	-0.017	-1.277	-2.257
-0.225	0.25	-0.009	-0.019	-1.320	-2.307
-0.225	0.40	0.159	-0.061	-1.645	-2.362
-0.225	0.55	0.060	-0.065	-1.158	-2.135
-0.225	0.70	-0.018	-0.039	-0.688	-2.129
-0.225	0.85	-0.024	-0.028	-0.660	-2.139
-0.225	1.00	-0.022	-0.024	-0.759	-2.148
-0.200	0.10	-0.011	-0.019	-1.554	-2.501
-0.200	0.25	0.003	-0.022	-1.668	-2.605
-0.200	0.40	0.409	-0.072	-2.381	-2.603
-0.200	0.55	0.199	-0.115	-1.470	-2.261
-0.200	0.70	-0.010	-0.058	-0.743	-2.279
-0.200	0.85	-0.036	-0.037	-0.647	-2.301
-0.200	1.00	-0.030	-0.031	-0.783	-2.318
-0.175	0.10	-0.112	0.027	-1.958	-2.847
-0.175	0.25	-0.087	-0.018	-2.342	-3.091
-0.175	0.40	1.073	-0.060	-4.187	-2.982
-0.175	0.55	0.579	-0.202	14.619	-9.014
-0.175	0.70	0.025	-0.082	-0.965	-2.543
-0.175	0.85	-0.042	-0.047	-0.805	-2.569
-0.175	1.00	-0.036	-0.037	-0.934	-2.586

Bibliography

[1] Campana, E., A. Di Mascio., P.G. Esposito, and F. Lalli, "Domain Decomposition in Free Surface Viscous Flows", 6th Conference on Numerical Ship Hydrodynamics, Iowa City, Iowa, 1993.

[2] Chang, J.L.C., and D. Kwak, "On the Method of Pseudo Compressibility for Numerically Solving Incompressible Flows", AIAA Paper-0252, 1984.

[3] Chen, H.-C., W.-M. Lin and K.M. Weems, "Interactive Zonal Approach for Ship Flows Including Viscous and Nonlinear Wave Effects", 6th Conference on Numerical Ship Hydrodynamics, Iowa City, Iowa, 1993.

[4] Chorin, A.J.,"A Numerical Method for Solving Incompressible Viscous Flow Problems", J. Computational Physics, vol. 2, pp. 12-26, 1967.

[5] Cosner, R.R, "Future Requirements in Surface Modeling and Grid Generation," Proceedings of the Surface Modeling, Grid Generation and Related Issues in Computational Fluid Dynamics Workshop, NASA Conference Publication 3291, NASA Lewis Research Center, Cleveland, OH, May 1995.

[6] Dawson, C.W., "A Practical Computer Method for Solving Ship-Wave Problems", Second International Conference on Numerical Ship Hydrodynamics, Berkeley, 1977.

[7] Dempsey, E. M., "Static Stability Characteristics of a Systematic Series of Stern Appendage Control Surfaces on a Body of Revolution", David Taylor Naval Ship Research and Development Center Report 77-0085, Aug. 1977.

[8] Thompson, J.F, Z.U.A. Warsi, C.W. Mastin, *Numerical Grid Generation*, North-Holland, 1985.

[9] Griffin, M.J., T.C. Fu, C.-H. Sung, and T. T. Huang, "Applications of CFD to Compute the Hydrodynamic Interaction of Submarine Appendages", 3rd International Symposium on Performance Enhancement for Marine Applications, Newport, Rhode Island, May 5-8, 1997.

[10] Havelock, T.H., "The Wave Resistance of a Spheroid", Proceedings of the Royal Society of London, Ser. A 131 (1931), pp 275-285.

[11] Hedstrom, G.W., "Nonreflecting Boundary Conditions for Nonlinear Hyperbolic Systems", Journal of Computational Physics, vol. 30, pp. 222-237, 1979.

[12] Hess, J.L. and A.M.O. Smith, "Calculation of Nonlifting Potential Flow about Arbitrary Three-Dimensional Bodies", Journal of Ship Research, Vol. 8, pp 22-44, 1964.

[13] Huang, T.T., T.C. Fu, and C.-H. Sung, "Computation of the Hydrodynamic Characteristics of a Fully Appended Submarine for Design Applications: Part 1 - Current Capability and Future Development", Presented at 1st Symposium on Marine Applications of CFD, McLean, VA, May 19-21, 1998.

[14] Jameson, A, "Multigrid Algorithms for Compressible Flow Calculations", in Multigrid Methods II, Lecture Notes in Mathematics Series, No. 1228, Hackbusch, W., and Trottenberg, U. Eds., Springer-Verlag, New York, 1986.

[15] Noblesse, F. and C. Yang, "Fourier-Kochin Formulation of Wave Diffraction-Radiation by Ships or Offshore Structures", Ship Technology Research, vol. 42, pp. 115-139, 1995.

[16] Noblesse, F., and X.B. Chen, "Decomposition of Free-Surface Effects into Wave and Near-Field Components", Ship Technology Research vol. 42, no. 4, pp. 167-185, 1995.

[17] Noblesse, F., and C. Yang, "Fourier Representation of Near-Field Free-Surface Flows", Ship Technology Research, vol. 43, no. 1, pp. 19-37., 1996

[18] Noblesse, F., X.B. Chen, and C. Yang, "Fourier-Kochin Theory of Free-Surface Flows", 21st Symposium Naval Hydronamics, Trondheim, 1996.

[19] Noblesse, F. and X.B. Chen, "Far-Field and Near-Field Dispersive Waves", Ship Technology Research, Vol. 44, 1997.

[20] Roache, P.J., *Verification and Validation in Computational Science and Engineering*, Hermosa Publishers, Albuquerque, New Mexico, 1998.

[21] Roddy, R.F., "Investigation of the Stability and Control of the DARPA SUBOFF Model (DTRC Model) from Captive-Model Experiments," Report DTRC/SHD-1298-08, Sept. 1990.

[22] Rudy, D.H. and J.C. Strikwerda, "Bounday Conditions for Subsonic Compressible Navier-Stokes Equations", Computers and Fluids, vol. 9, pp. 327-338, 1981.

[23] Scullen, D.C., "Accurate computation of nonlinear free-surface flows", PhD. Thesis, The University of Adelaide, 1998.

[24] Sung, C.-H., M.J. Griffin, J.F. Tsai and T.T. Huang, "Incompressible Flow Computation of Forces and Moments on Bodies of Revolution at Incidence", AIAA 93-0787, 31st AIAA Aerospace Sciences Meeting, Reno, Nevada, January 11-14, 1993.

[25] Sung, C.-H., T.C. Fu, M.J. Griffin, and T.T. Huang, "Toward Accurate Prediction of Forces and Moments on Axisymmetric Bodies at Angle of Attack", Eurovisc Workshop, Emmen, Switzerland, October 28, 1994.

[26] Sung, C.-H., T.C. Fu, M. J. Griffin and T. T. Huang, "Validation of Incompressible Flow Computation of Forces and Moments on Axisymmetric Bodies Undergoing Constant Radius Turning," The Twenty-First Symposium on Naval Hydrodynamics, Trondheim, Norway, June 23-28, 1996.

[27] Sung, C.-H. and M.J. Griffin, "Improvements in Incompressible Turbulent Horseshoe Vortex Juncture Flow Calculations", AIAA 91-0022, 29th Aerospace Sciences Meeting, Reno, Nevada, January 7-10, 1991.

[28] Sung, C.-H., M.J. Griffin and R.M. Coleman, "Numerical Evaluation of Vortex Flow Control Devices", AIAA 91-1825, AIAA 22nd Fluid Dynamics, Plasma Dynamics and Lasers Conference, Honolulu, Hawaii, June 24-26, 1991.

[29] Sung, C.-H., "An Explicit Runge-Kutta Method for 3-D Incompressible Turbulent Flows", Report DTNSRDC/SHD-1244-01, July, 1987.

[30] Tahara, Y. and Stern F., "Validation of an Iterative Approach for Calculating Ship Boundary Layers and Wakes for Nonzero Froude Number", Journal of Computers and Fluids, Vol. 23, 1994.

[31] Thomas, G.R. "A Combined High-Order Spectral and Boundary Integral Equation Method for Modelling Wave Interactions With Submerged Bodies", PhD Thesis, Massachusetts Institute of Technology, 1997.

[32] Tsai, J.F., Sung C.H., Griffin, M.J., and Huang, T.T. "Effects of Grid Resolution on Axisymmetric Stern Flows Computed by an Incompressible Viscous Flow Solver", presented at the ASME Summer Fluids Engineering Conference, FED-Vol. 158, pp 99-108, June 20-24, 1993.

[33] Turkel, E., "Preconditioned Methods for Solving Incompressible and Low Speed Compressible Equations", Journal of Computational Physics, vol. 72, 277, 1987.

[34] Wilcox, D.C., *Turbulence Modeling for CFD*, DCW Industries, Inc., CA, 1993.

[35] Wilcox, D.C., "Reassessment of the Scale-Determining Equation for Advanced Turbulence Models," AIAA Journal, Vol. 26, No. 11, pp. 1299-1310, November, 1988.

[36] Yee, H.C., "A Class of High-Resolution Explicit and Implicit Shock-Capturing Methods", NASA Technical Memorandum 101088, February, 1989.